Field Ionization from Carbon NanoFibers

by

Bosun J. Adeoti

B.S., Electrical Engineering and Computer Science, Massachusetts Institute of Technology, 2007

Submitted to the Department of Electrical Engineering and Computer Science
in partial fulfillment of the requirements for the degree of

Master of Engineering in Electrical Engineering and Computer Science

at the

MASSACHUSETTS INSTITUTE OF TECHNOLOGY

February 2008

Author .....
Department of Electrical Engineering and Computer Science
September 14, 2007

Certified by .....
Akintunde Ibitayo (Tayo) Akinwande
Professor of Electrical Engineering
Thesis Supervisor

Accepted by ..
Arthur C. Smith
Chairman, Department Committee on Graduate Students

Field Ionization from Carbon NanoFibers

by

Bosun J. Adeoti

Submitted to the Department of Electrical Engineering and Computer Science
on September 14, 2007, in partial fulfillment of the
requirements for the degree of
Master of Engineering in Electrical Engineering and Computer Science

Abstract

The Micro Gas Analyzer project aims to develop power-efficient, high resolution, high sensitivity, portable and real-time gas sensors. We developed a field ionizer array based on gated CNTs. Arrays of CNTs are used because of their small tip radii and high aspect ratio which yields high electric fields at low voltages. One possible configuration for the device is to bias the CNTs at the highest potential, and the collector or anode at the lowest potential. In this configuration, the electrons in the outer shell of the molecules tunnel out due to the high local electric fields which serve to lower the unperturbed potential barrier seen by the electrons. The tunneling effect is a purely quantum-mechanical process whose probability of occurrence is strongly dependent on the applied electric fields.

We optimize the theoretical current obtainable from the Field Ionization Array (FIA) by varying structural parameters in our device. The most relevant parameters include the radius of curvature, height, base radius and base angle of the grown tip; height and thickness of the tip; and the gate aperture. Varying the gate (or oxide) height without updating the height of the CNT yields the derivable result that the electric field is maximized when the tip is at about the same height as the gate. We demonstrate field ionization of Argon from multi-walled CNTs and provide a numerical framework for analyzing the generated ion currents in cases where the surface electric fields are low.

Thesis Supervisor: Akintunde Ibitayo (Tayo) Akinwande
Title: Professor of Electrical Engineering

Acknowledgments

A lot of people have contributed in one way or the other to the development and completion of this thesis.

First and foremost, I would like to thank my advisor, Professor Tayo Akinwande, for his sustained mentorship and guidance throughout my undergraduate and graduate years. He was always ready with a kind word whenever I was struggling and just as ready with a fatherly disciplinary attitude whenever my progress was lacking. His high scientific standards taught me how to be a good scientist.

I cannot but appreciate the members of my research group. They constituted an invaluable source of technical know-how, advice and support. I would especially like to thank Drs. Luis Velasquez-Garcia and Liang-Yu Chen without whose breadth of fabrication knowledge and wisdom I would never have made much progress.

My sincere thanks go to all the staff of the MIT Microsystems Technology Laboratories who were responsible for maintaining the facilities and equipment I used in several of my fabrication processes. Robert Biccheri, Paul Tierney and Paudely Zamora deserve special mention for all those times they trained me to use the equipment and for helping me to use them.

I would also like to thank my family and friends for their constant encouragement and support. Muyiwa, Esosa, Jitin, Saba - I hope you guys realize how much I appreciate your unfailing confidence in me even when things looked bleak.

Finally, I would like to acknowledge the financial support that made this research possible. The DARPA/ US Army Natick Soldier System Center and the Total Corporation funded my research.

Contents

List of Figures

1 INTRODUCTION

1.1 Overview of Mass Spectrometers

Mass spectrometers are widely used in industrial plants for the detection of potentially dangerous gases. Such detection would indicate a possible leak in the plant. Mass spectrometers are also used inside plant machinery where measurements of gas concentrations are necessary to control the operation of the plant. The overall design of a mass spectrometer depends on its function. Designs for mass spectrometers that take accurate measurements of gas concentration can be significantly more complex than those for detecting the presence (or absence) of a particular gas.

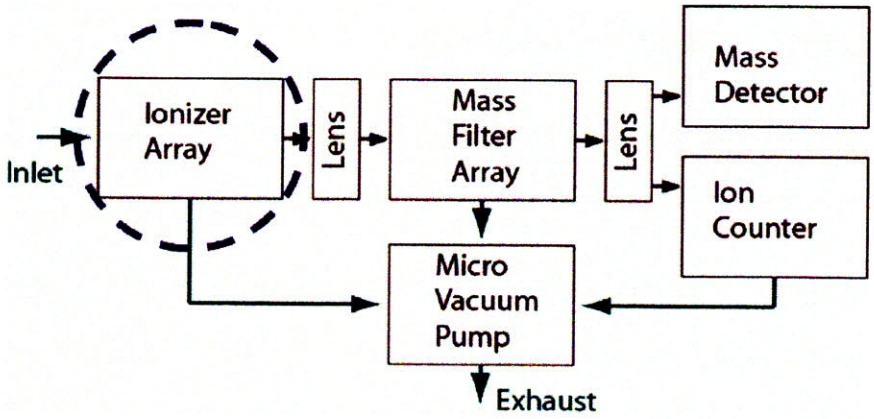

Fig. 1-1: Micro Gas Analyzer, Basic Schematics

The basic schematic of a mass spectrometer is shown in Figure 1-1. As shown, there is a single vacuum pump that draws gas through the entire device. Gas coming from the

environment first passes through an ionizer which strips electrons off the molecules. The beam of charged ions is then focused towards the mass filter array which transmits only ions of a certain mass range. Masses outside this range are collected by the rods of the mass filter. The transmitted ions can again be focused by lens, this time towards an ion counter which gives a measure of the concentration of the particular mass.

The over-arching purpose of the Micro Gas Analyzer (MGA) project is to reduce the size and power expenditure, and increase sensitivity of currently existing mass spectrometers.

1.2 Requirements for the MGA Ionizer

We assume an ion current detection limit of about $10^{-18}A$ [1]. Assuming we can achieve a reasonable ion resolution, then a resolution of 1 ppt (parts per trillion 10^{-12}) requires that we have an input ion current of about $1\mu A$. If we further assume that only 10% of the ions are transmitted through the mass filter, we see that we actually require about $10\mu A$ of input ion current at the ionizer output.

1.2.1 Eligible Ionization methods

There are several ionization methods currently used in mass spectrometers. Some of these methods are unsuitable for the MGA Ionizer for obvious reasons:

Induction Coupled Plasma in which a plasma is required. The typical output power for most ICP-based instruments is 1 to 2 kW [2]. Even more recent miniaturized ICP plasma sources require at least $0.5W$ plasma power [3] which violates the MGA Ionizer's power requirements

Fast Atom Bombardment which utilizes a fast moving beam of neutral atoms (typically Argon or Xenon at 8 kV) to bombard a metal target coated with a non-volatile liquid

called a matrix in which the analyte has been dissolved [4]

Field Desorption in which an emitter that has been coated with the analyte is slowly heated by passing a high current through it, while maintaining it at a high electric potential (typically thousands of volts). The analyte is desorbed and ionized by electron tunneling in a manner similar to field ionization [5, 6]

Electrospray Ionization in which an analyte-containing liquid is passed through a tiny, charged capillary [7]. The analyte is ionized as the solvent evaporates on exiting the capillary.

Two other ionization methods are commonly referenced in the literature. They are electron impact ionization [8, 9, 10, 11] and field ionization [6, 12]. For Electron Impact Ionization, electrons can be provided by thermionic emission [13], plasma electron sources [14] and field emission [6, 12, 15, 16, 17].

Electron Impact Ionization using thermionic cathodes is characterized by very low ionization efficiencies (low ionization cross-section ratio of 10^{-16}) [18]. Thermionic cathodes also use excessive power $(1 - 3W)$ [19]. They generate heat, burning the cathode elements slowly and they have short life spans. Plasma electron sources for electron impact ionization can also be rejected on the same bases that we reject Induction Couple Plasma.

Therefore, the ionization methods we can use to attain the specificity and sensitivity goals of the MGA reduce to

1. electron impact ionization by way of field emission electrons

2. field ionization

1.2.2 Field Ionization Arrays

The work presented in this thesis explores the application of the field ionization method. Field Ionization is preferably to Electron Impact Ionization because the latter is known to be a rather violent process which produces fragmented ions [11, 19]. This is why we say Electron Impact Ionization is a "hard" form of ionization. On the other hand, field ionization is a "soft" ionization method. It produces regular ions of mainly charge +1 [12]. With a Field Ionization Array operating at an input voltage of $200V$, we expend only $2mW$ of power, which meets the power requirements.

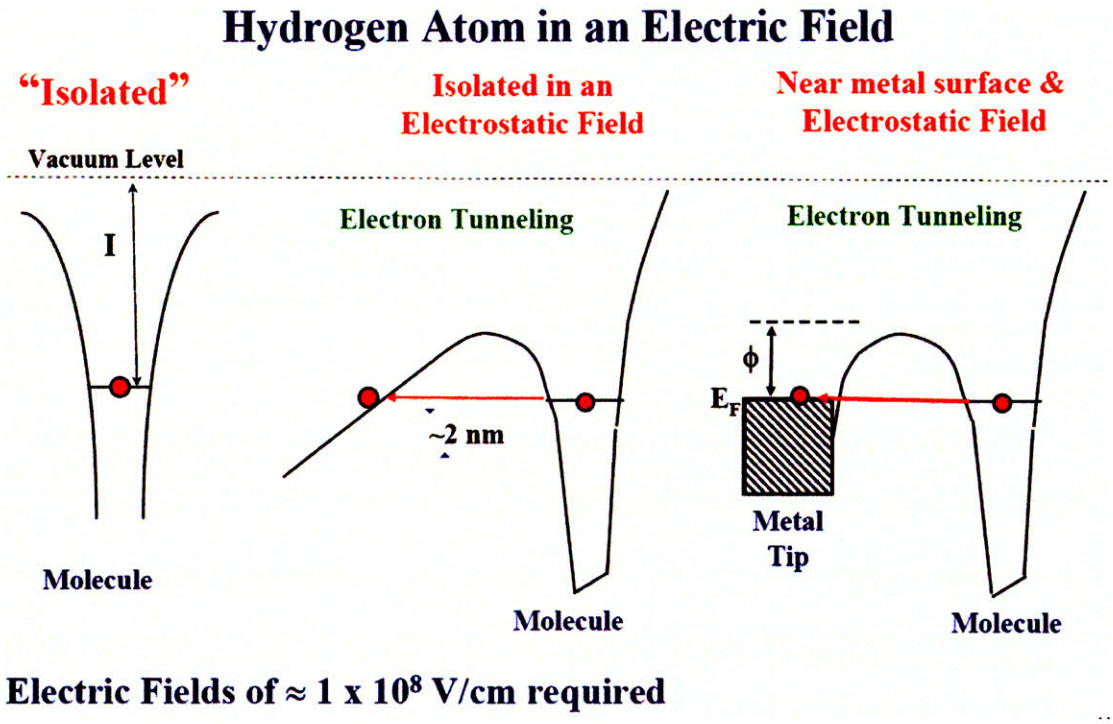

Fig. 1-2: Physics of Field Ionization

Field Ionization of gas molecules works by quantum tunneling of electrons through narrow potential barriers created by an external field [6]. Even when the tunneling is facilitated by the presence of metal tips in the vicinity of the field (figure 1-2), very large electric fields are required. For instance, field ionization of a hydrogen atom requires about $10^8 V/cm$.

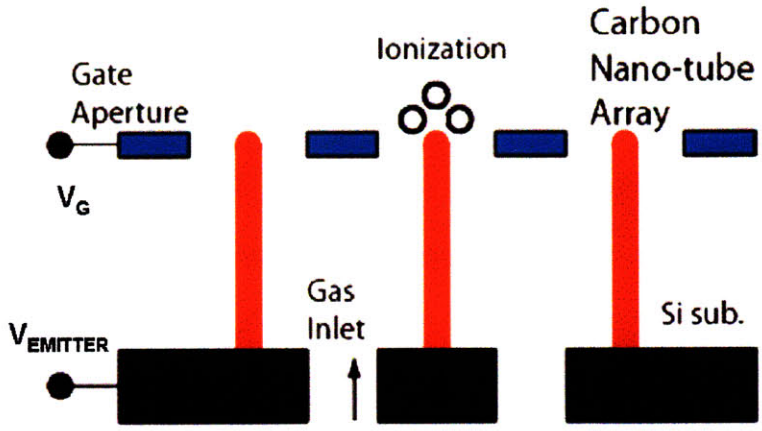

Fig. 1-3: Working template for Field Ionization Array

To obtain such high fields at low voltage, **and** satisfy the current requirements of the MGA Ionizer, we proposed to use arrays of gated carbon nanotubes (CNT) as the main components of our Field Ionization arrays. In addition to the possibility of obtaining proximal gates at lower potential, CNTs [1]provide the advantages of small radii, high aspect ratio, high chemical stability and high mechanical strength [24]. These properties are especially suited to the particular implementation of Field Ionization. They ensure that we can have high electric fields at low voltage and obtain high ionization efficiency.

Arrays of CNTs are used to increase the output currents. Because the arrays contain isolated, well-spaced elements, there is no shadowing effect whereby the surface fields are reduced because of the closeness of the emitters. Field ionization of Helium has already been demonstrated [20] but the experimenters used highly dense forests of carbon nanotubes.

In our field ionization configuration, the tips are biased at the highest potential. The positively charged ions move away from the CNT tips towards the lower potential electrode, the lens. No damage ever occurs to the CNT tips due to ion collision; hence, the FIA is

[1]Strictly speaking, the designation "CNT" is not accurate here. The term "Carbon nanotubes" is widely accepted as describing cylindrical structures with well-defined and uniform radii. The vertical conical-shaped CNT-like structures that we use are best called carbon nanofibers. Throughout this work, we will use the terms CN, CNT and CNF interchangeably to refer to these vertical carbon nano fibers

robust. The voltage requirements of the Field Ionization array are also significantly lower than those of the thermionic cathodes ($100V$ as opposed to $10,000V$ [18]).

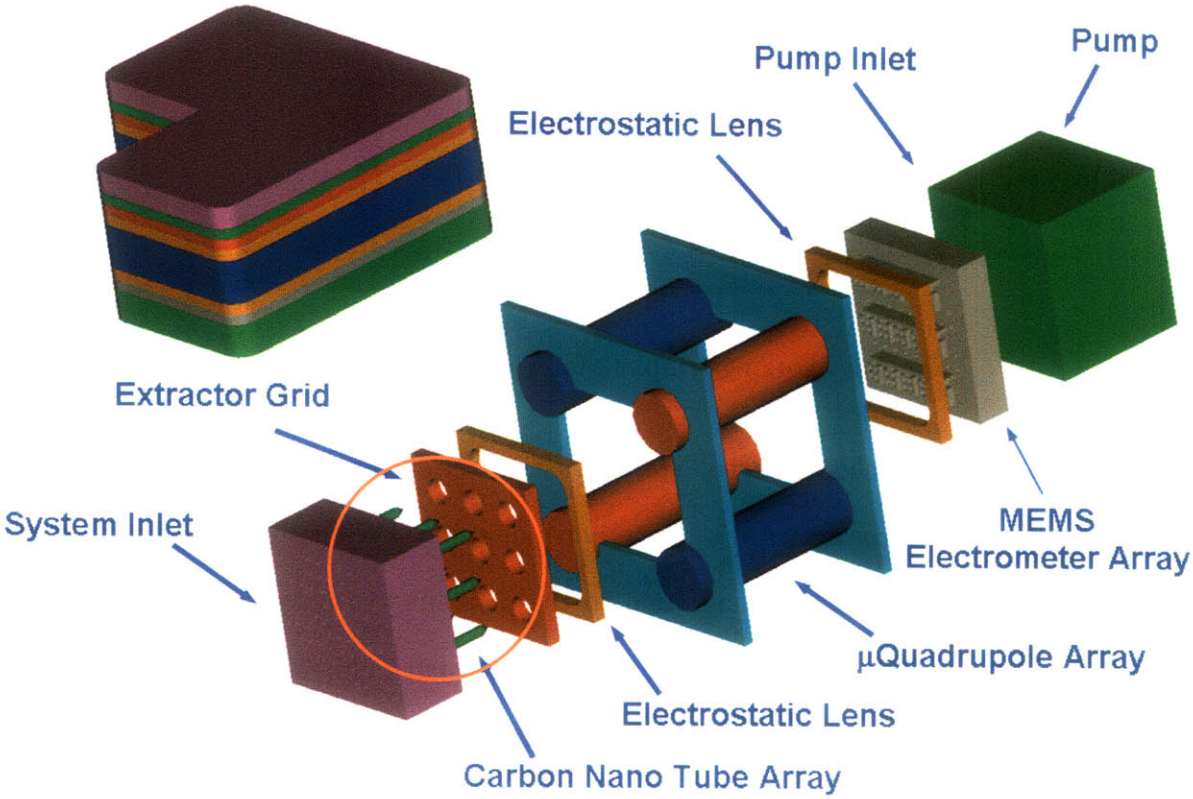

Fig. 1-4: Full Schematic of Micro Gas Analyzer

1.3 Thesis Organization

The outline of this thesis is as follows:

In chapter 2, we present the theories of Field Emission and Field Ionization as these will be important for our analysis and appreciation of any data we collect. We also examine some field ionization data from the literature, using our field ionization equations in the low field regime.

In chapter 3, we present some analytical models for predicting field amplification at sharp tips. We also present the results of numerical simulations of the electrostatic fields at sharp

tips and use these results to design the device that we develop in chapter 5.

Chapter 4 contains a description of the growth process for the carbon nanotubes and presents a characterization of the CNT growth tool.

In chapter 5, we describe the fabrication process for our device and present two different methodologies for gating the CNTs. The complete fabrication process is also tabulated in appendix A.

Chapter 6 deals with the characterization of our device. Here, we demonstrate field ionization of Argon with our device and compare the results to a field ionization experiment reported in the literature.

Finally, we summarized the thesis in chapter 7 and make some recommendations for future work.

2 Background & Theory

2.1 Electron Impact Ionization

Electron impact ionization is the mechanism by which electrons are used to ionize and fragment molecules. The ions produced can then be used for a number of subsequent processes, notably mass spectrometry [19, 18]. This process is a relatively harsh form of ionization producing a wide range of molecular fragments, but it is still the most widely used form of ionization. There are many methods of producing the electrons used in an impact ionization process, all of which involve getting electrons to overcome the work function (barrier height) of the material from which the electrons are to be extracted.

Consider a metal-vacuum surface in the absence of any external electric fields. A schematic of the electron energy levels in a metal is shown in Figure 2-1. The electrons in the bulk material are restricted to the conduction band; the most energetic electrons have a maximum energy level at $0K$ (the Fermi energy). Classically, the energy gap between this Fermi sea of electrons and vacuum is termed the work function (ϕ) of the metal, and this corresponds to the minimum energy needed to remove an electron from the bulk.

For electron impact ionization, the electrons are commonly extracted by thermionic emission or field emission, or from plasma electron sources [14].

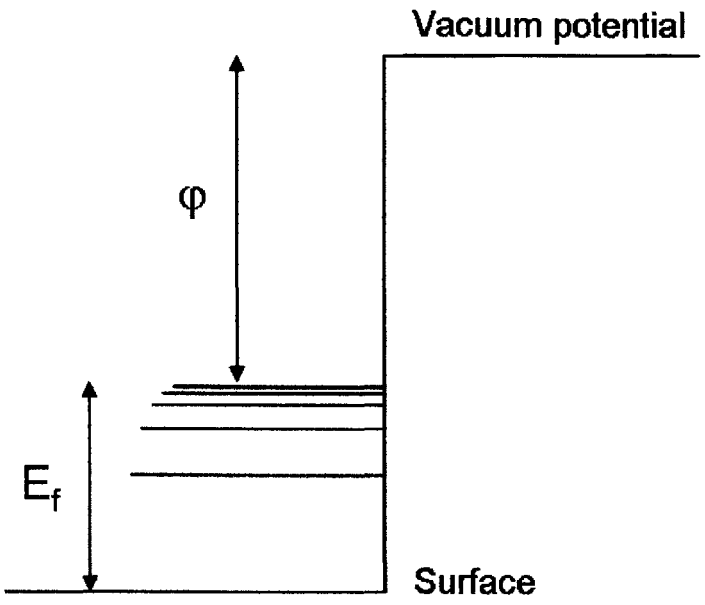

Fig. 2-1: Schematic of electron energy levels in metal. E_f is the Fermi level of the electron inside the metal while ϕ is the work function

2.1.1 Thermionic Emission

In a conducting material, the electrons are governed by Fermi-Dirac statistics. The baseline electron energy is the Fermi Energy, and at low temperatures the electrons all exist at or below this level. As temperature is increased, so the Fermi-Dirac distribution function

$$n(E) = \frac{1}{\exp^{\frac{E-E_f}{k_B T}} + 1}$$

for the electrons develops a high energy 'tail'. $n(E)$ is the probability of occupation of an electronic state with energy E, $k_B = 1.38 \times 10^{-23} J/K$ is the Boltzmann constant and T is the absolute temperature. At non-zero temperatures, some of the electrons have sufficient energy to pass over the surface potential barrier between the material and the vacuum. This process of increasing the temperature of a bulk material to increase the number of electrons which can leave the material is called thermionic emission [13].

2.1.2 Field Emission

Field emission is a quantum-mechanical process that occurs at the surface of a conducting material. In thermionic emission, the electrons are supplied thermal energy such that a finite number of electrons have sufficient energy to escape from the material. In field emission, an external field is applied to deform the barrier so that electrons can tunnel through.

The unperturbed (no external fields) potential barrier at the surface of the metal is flat, constant value $-\phi$. When a positive voltage is applied to the metal surface, the shape of the potential barrier faced by the electrons is narrowed so that the electrons have finite probability of tunneling through the barrier. This purely quantum-mechanical effect can be qualitatively explained with the aid of the Heisenberg Uncertainty Principle [6].

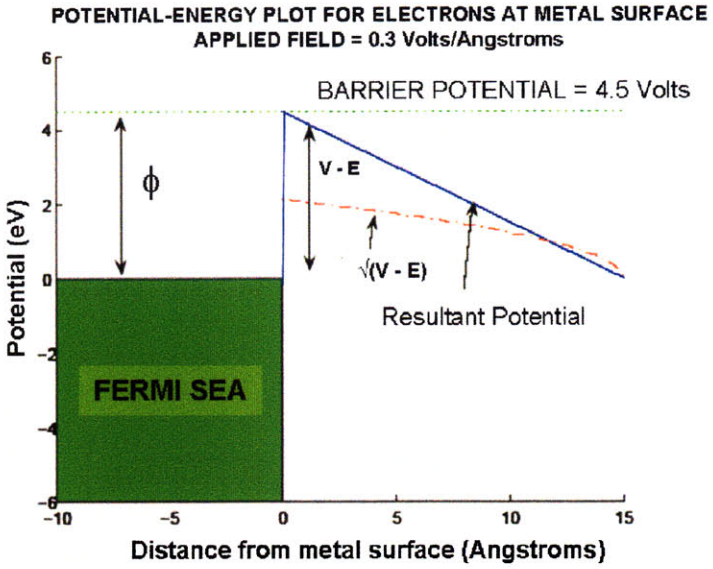

Fig. 2-2: Potential Energy Plot for Electrons at Metal Surface with Applied Positive Voltage

Consider electrons near the Fermi level. These have an uncertainty in momentum $\Delta p \sim \sqrt{2m\phi}$ due to the flat barrier, height ϕ. The corresponding uncertainty in position is $\Delta x \sim \frac{\hbar}{2\sqrt{2m_e\phi}}$. If the barrier width facing the electron at Fermi energy is of the order of Δx, then there is finite probability that the electron can be found on the other side of the barrier.

This means the electron may be "found" to have tunneled out of the metal!

Strong electric fields of the order of 10^7 *volts/cm* are required to achieve field emission in a metal. This follows from the fact that the work function ϕ of metals (also the barrier potential in Figure 2-2) is usually in the range $2 - 6$ eV [6]. The applied electric field must deform the barrier so that the barrier width is of the order of 1 *nm*. Once electrons have tunneled out of the metal, they can be used to ionize test gas molecules by impact ionization. Therefore, when scientists refer to the "field emitted electron impact ionization," they are actually referring to a two-step phenomenon in which field emission serves as a source for the electrons which are then used to bombard and strip electrons off the gas molecules.

The field emission of electrons from a solid-vacuum can be broken down into three continuous process: 1) electron flux to the surface, limited by the electron supply, 2) tunneling through the surface barrier potential determined by the tunneling transmission coefficient, and 3) movement of the electrons in the vacuum

Quantitative analysis of the tunneling probability of electrons of varying energies is made possible by the application of the Wentzel-Kramers-Brillouin (WKB) approximation equation for penetration coefficients:

$$D = exp\left\{-2\sqrt{\frac{2m_e}{\hbar^2}}\int\sqrt{V(x)-W}dx\right\}$$

where D = tunneling probability, m_e = mass of electron, W = total energy of electron and $V(x)$ is the potential energy barrier seen by the electron. The integral is done over the region where $V(x) > W$, i.e. where there is a classical barrier. Note that this region corresponds to a classically forbidden region since the electron has negative kinetic energy $W - V(x) < 0$. Using the WKB equation to derive a tunneling probability $D(F, E)$ where F is the applied field and E is the tunneling electron's energy, Fowler and Nordheim were able to calculate

the emitted current by integrating $D(F, E)$ weighted by the appropriate differential arrival rate over the electron energy interval $0 \leq E \leq \mu$. The Fowler-Nordheim (FN) equation, recast here as a function of applied voltage, is given by:

$$I = a_{FN} V^2 e^{\frac{-b_{FN}}{V}} \tag{2.1}$$

where

$$\begin{aligned} a_{FN} &= \frac{\alpha A \beta^2}{1.1\varphi} e^{\frac{B(1.44\times10^{-7}}{\varphi^{0.5}}} \\ b_{FN} &= \frac{0.95 B \varphi^{3/2}}{\beta} \\ A &= 1.54 \times 10^{-6} \\ B &= 6.87 \times 10^{7} \end{aligned}$$

α is the effective emitter area, φ is the workfunction (we assume the value $\varphi = 4.8eV$ as for graphite), and β is the field factor.

2.2 Field Ionization

Field Ionization is sometimes thought of as field emission in reverse. There are many reasons to justify this. First, a large negative electric field is applied to the tip, as opposed to the positive field in field emission. Secondly, electrons tunnel from the gas molecule into the tip. Recall that in field emission, electrons tunnel out of the tip (metal surface).

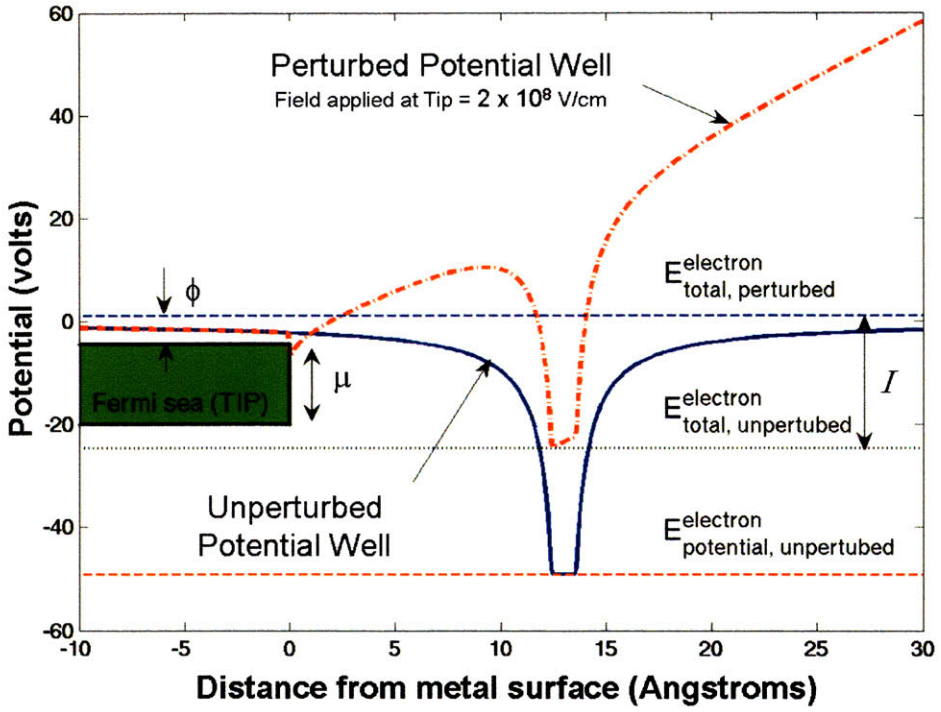

Fig. 2-3: Illustration of Potential Wells in the Field Ionization scenario

2.2.1 Mechanism of Field Ionization

The electrons in the gas molecule are bound by the potential barrier due to the positive charges (protons) at the core of the molecule. Figure 2-3 shows a simulated potential barrier after image effects at the tip are taken into account. The unperturbed potential well is the Coulomb potential seen by the electron in the absence of external fields. In this well, the electrons lie at $-I$ below the vacuum level (zero potential in the plot) i.e. the total energy of the most energetic electrons $E_{\text{total}}^{\text{electron}}$ is $-I$. The perturbed potential well is the deformed potential seen by the electron. Here, we have shown the perturbation that raises $E_{\text{total}}^{\text{electron}}$ to vacuum level. Before the perturbation, the electron faced an infinitely wide potential barrier. The field serves to deform the Coulomb barrier so that the electron sees a barrier of finite height and width. If the barrier is small enough, the electron can tunnel through.

$E_{\text{total, perturbed}}^{\text{electron}}$ decreases as the atom or molecule gets closer to the tip. When the molecule

is so close to the tip that $E^{\text{electron}}_{\text{total, perturbed}}$ is less than $-\phi$ (the top of the Fermi sea of electrons in the tip), no tunneling can occur. The reason for this limit is that there are no empty states below the Fermi level μ into which an electron may tunnel. That is, (in a metallic tip), there are no states an electron may occupy after tunneling if $E^{\text{electron}}_{\text{total, perturbed}} < -\phi$. Therefore, the applied field must raise the tunneling electron to above the Fermi level for field ionization to occur. This effect gives rise to a critical distance x_c [6, 16] defined as the minimum distance from a field amplifying material at which field ionization may occur. Assuming the field is uniform in regions very close to a metallic tip,

$$x_c \cong \frac{I - \phi}{F_0} \tag{2.2}$$

where I is the ionization potential of the ionized gas and F_0 is the surface electric field.

The tunneling probability D can be estimated using the WKB approximation and an initial assumption that image effects are negligible. Gomer [6] gives this first-order approximation:

$$D \cong \exp\left\{ -6.8 \times 10^7 * \frac{I^{\frac{3}{2}}}{F} * \sqrt{1 - 7.6 Z_{eff}^{\frac{1}{2}} F^{\frac{1}{2}} \times \frac{10^{-4}}{I}} \right\} \tag{2.3}$$

where Z_{eff} is the effective nuclear charge of the molecule being ionized and F is the local electric field at the molecule's position.

In the approximating equation 2.3 for the field ionization tunneling probability D, the "Image Force Lowering" factor

$$\varepsilon(F) = \sqrt{1 - 7.6 Z_{eff}^{\frac{1}{2}} F^{\frac{1}{2}} \times \frac{10^{-4}}{I}} \tag{2.4}$$

increases the overall tunneling probability in an attempt to correct for image effects. Unfortunately, $\varepsilon(F)$ makes equation 2.3 invalid at very high fields since it becomes imaginary

as $F \rightarrow \infty$. However, equation 2.3 remains very useful since it is reasonable to assume that $D \rightarrow 1$ as $F \rightarrow \infty$.

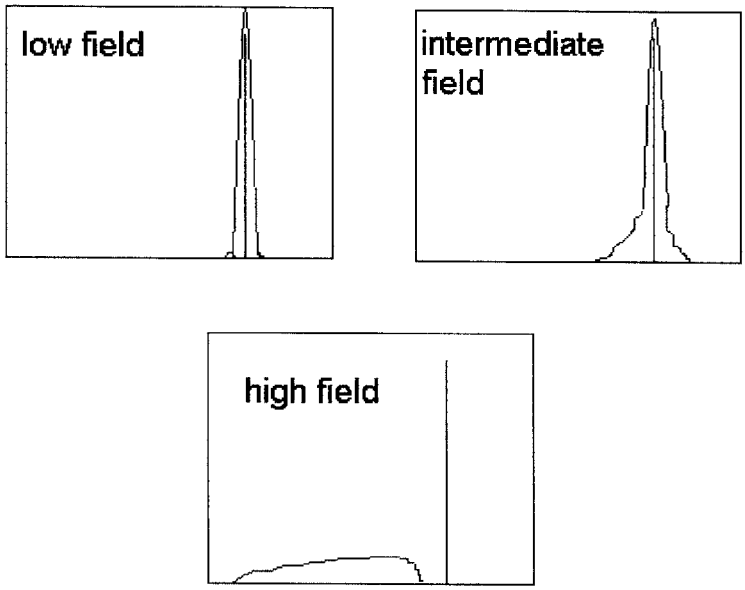

Fig. 2-4: Peak shapes of ion intensity profile in different regimes

2.2.2 High Field Regime

At sufficiently high fields, the ionization probability is so high that no molecules enter the vicinity of the tip and remain neutral. All supply molecules are ionized before they reach the immediate vicinity of the tip and hence none actually gets close to the tip. The ion current observed will thus depend solely on the supply function $n(r_t, P, T, F_0)$ where r_t is the tip radius, P is the gas pressure, T is the absolute temperature and F_0 is the surface electric field at the tip. The supply function will exceed the gas-kinetic levels defined by $n_0(r_t, P, T)$ since molecules on trajectories close to the tip will be attracted to it by polarization forces [16].

$$n_0 = 2\pi r_t^2 \sigma P \sqrt{2\pi m k_B T} \tag{2.5}$$

where m is the mass of gas particle.

The ion intensity profile will be smeared out over many electron-volts [6] since the Coulomb potential faced by the tunneling electrons will be so strongly deformed that electrons from many energy levels will be able to tunnel out, not just the more energetic electrons as is the case with other field regimes of field ionization.

2.2.3 Low Field Regime

The low field regime is characterized by a small (total) rate of ionization compared to the rate of arrival (supply). Any molecule reaching the vicinity of the tip ionizes with some probability D; otherwise it simply bounces back. The ion current in this regime is directly proportional by the equilibrium number of particles near the tip and inversely proportional to the mean lifetime of the molecule with respect to the ionization process.

Ionization in the low field regime will only occur in regions R_t close to the tip. At equilibrium, particles are moving in and out of this region, and, by the equilibrium condition, the flux of particles into this region must equal the flux of particles out of the region.

A representation of the region close to the tip is shown in Figure 2-5 where

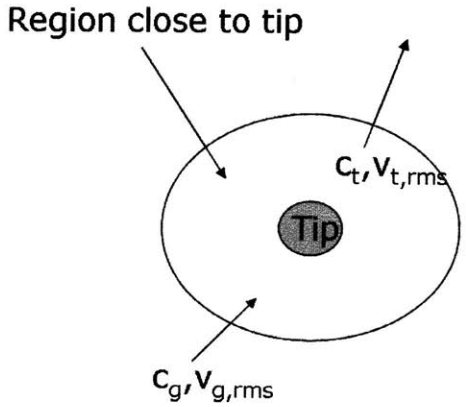

Fig. 2-5: Schematic of the immediate vicinity of the tip

$\nu_{g,rms}$ = gas velocity far from the tip

$\nu_{t,rms}$ = equilibrium gas velocity near the tip

c_g = (neutral) gas concentrations far from the tip

c_t = the equilibrium (neutral) gas concentration near the tip

Since the equilibrium condition stipulates zero total flux into R_t, we have

$$c_t \nu_{t,rms} = c_g \nu_{g,rms} \tag{2.6}$$

The root-mean-square velocity of a gas molecule of mass m at temperature T is $\nu_{rms} = \sqrt{\frac{3kT}{m}} \propto T^{1/2}$. Therefore, equation 2.6 reduces to $c_t T_t^{\frac{1}{2}} = c_g T_g^{\frac{1}{2}}$ and we get

$$c_t = c_g \sqrt{\frac{T_g}{T_t}}$$

If we now take into account the polarization energy of the gas molecule, c_t becomes:

$$c_t = c_g \sqrt{\frac{T_g}{T_t}} \exp\left(\frac{-V(F)}{kT_g}\right) \tag{2.7}$$

where we have added a Boltzmann factor and

$-V(F)$ = Potential energy of a particle in the field F

$= P_D F + \frac{1}{2}\alpha_p F^2$

α_p = polarizability of the particle

P_D = sum of dipole moments of the particle

T_g = gas temperature

Letting F_0 be the field at the tip surface, we have $F \simeq F_0 \left(\frac{r_t}{r}\right)^2$ and we take $V(F)$ as a function of r only. Now, assuming total ionization does not decrease c_t significantly, current from volume element $dV = 2\pi r^2 dr$ is $di = qc_t\tau_{-1}dV$ where q is the electronic charge and τ is the mean lifetime of a neutral molecule in R_t. τ can be approximated by

$$\tau = \frac{1}{\nu_e D} \tag{2.8}$$

where ν_e is the arrival rate of electrons at the potential barrier [6] and D is the tunneling probability approximated by equation 2.3.

The total current is therefore derived by integrating these current elements from the minimum radius at which field ionization can occur $(r_t + x_c)$ to ∞:

$$i = 2\pi c_g \int_{r_t+x_c}^{\infty} r^2 \tau^{-1} \sqrt{\frac{T_g}{T_t}} \exp\left(\frac{-V(r)}{kT_g}\right) \tag{2.9}$$

$$\cong 2\pi r_t^2 c_g x_c \tau^{-1} \sqrt{\frac{T_g}{T_t}} \exp\left(\frac{-V(F_0)}{kT_g}\right) \tag{2.10}$$

where r_t is the tip radius and x_c is the critical distance as previously seen in section 2.2.1 and defined in equation 2.2.

Summarizing these results:

$$i \propto \underbrace{C_1}_{\text{pre-constants}} * \underbrace{\frac{C_2}{F_0}}_{x_c} * \underbrace{\exp\left(-\frac{C_3\varepsilon(F_0)}{F_0}\right)}_{\tau^{-1}=\nu_e D} * \underbrace{\exp(C_4 F_0^2)}_{\text{potential energy term}} \tag{2.11}$$

in which we have expanded x_c using equation 2.2 and expanded τ^{-1} using equation 2.8 and assuming only the tunneling probability $(D(F_0))$ infinitesimally close to the tip matters.

In writing equation 2.11, we have also collected the constant terms:

$$C_1 = 2\pi r_t^2 \sqrt{\frac{T_g}{T_t}} c_g \nu_e \qquad C_4 = \frac{\alpha_p}{2k_B T_g}$$

$$C_2 = I - \mu \qquad C_3 = 6.8 \times 10^7 I^{\frac{3}{2}}$$

$\varepsilon(F) = \sqrt{1 - \frac{7.6\sqrt{Z_{eff}F} \times 10^{-4}}{I}}$ = the "Image Force Lowering" factor defined in equation 2.4.

In expanding the potential energy term $-V(F_0)$, we ignore any dipole moments P_D that the gas particle being ionized might have. This is certainly a valid assumption for the gases Argon and Helium used in this work. Argon and Helium are inert gases which have no dipole moments.

2.2.4 Intermediate Field Regime

This regime exists at fields intermediate between the above two extremes of low and high fields. It is more complicated to analyze in closed form because incoming molecules have velocities in excess of thermal values due to polarization and dipole forces and because of the possibility of rebounding molecules. Gomer's discussion of this regime is very instructive but not in any way definitive [6].

2.3 Examination of FI Data from Literature

In their 2003 paper [20], Riley et al presented data for field ionization of Helium molecules by carbon nanotube tips. In this section, we analyze their data assuming their device operated in the low field regime. This assumption is justified by the fact that the deducible field factors from their experiments was of the order of $10^4/cm$ while they applied voltages in the range $5.5 - 9kV$. The resulting surface electric fields were thus in the low field regime.

After extracting their data from the paper, we derive the plot in Figure 2-6 which leads us to conclude that the authors achieved field ionization in their experiment. The data is given as ion count rate(CR) vs. voltage(V) applied to the CNTs. Since current $i \propto CR$ and field $F \propto V$, we fit with CR and V as given. We first attempt a fit using only the strongest term in the low field regime equations. Then we add the critical distance term and finally we include the potential energy term of equation 2.11 in our fittings.

"Image Force Lowering" Factor $\varepsilon(F)$ In the following fittings, we ignore the "Image Force Lowering" factor $\varepsilon(F)$. Our justification for doing this is illustrated in Figure 2-7. The voltage range of the data we are analyzing spans 14 orders of magnitude of tunneling probability. $\varepsilon(F)$ serves as a power factor and is fairly constant $(0.68 \rightarrow 0.76)$ in the range of

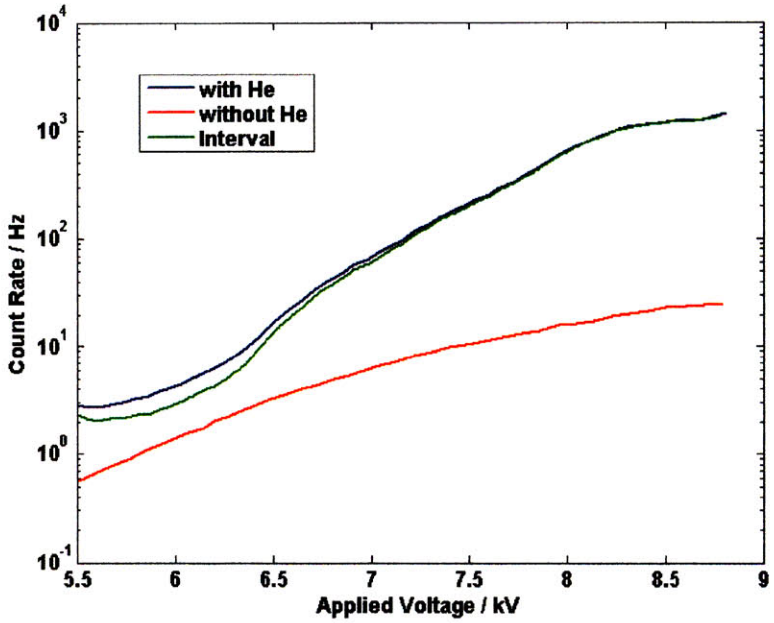

Fig. 2-6: Field Ionization of Helium from carbon nanotubes. The uppermost trace indicates the time-averaged detection current as a function of voltage applied. The lower trace indicates the "background" ion current, measured in the absence of admitted helium

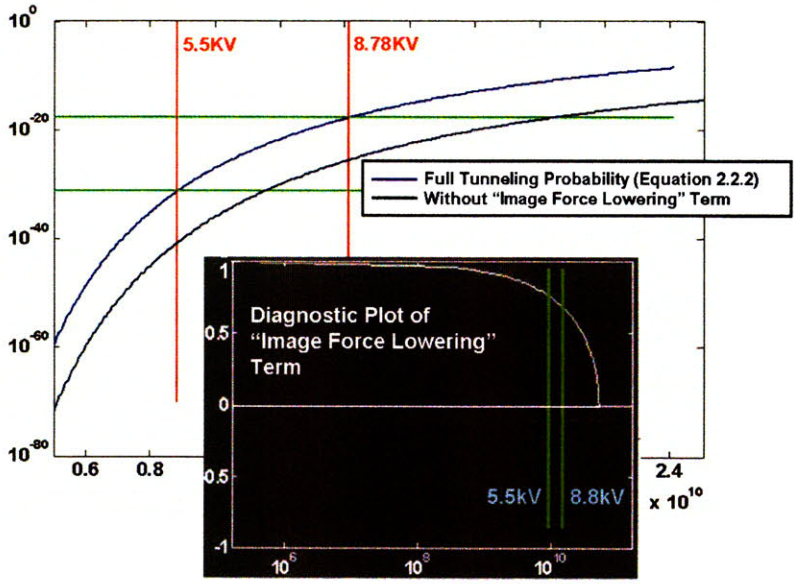

Fig. 2-7: Diagnostic Plot of tunneling probability estimate, showing range of actual data and "Image Force Lowering" factor

our data. Its effect is to reduce the ionization probability by a uniform 8 orders of magnitude. Since we are only interested in confirming or refuting the relationship evident in the low field regime equations, we can and will ignore $\varepsilon(F)$ for now.

Data Fits

Fitting to $i \propto exp\left(-\frac{C_3\varepsilon(F_0)}{F_0}\right)$ The exponential term $exp\left(-\frac{C_3\varepsilon(F_0)}{F_0}\right)$ is arguably the strongest term in equation 2.11. We first attempted a fit to just that exponential term. Manipulating $i \propto exp\left(-\frac{C_3\varepsilon(F_0)}{F_0}\right)$, and assuming $i = k_1 c_{RATE}$ and $F_0 = \beta V$, we deduce that $\ln(c_{RATE}) \propto \frac{1}{V}$ with a proportionality constant $\frac{C_3\varepsilon(F_0)}{\beta}$. Figure 2-8 shows that the resulting fit does have a strong linearization with slope 1.163×10^5.

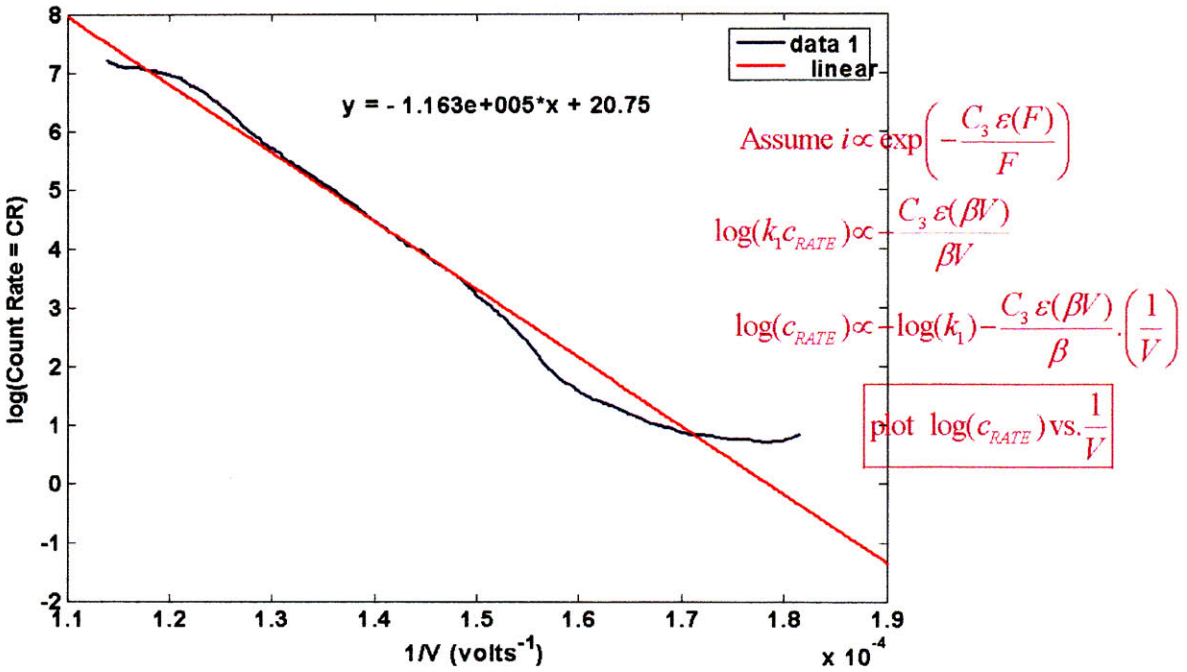

Fig. 2-8: Fit to Exponential (Tunneling Probability) term

Fitting to $i \propto \frac{C_2}{F} exp\left(-\frac{C_3 \varepsilon(F_0)}{F_0}\right)$ We add the next strongest term, the critical distance term $x_c = \frac{C_2}{F_0}$, to our fit function. Manipulating $i \propto \frac{C_2}{F_0} exp\left(-\frac{C_3 \varepsilon(F_0)}{F_0}\right)$, assuming $i = k_1 c_{RATE}$ and $F_0 = \beta V$, yields $\ln(c_{RATE} * V) \propto \frac{1}{V}$ with the same proportionality constant as above, $\frac{C_3 \varepsilon(F_0)}{\beta}$. On refitting, we find that this plot (Figure 2-9) also shows a strong linear component, this time with slope 1.233×10^5. This slope is only 6% bigger than the previous slope so we conclude that the critical distance term is not very relevant in the voltage range of the data.

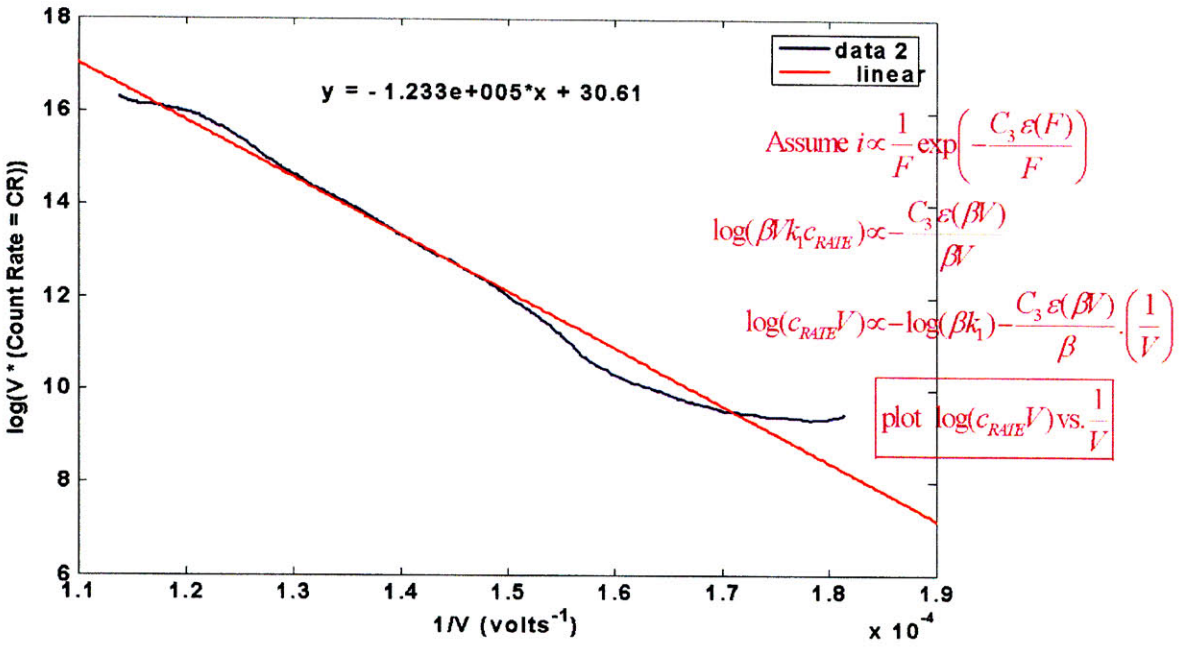

Fig. 2-9: Including Critical Distance component in fit

Fitting data to $i \propto \frac{C_2}{F_0} exp\left(-\frac{C_3\varepsilon(F_0)}{F_0} + C_4F_0^2\right)$ We include all the terms in equation 2.11. We multiply both sides of the relation 2.11 by F_0 and take logs to get:

$$\ln(iF_0) \propto \ln(C_2) - \frac{C_3\varepsilon\left(F_0\right)}{F_0} + C_4F_0^2$$

Multiplying through by F_0 again, and assuming $i = k_1 c_{RATE}$ and $F_0 = \beta V$ as before, we arrive at $\beta V \ln(k_1 c_{RATE}\beta V) \propto \beta V \ln(C_2) - C_3\varepsilon\left(\beta V\right) + C_4\beta^3V^3$ which simplifies to:

$$V \ln(c_{RATE}V) \propto V \ln(\frac{C_2}{k_1\beta}) - \frac{C_3}{\beta}\varepsilon\left(\beta V\right) + C_4\beta^2V^3$$

Thus, we are able to predict fits to degree 1 (linear) or degree 3 polynomials on a plot of $V \ln(c_{RATE}V)$ against V shown in Figure 2-10. We find that the degree 3 polynomial is superfluous since its linear component dominates terms of all other degrees.

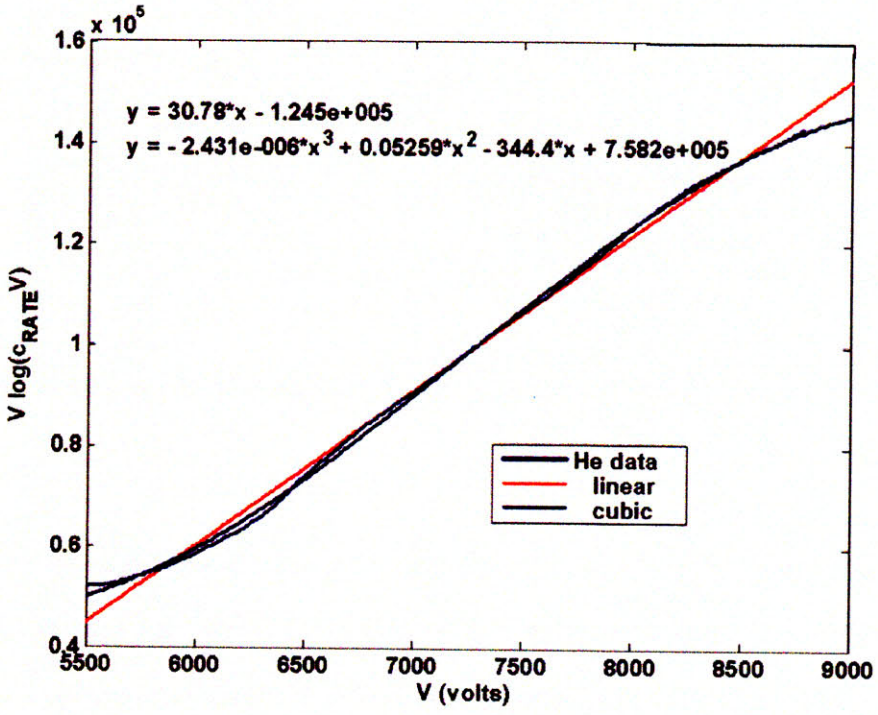

Fig. 2-10: Including Boltzmann factor

Conclusions The fit to polynomial degree 3 shows a very strong linear component, possibly because the Boltzmann factor contribution can be ignored since C_4 is so small. We will ignore the 3rd polynomial degree and adopt the linear fit, including the $\frac{1}{F}$ multiplier. As an accuracy check, we attempt to extract the ionization potential of Helium from the data.

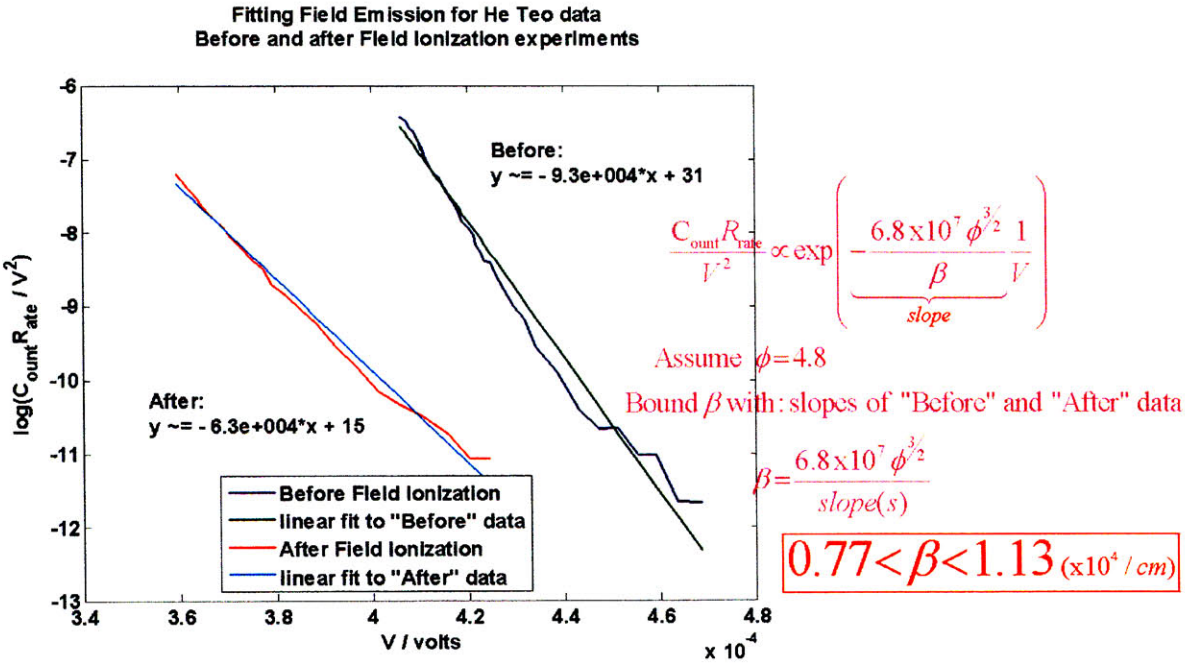

Fig. 2-11: Extracting the field factor using a Fowler-Nordheim fit of the Field Emission data

Accuracy Check First we extract the operating field factor using the "Before" and "After" Field Emission data as in Figure 2-11. After extracting the Fowler-Nordheim coefficients b_{FN} from the Fowler-Nordheim plots of the Field Emission data, we conclude that

$$0.77 \times 10^4 < \beta < 1.13 \times 10^4 \ /cm$$

using $b_{FN} = \frac{0.95B\varphi^{3/2}}{\beta}$ and a value of 4.8 for the work function ϕ of graphite. From the linear fits to the field ionization data, we see that

$$\frac{C_3\varepsilon(F)}{\beta} \approx 1.214 \times 10^5$$

Recalling that $C_3 = 6.8 \times 10^7 I^{\frac{3}{2}}$, and $\varepsilon(F)$ is fairly constant($0.68 < \varepsilon(F) < 0.76$), we can bound I:

$$6.90 < I < 9.63$$

As it turns out, this estimate is not very accurate ($I_{Helium} = 24.587$). However, it is well within the order of magnitude.

3 Device Design

The Fowler-Nordheim formula which describes the fundamental process and equation that governs the field emission phenomenon was presented in chapter 2. In addition, we saw analytical models for the process of field ionization in its different electric field regimes. In order to achieve field emission or field ionization from surface, we require huge electric fields, typically $\sim 2 - 6 \times 10^7\ V/cm$ for field emission and even higher ($\sim 2 \times 10^8\ V/cm$) for field ionization. Large voltages would be required to achieve such high fields on a planar surface, even at sub-micron spacing.

As an example, a parallel plate at a spacing of $50nm$ would require $250V$ to achieve a surface electric field of $\sim 5 \times 10^7\ V/cm$. Therefore, to obtain high electric fields at low voltages, we need to use high aspect physical structures with small tip radii. This is the essential inspiration for the idea to use carbon nano fibers as field emission / field ionization elements. The sharp tips enhance the surface electric field. Other sharp-tipped structures such as doped silicon tips exist and have been explored for the similar purposes [31, 32] but, as previously mentioned, field emission or field ionization elements have the advantage that they can be fabricated in bulk and hence yield higher currents [30].

The first and most important step in predicting the current densities expected from a given device is to solve for the electrostatic field in all traversable regions of a typical device geometry. Given a module to solve for one particular geometry, we can generate multiple geometries and estimate the tunneling probabilities (and hence ionization probabilities) for

each of the geometries. Then, we look at our actual device and compute expected ionization currents based on the observable distribution of actual geometries.

Unfortunately, most practical geometries are either not analytically solvable or require disproportionate amounts of effort to solve. To provide a more accurate picture of the operation of our device, we need a numerical model. Here is where finite element methods come into the picture.

We first describe some analytical models for predicting the field amplification of a tapering carbon nano fiber. All analytical models that have been put forward have been suggested with field emission in mind. Since the physics of the phenomenon of field amplification at sharp tips will not change when we invert the electric potential, these models describe field amplification whether or not we have field emission or field ionization in mind.

3.1 Analytical models of Electric Field Enhancement by Cone-shaped Field Emitters

3.1.1 "Ball in a Sphere" model

The "ball in a sphere" model represents the cone-shaped (tapering) field emitter as a ball enclosed by a larger sphere which represents the gate structure. The radius of the inner ball r corresponds to the radius of curvature of the tip, which can be estimated by fitting a circle to the tip circumference. The radius of the outer ball d corresponds to the effective radius of the gate structure. This model is effective to the extent that the field at the tip is mathematically related to the curvature of the tip.

In the Field Emission setup, the emitter is grounded, i.e., $V(r) = 0$ and a voltage $V(d) = V_g$ is applied to the gate. Given these boundary conditions, a solution to Laplace's

equation in spherical coordinates [25] yields the electric field at the ball's surface to be

$$\frac{F_{tip-surface}}{V_g} = -\beta = -\left(\frac{1}{r} + \frac{1}{d-r}\right)$$

In the case where $d >> r$ (as is usually the case), the "ball in a sphere" model predicts that the surface electric field is independent of the gate aperture ($2d$) and inversely proportional to the radius of curvature of the tip. Our previous required field of 5×10^7 V/cm can now be obtained at a low 10 V with a tip of radius of curvature $2nm$.

3.1.2 Coaxial Cylinders

The coaxial cylinder model is particularly effective for predicting the field enhancement effects we would see in a ridge type field emitter. In this model, the interior cylinder is analogous to the cone ridge and the outer cylinder is analogous to the gate structure.

Solving the model in cylindrical coordinates yields

$$\frac{F_{tip-surface}}{V_g} = -\beta = -\frac{1}{r \ln\left(\frac{r+d}{r}\right)}$$

This field factor is less than the field factor associated with the "ball in a sphere" model, which roughly implies that ridge-like structures are to be avoided in low voltage field emission or field ionization devices.

3.1.3 Bowling Pin model

Dvorson et al [26] have developed a more mathematically rigorous model for describing the field enhancement at emitting tips. Their model imagines the emitting tip as a cone with a small sphere centered at its apex. This model also confirms the intuitive expectation that

the field at the tip is most strongly dependent on the radius of curvature of the tip. However, their position is that the relationship is more closely approximated by

$$\beta \propto \frac{1}{r^{\nu}}$$

where $\nu \approx 0.8$.

The discussion of Dvorson et al is very instructive in understanding the physics of field enhancement and field emission, and coupled with other analytical models, provide a handy framework for predicting the behavior of cone-shaped field emitters.

3.1.4 Summary

All these analytical models predict a strong dependence of the field factor β on the tip radius. We will expect the numerical simulations to show as strong a dependence on the tip radius.

3.2 Discretization Methods in Electrostatic Modeling

Mathematical modeling is a process of simplification. However, models of physical systems are not necessarily simple to solve. They often involve partial differential equations in space and time which equations are also subject to boundary and/or interface conditions. Such models have an infinite number of degrees of freedom, even if, as with electrostatic models of physical systems, the time component of the differential equations is ignored. To make their numerical solutions practical, it is necessary to reduce the number of degrees of freedom to a finite number. This reduction is called *discretization.*

Two non-analytical methods for doing an electrostatic simulation are widely used in practice: Finite Element Method (FEM) and Boundary Element Method (BEM). Other methods like classical and energy-base exist but these will not be discussed here.

3.2.1 Finite Element Methods (FEM)

The finite element method is the dominant discretization technique in structural mechanics and is fast becoming the standard in electrostatic studies. The basic concept is the subdivision of the problem space into disjoint (non-overlapping) components of simple geometry called *finite elements*. The response of each element is expressed in terms of a finite number of degrees of freedom and can be fully solved analytically given a corresponding number of solution values at a set of nodal points on the element. The overall numerical solution is "correct" when the solution as determined for each finite element meets the overall boundary conditions and satisfies the system of equations that are being solved.

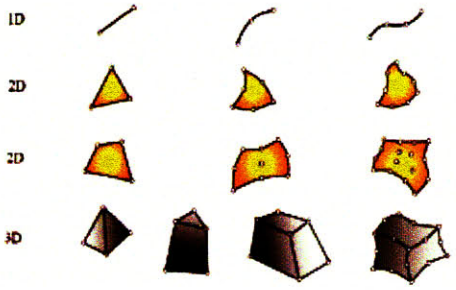

(a) Typical finite element geometries in one through three dimensions

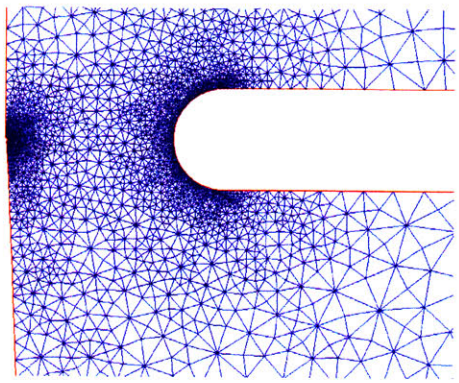

(b) Example solution space for 2D FEM

Fig. 3-1: Finite Element Geometries

For a 2D-solution space, the simplest finite elements are triangles as shown in Figure 3-1(a). As can be expected, full 3D finite element modeling is very much computationally expensive. The use of a 2D solution to simulate a physical system (predominantly 3D) makes the computation less intensive but limits us to models that are isotropically independent along at least one degree of freedom. Figure 3-1(b) demonstrates the solution space of a tapering carbon nano fiber surrounded by a rigid anode. This meshed solution space takes advantage of the axial symmetry of the problem under consideration to produce a 3D solution

without doing too much work.

3.2.2 Boundary Element Methods (BEM)

The BEM, also referred to as Boundary Integral Equation, uses elements along the boundary of the model, rather than throughout the model. It uses integral formulations of the applicable partial differential equations, ensuring that these equations are satisfied at every interior point of the model [28]. For 3D systems, this method uses nodal points on the boundary surface and points on the bounding curve for 2D systems. Given that only the boundary is solved, no internal mesh is required and so there are no unknowns associated with the interior points. BEM has been shown to be more computationally efficient than FEM when modeling 3D systems that do not permit a 2D simplification based on some symmetry [29].

In our work, we focus on finite element, rather than boundary element methods. Finite Element Methods are a good choice when the desired precision varies over the solution domain; this is certainly the case here where we really only care about the accuracy of the solution in the immediate vicinity of the tips.

3.3 Electrostatic Simulation

All electrostatic simulation in this work were done using the MATLAB Partial Differential Equation Toolbox (PDE Toolbox). The toolbox allows the use of scripts (m-files) to construct and solve models. The model geometries define 2D problems with associated boundary conditions and differential equation coefficients that can be easily plugged into the PDE Toolbox. Solutions can then be transferred to the traditional MATLAB workspace for further analysis. The electric field values in the vicinity of the tip were computed using the returned PDE solutions. These values were then applied to a routine that solves for the maximum

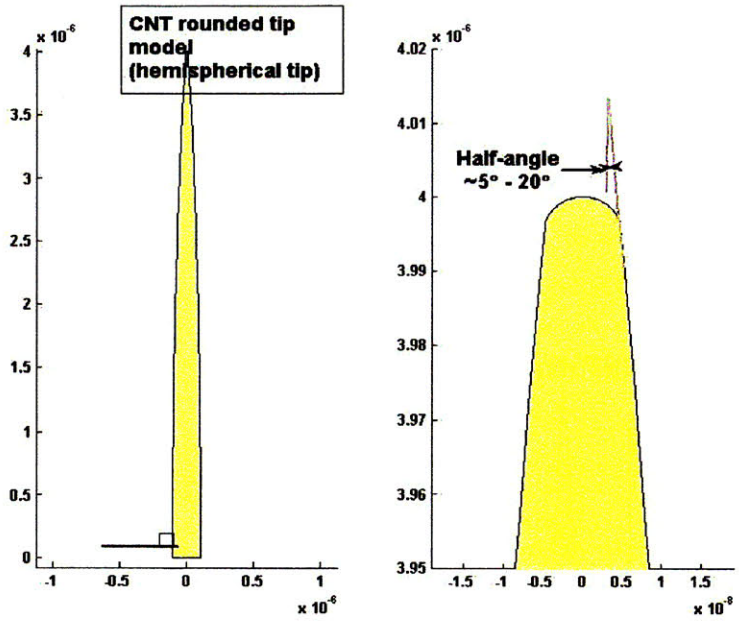

Fig. 3-3: CNT model (rounded tip)

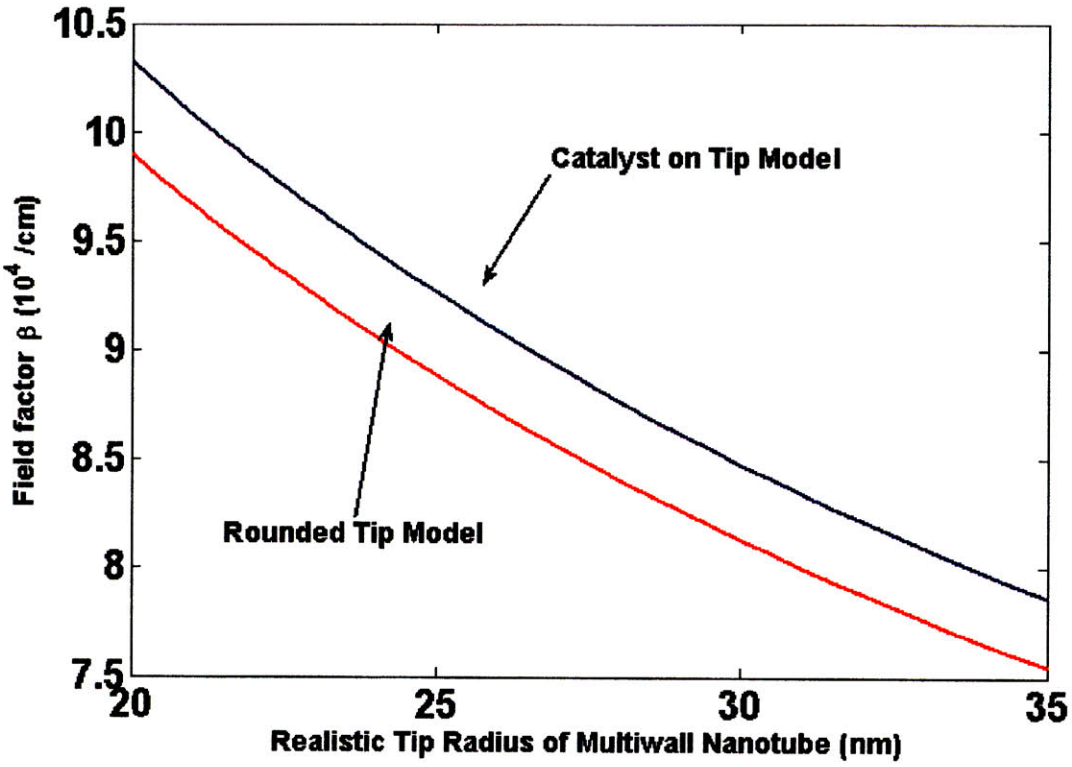

Fig. 3-4: Sensitivity of generated Field Factor to actual CNF tip radius

tunneling probability of a specific gas molecule (we explored field ionization from Hydrogen and Helium gases) along a specified path. A path-integration technique was then used to find the expected probability of ionization of a gas molecule entering the solution space.

3.3.1 CNT Model

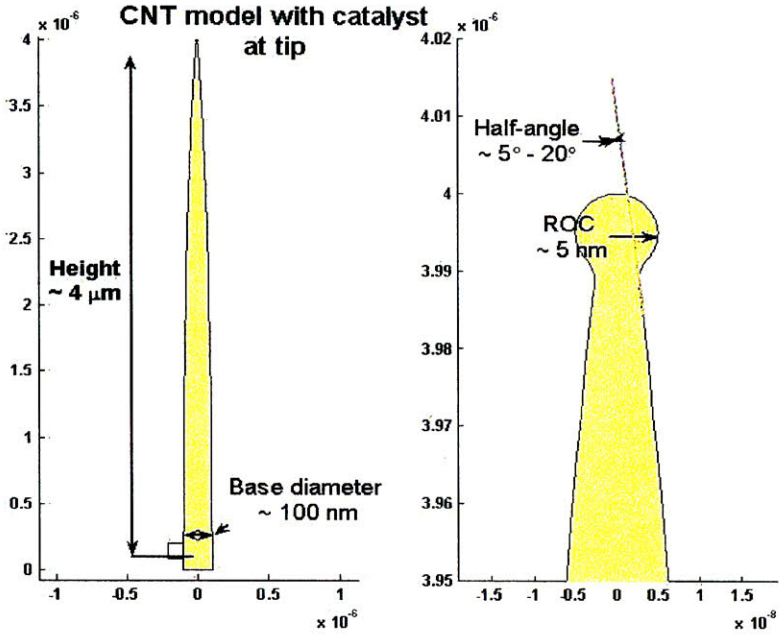

Fig. 3-2: CNT model (catalyst on tip)

Two main models were examined for the carbon nano fibers. The first model (Figure 3-2) puts the catalyst on the tip. This is an assumption from the fact that the fiber condenses on the bottom of the catalyst during the growth process. Hence, if it is not dislodged by the end of the growth, it stays on top of the CNF structure.

The second model (Figure 3-3) assumes a hemispherical tip. It assumes there are no dangling bonds at the end of the growth process and the nanofiber tip is "patched" similarly to the closely related fullerenes.

Within the range of tip radii expected of a multiwall carbon nanotube, we found that the

two models above yield similar field amplification factors, to within 25%. Figure 3-4 shows that the model with catalyst on the tip yields higher amplification, a result attributable to the increased curvature required by this model around its tip.

3.3.2 Solution Space

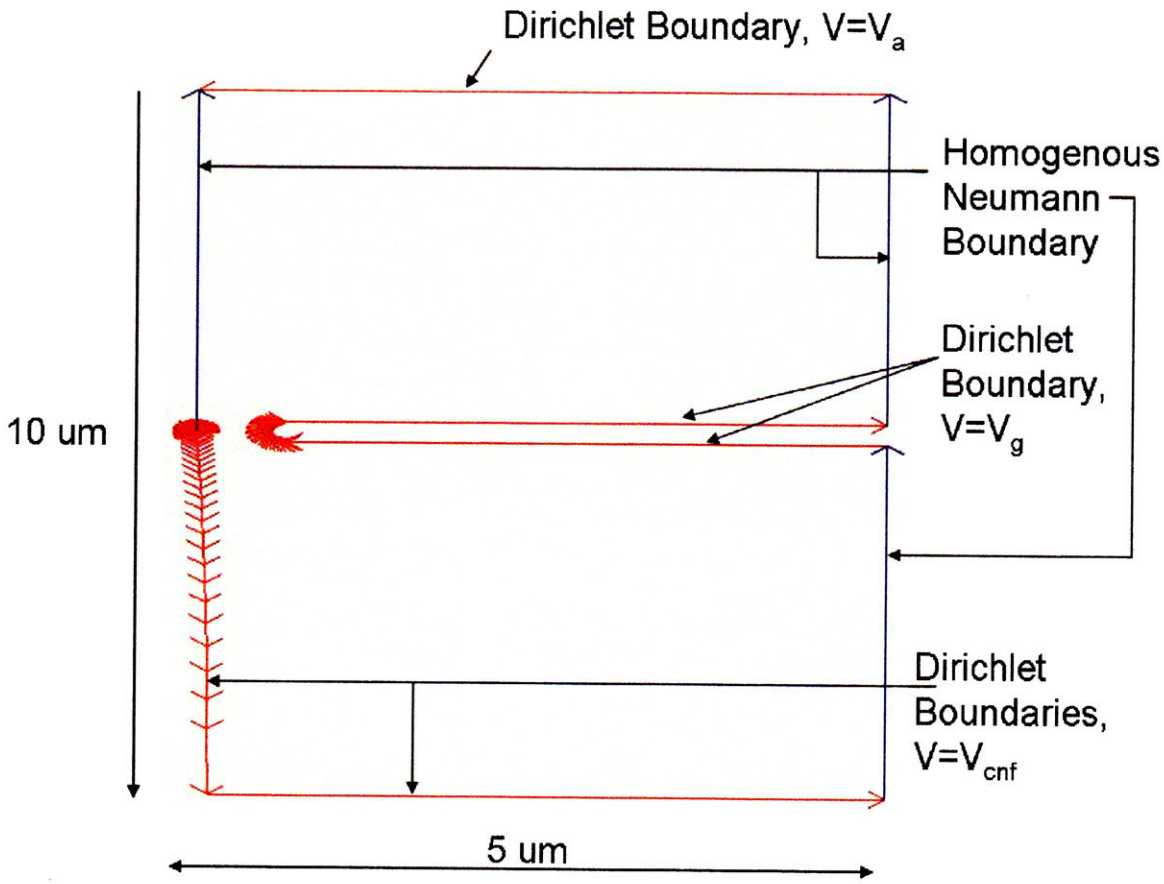

Fig. 3-5: Solution space with Boundary Conditions

The top edge of the solution space was set as a Dirichlet boundary with a voltage corresponding to the anode voltage V_a. Since this edge may not actually represent the anode in a real experiment, the value of the applied voltage will be scaled so that the constant "parallel-plate" fields seen by both experimental and simulated set-ups will be equal.

Going by a result from Pflug [27], the surface field solution converges to within $\pm 0.5\%$

of a stable solution when the top Dirichlet boundary is set at 10 times the gate aperture or more. In our simulations, the solution space was chosen to be 10 μm tall and 5 μm wide. This rather large space permitted a bigger graduation of the finite element triangles. That is, the refinement of the solution around the tips could be made much higher than elsewhere so that MATLAB spends significantly more processing time refining these areas.

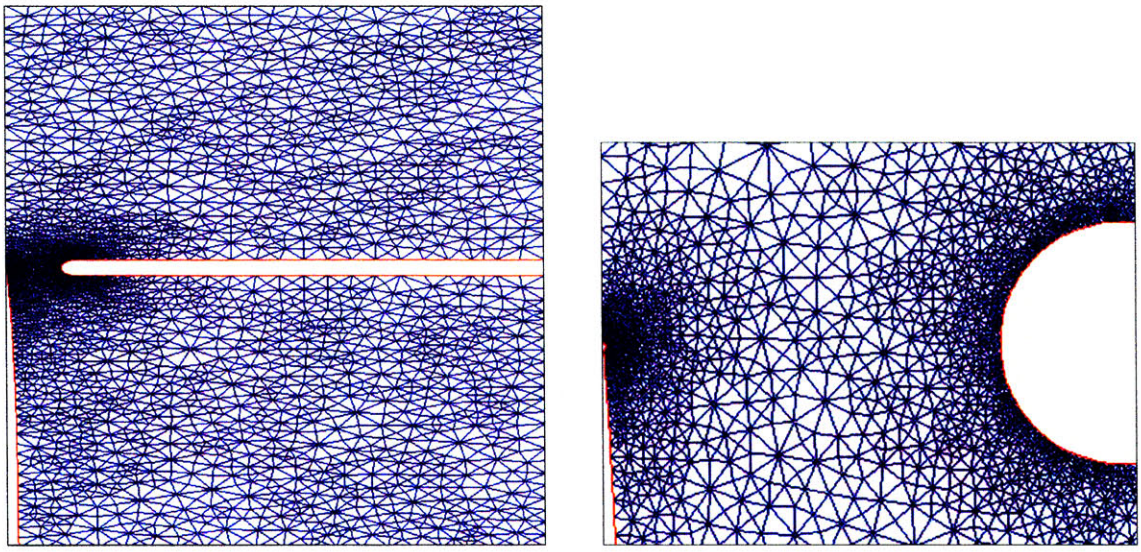

(a) Full solution space

(b) Zoom of solution mesh

Fig. 3-6: MATLAB-generated mesh of solution space. Notice that areas of high structural curvature have more elements, smaller and more densely packed

Figure 3-7 shows a typical shot of the MATLAB-generated potential lines of the solution space. The device model has been put in the field ionization configuration. Thus, a positive voltage is applied at the tip and a large negative voltage is applied at the top of the solution space. The bigger and longer arrows around the tip area signify the field amplification in that vicinity. Figure 3-7 also highlights the position of the tip itself on the left boundary and the fact that only half of the tip surface area has been used in this 2D simulation of the axially symmetric 3D space.

Since the CNT, the gate and the top boundary are Dirichlet boundaries with constant potentials, the electric potential lines close to these surfaces are compelled to be parallel to

them. Conversely, the three Neumann boundaries (Figure 3-5) have potential lines running perpendicular to them.

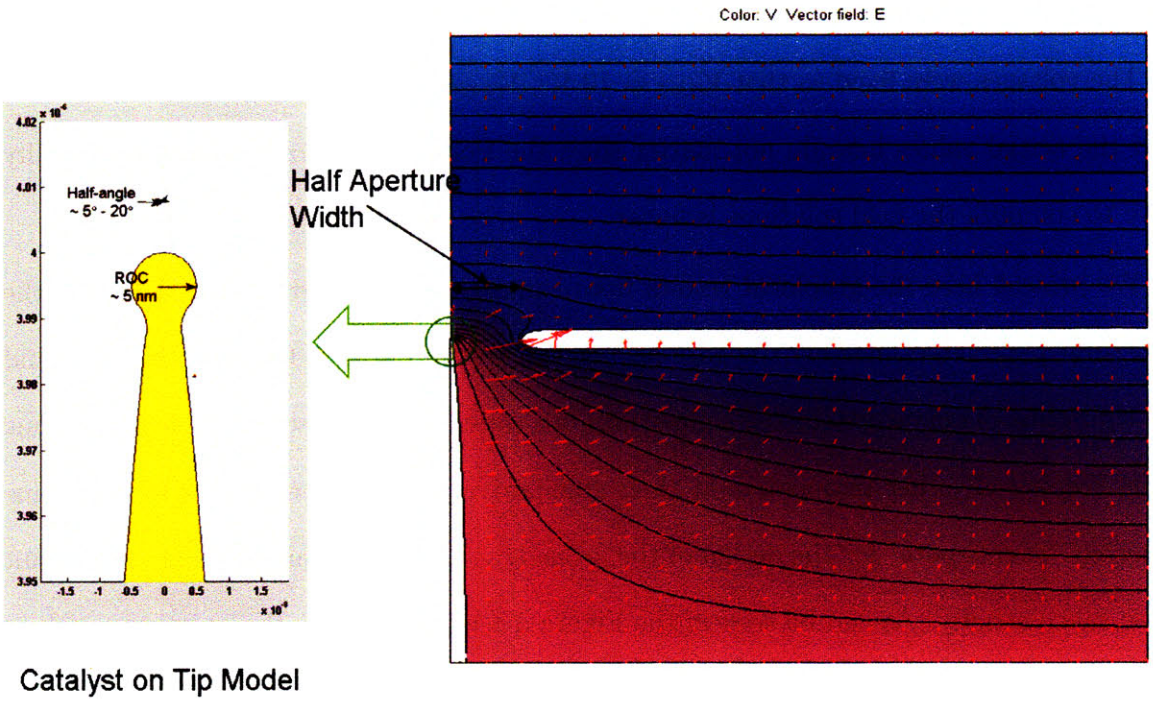

Fig. 3-7: Electric Potential Lines of a typical Field Solution

3.3.3 Simulation Results

3.3.3.1 Standard Parameters and Brief Description

In our simulations, we took the following structural parameters as standard:

CNT: roc = 5.01 nm, height= 5.1605 μm — Base:- angle=85, radius= 101 nm

GATE: aperture=1.01 μm, thickness= 0.301 μm, height= 5.01 μm

$$V_{CNT} = 10\ V \quad V_{GATE} = 0\ V \quad V_{ANODE} = -10\ V$$

The standard height of the CNTs was chosen to be 5.1605 μm while the standard *tip* radius of curvature was set at 5.01 nm. Their base radii were fixed at 101nm. The standard

height of the gate was chosen so that the tip of the CNT is at the same level as the vertical center of the gate. The standard gate height was 5.01 μm while the standard gate thickness was 0.301 μm. The standard gate aperture was 1.01 μm.

The voltages were fixed so that $V_{CNT} = 10\ V \quad V_{GATE} = 0\ V \quad V_{ANODE} = -10\ V$. Note that the actual values here do not matter since the Poisson equation that we numerically solve to compute the field solutions is linear.

We present here the graphical results from simulations in which we varied four of the structural parameters, namely the gate height, the aperture width, the gate thickness and the tip radius of curvature. In the simulations, we varied one of these parameters at a time while keeping all other parameters at their standard values. This was done to determine expected "sweet spots" for the design of the geometry. These determinations are not meant to be taken strictly. As can be seen in the Figure 3-8 where we vary the aperture width to Figure 3-11 where we vary the gate thickness, the range of variation of the field factors when the geometry changes can be quite small. We shall now go into further detail.

3.3.3.2 Varying Aperture Width

We varied the aperture size from $0.15\mu m$ to $3.3\mu m$ in steps of $0.101\mu m$. Within this range, the field factor β fell from $6 \times 10^5 volts/cm$ to about $13 \times 10^4 volts/cm$. As we varied the aperture size, we also varied the width of the solution space to make sure that our field solutions were convergent in each iteration of the simulation. One of Pflug's results was that the surface solution converges to within 0.5% when the solution space width is at least thrice the aperture width [27]. Therefore, we reset the width of the solution space in each iteration, taking care to enforce a minimum solution space width of $3\mu m$ because MATLAB's PDE solver could not mesh the solution space properly whenever the aspect ratio of the solution space was higher than 3. We discovered this minimum aspect ratio by trial and error. All

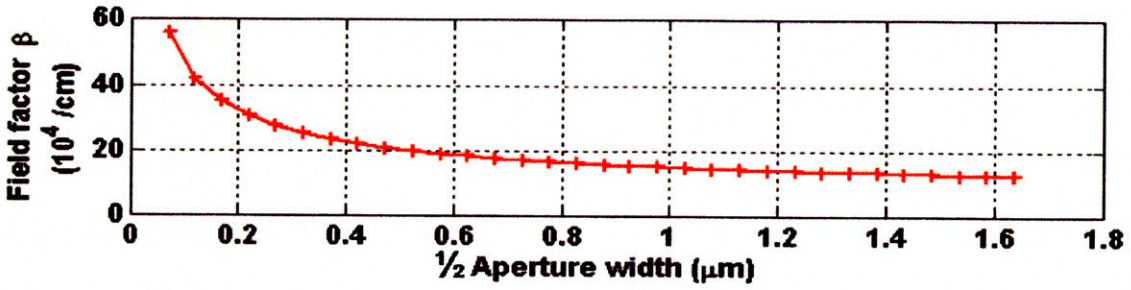

(a) Plot vs. $\frac{1}{2}$(Aperture Width)

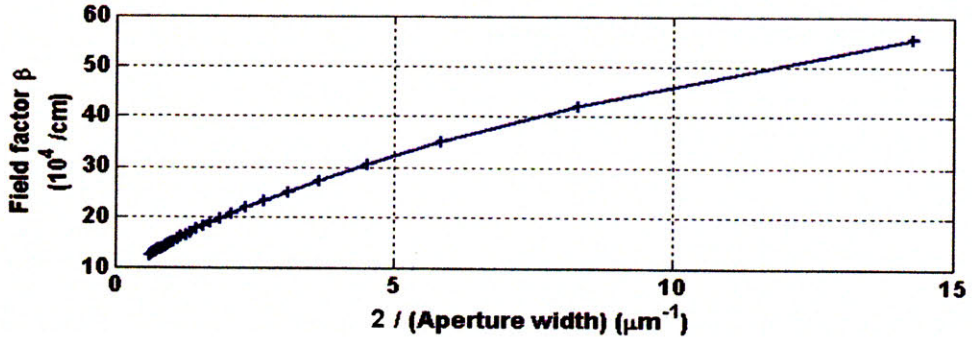

(b) Plot vs. $\frac{2}{\text{Aperture Width}}$

Fig. 3-8: Field Ionization simulation: Varying Aperture Width

other structural parameters were kept at their standard values as defined in section 3.3.3.1. At each value of the aperture size, we computed the surface electric field F_0 and divided this by the applied emitter voltage V_{CNT} to obtain the field amplification factor β.

We then created two plots. In the first plot (Figure 3-8(a)), we plotted the calculated values of β against half the aperture size, which would correspond to the radius of a round aperture. The plot clearly shows that β is a decreasing function of the aperture size. The second plot (Figure 3-8(b)) shows β against $\frac{1}{\frac{1}{2}*\text{aperture width}}$ or equivalently $\frac{2}{\text{aperture width}}$. In this second plot, we clearly see that β is very close to being inversely proportional to the aperture size. The result from this simulation seems to bear out the "Ball in a Sphere" model which includes an explicit β-dependence on $2d$, the aperture width: $\beta = \left(\frac{1}{r} + \frac{1}{d-r}\right)$. Unfortunately, we did not vary $2d$, the effective aperture width, high enough that we might begin test that model in the regions where the first plot (Figure 3-8(a)) might have flattened out and thus provide strong corroboration for the "Ball in a Sphere" model.

3.3.3.3 Varying Gate Height

In these simulations, we swept the height of the gate from $0.5\mu m$ to $2\mu m$ in steps of $0.101\mu m$ and from $2\mu m$ to $13\mu m$ in steps of $0.5\mu m$. We updated the height of the solution space in each simulation, for similar reasons as our reasons for updating the solution space width during the aperture width simulations in section 3.3.3.2. In this case, we not only needed to make sure that the solution space was taller than 10 $\times$ the *aperture width*, but also needed to make sure that the top boundary of the solution space was at least half as tall as the gate. This was done to make sure the gate always exert more electrostatic influence on the tips than the anode (top boundary). All other structural parameters were kept at their standard values as defined in section 3.3.3.1, especially the gate height whose constant height is shown in the figure 3-9. At each value of the gate height, we computed the surface electric field F_0

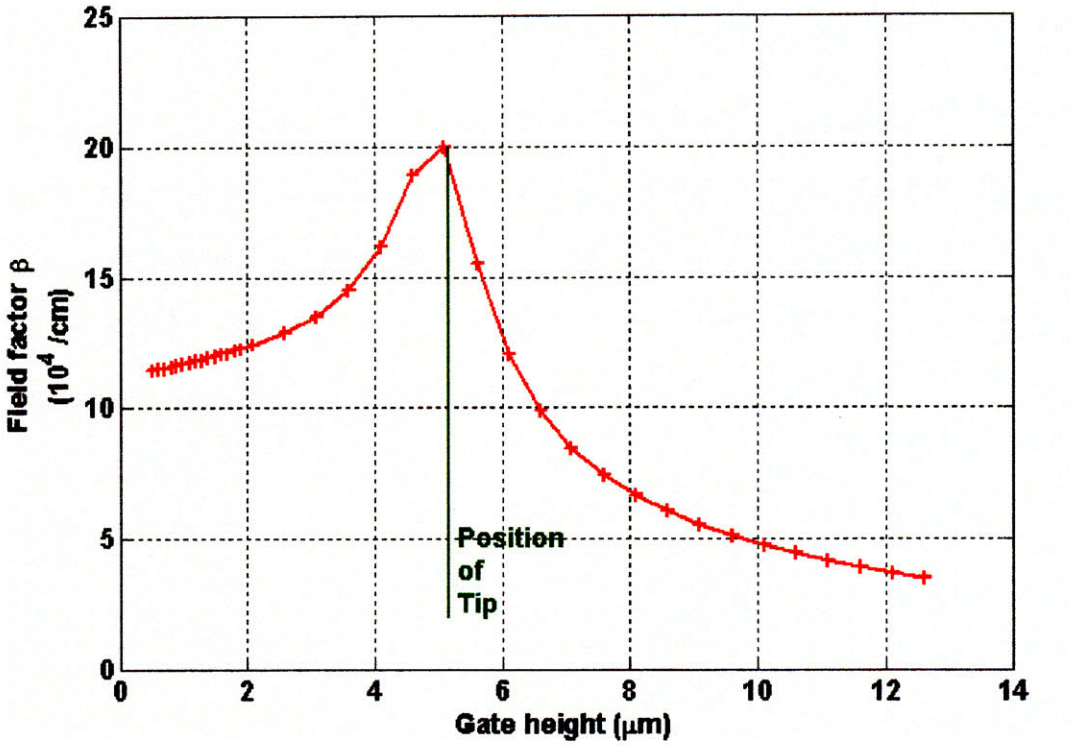

Fig. 3-9: Field Ionization simulation: Varying Gate Height

and divided this by the applied emitter voltage V_{CNT} to obtain the field amplification factor β. The gate is allowed to tower above the tip and vice versa. The constant position (height) of the tip is marked by the vertical line.

The results show that the maximum field factor occurs when the gate lies slightly below the top of the tip. For the tip fixed at $5.1605\mu m$, the results show that the optimum gate height is about $5.01\mu m$. This is why we chose the standard values as we did in section 3.3.3.1 in the first place. Also, because the right tail is taller than the left tail, we conclude that it is better to have shorter CNT than a taller CNT. Therefore, we will always veer towards the short end of the height range when making any fabrication choices.

3.3.3.4 Varying Tip Radius of Curvature

We varied the tip radius of curvature r from $2.51nm$ to $15.1nm$ in steps of $0.101nm$. All other structural parameters were kept at their standard values as defined in section 3.3.3.1 without exception. At each value of the tip radius of curvature, we computed the surface electric field F_0 and divided this by the applied emitter voltage V_{CNT} to obtain the field amplification factor β. The simulation yielded the expected result that β is strongly dependent on r.

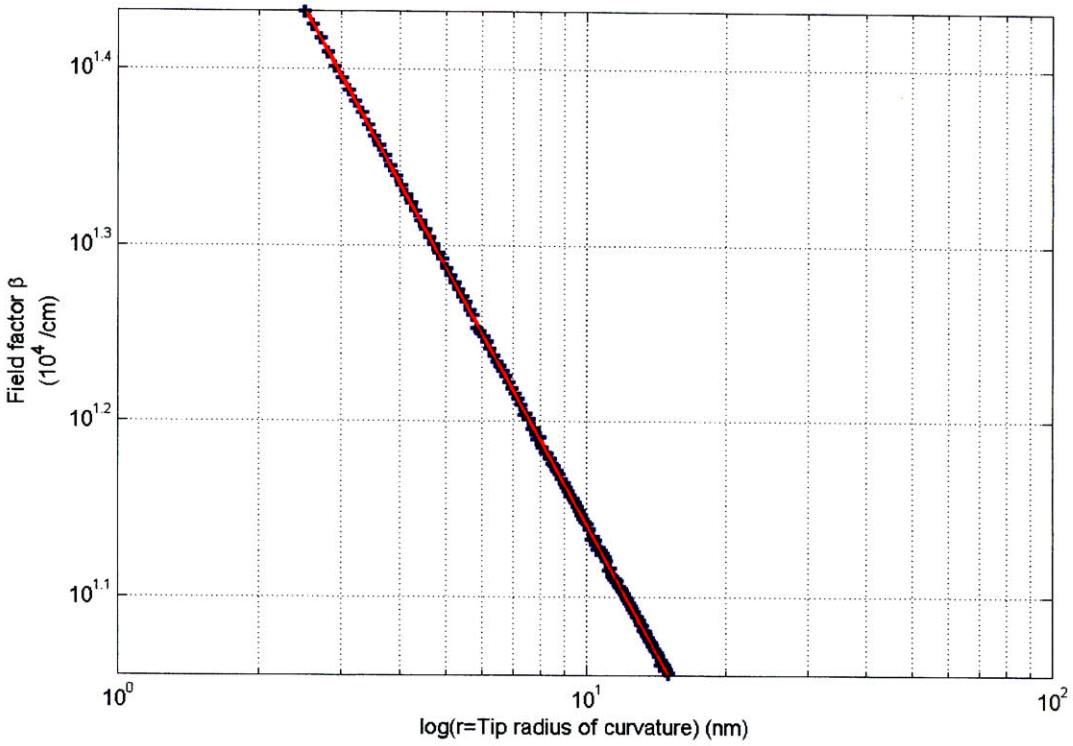

Fig. 3-10: Field Ionization simulation: Varying Tip Radius of Curvature

We put the calculated values of β into a plot of $log(\beta)$ against $log(r)$, expecting a strong linearization that would support at least one of the analytical models we looked at earlier (section 3.1). The resulting curve in Figure 3-10 was fitted to $\beta = \frac{42.4325}{r^{0.48579}}$ This seems to confirm Dvorson's result that the relationship between β and the tip radius of curvature is not simple inverse proportionality [26].

3.3.3.5 Varying Gate Thickness

In these simulations, we varied the thickness of the gate from $100nm$ to $600nm$ in steps of $5nm$. Since we already had the result that the gate height should follow the tip height and vice versa (section 3.3.3.3), we fixed the top of the tip at the same height as the gate's mid height in each iteration. All other structural parameters were kept at their standard values as defined in section 3.3.3.1 without exception. At each value of the gate thickness, we computed the surface electric field F_0 and divided this by the applied emitter voltage V_{CNT} to obtain the field amplification factor β. We obtained a weak linear relationship between β

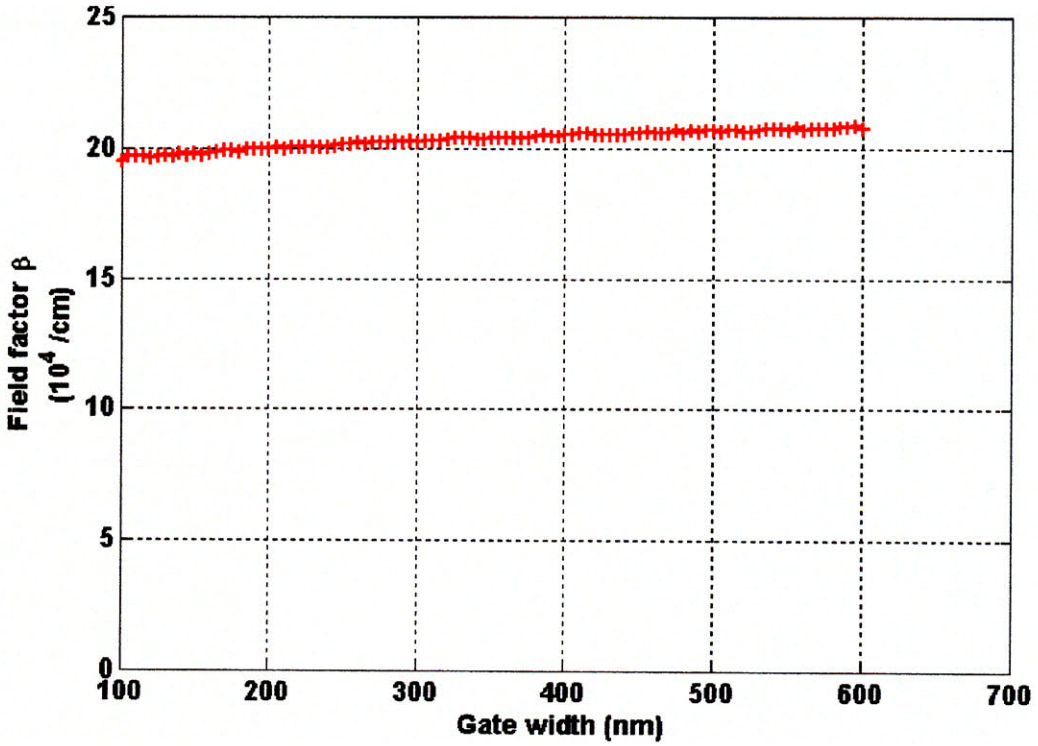

Fig. 3-11: Field Ionization simulation: Varying Gate Thickness

and the gate thickness, as shown in Figure 3-11. This result can be interpreted as follows. As long as the gate remains close to the tip, the thickness of the gate thickness will have no effect on the field amplification characteristics of the device. Therefore, in our fabrication, we will not attempt to optimize the gate thickness for the purpose of maximizing the field

amplification; for this purpose, we willl focus on optimizing the tip radius of curvature, and the gate and tip heights.

3.3.3.6 Optimum Height of Tip and Gate

Since we observed a strong maxima where the gate and CNT were at about the same heights, we performed an additional simulation where we varied the heights of the tip and gate in tandem so that the gate is always optimally located relative to the tip, and kept all other structural parameters standard (excluding the height of the solution space which we updated as described in section 3.3.3.3 while varying the gate height). This simulation yielded an optimum height for both tip and gate as shown in Figure 3-12.

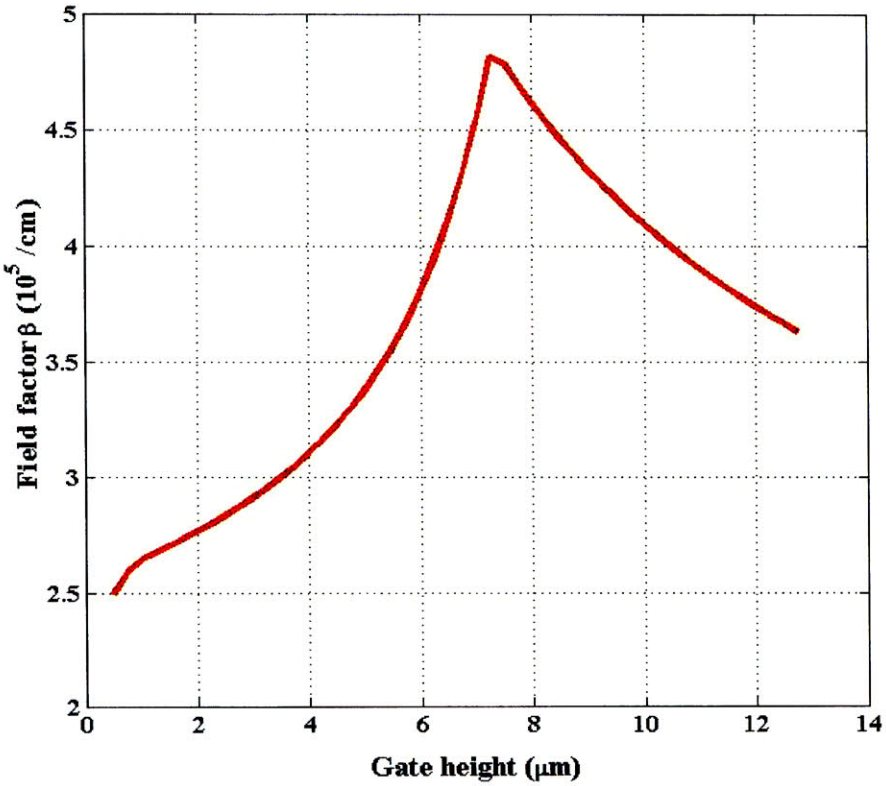

Fig. 3-12: FI Field factor β for various heights of gate. Tip height was varied in sync with gate height so that the tip remained within the range of the gate width

The value of this optimum height would depend, among other variables, on the electrostatic properties of the insulating material and the actual dimensions of the rest of the structure. However, we would not expect a strong dependence on the tip radius of curvature. An interesting simulation would attempt to determine various values of the optimum heights for various structural configurations of the device.

3.3.3.7 Summary of Simulation Results

The non-smoothness apparent in some of the plots is due to numerical errors in the MATLAB PDE solver. As expected, the tip radius of curvature has the strongest effect on the field amplification factor while varying the tip base angle barely modulates the amplification at all. The results of the simulations are summarized in the table below:

Table 3.1: Table showing summary of simulation results

Vary Parameter	**From**	**To**	**Updated Parameters**	**Maximum in Range?**	**Increasing or Decreasing function?**	**Optimize in Fabrication Design?**
Aperture Width	$0.15\mu m$	$3.3\mu m$	Solution Space Width	no	decreasing	no
Gate Height	$0.5\mu m$	$13\mu m$	Solution Space Height	yes		yes
Tip ROC	2.51nm	15.1nm		no	decreasing	yes
Gate Thickness	100nm	600nm	Tip/Gate Height	no	increasing	no

3.4 FI Tunneling Probability

3.4.1 Preliminary 1D Calculations

Here, we assume that the field in the immediate vicinity of the tip is constant. This assumption will be rescinded in section 3.4.2 where we include the electrostatic simulation results from section 3.3.

The WKB approximation admits the following expression for the tunneling probability of an electron:

$$D = exp\left\{-2\sqrt{\frac{2m_e}{\hbar^2}}\int\sqrt{V(x)-W}dx\right\}$$

where

$$\begin{aligned}
D &= \text{tunneling probability} \\
m_e &= \text{mass of electron} \\
V(x) &= \text{potential seen by electron} \\
&= \underbrace{\left\{-2I+\frac{Z_{eff}q}{4\pi\varepsilon_0}\left(\frac{1}{r_0}-\frac{1}{r}\right)\right\}}_{\text{molecular potential}} + \overbrace{\left\{-\frac{3.6}{\left(x+\frac{3.6}{\phi}\right)}\right\}}^{\text{image potential}} + \underbrace{\{Fx\}}_{\text{applied field}} \\
W &= \text{total energy of electron} \\
I &= \text{ionization potential} \\
r_0 &= \text{atomic radius} \\
\phi &= \text{work function of tip material}
\end{aligned}$$

In all calculations, 0 is considered to be the vacuum energy. The expression for $V(x)$ includes a correction factor of $-2I$ which maintains the limiting conditions $V(\infty) = 0$ and $V(r_0) = -2I$. But why is $V(r_0) = -2I$? One must be careful not to include the kinetic energy of the electron in the expression for the potential well. The **total energy** of the unperturbed electron is $-I$. In the Bohr model, the potential energy of the orbiting (rest)

electron is twice as large as the kinetic energy, but negative.

$$E_{total}(r_0) = KE(r_0) + PE(r_0) = -I$$

$$PE = -2KE \Rightarrow \frac{PE}{2} = -I \Rightarrow PE(r_0) = -2I$$

$$V(\infty) = -2I + \frac{Z_{eff}q}{4\pi\varepsilon_0 r_0} = 0 \Rightarrow r_0 = Z_{eff}\frac{q}{4\pi\varepsilon_0}\frac{1}{2I} = 7.197\frac{Z_{eff}}{I}\mathring{A}$$

In plotting the potential well of Figure 2-3 reproduced in Figure 3-13 for convenience, we introduce a correction factor for the image potential that requires the sum of the applied and image potentials to equal the potential at the top of the metal conduction band. Hence:

$$\left(Fx - \frac{3.6}{x+d}\right)|_{x=0} = -\phi \Rightarrow d = \frac{3.6}{\phi}$$

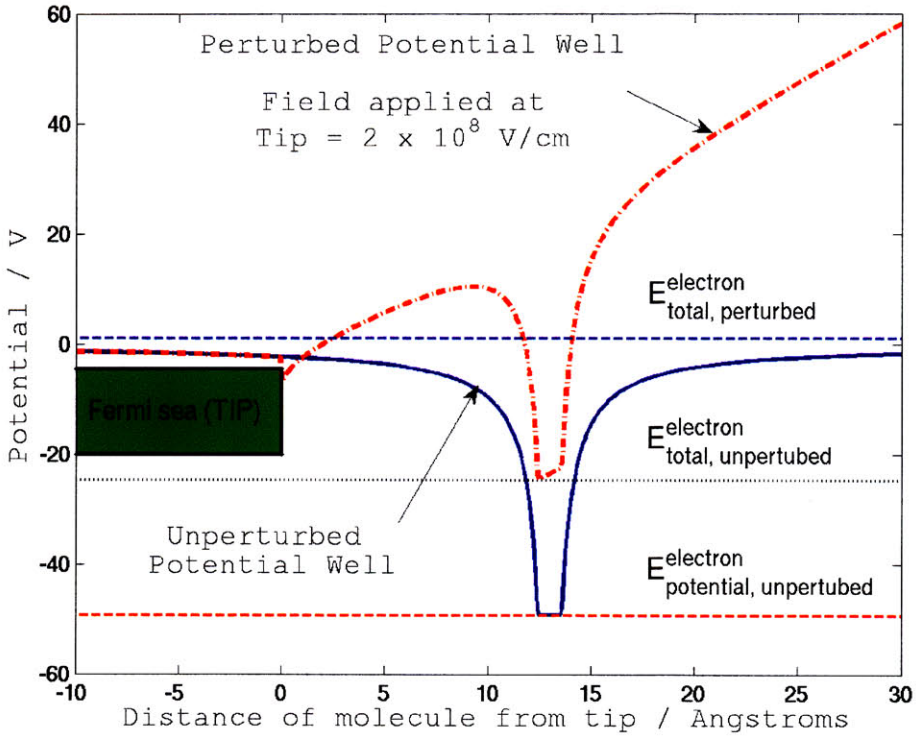

Fig. 3-13: Potential Well of an Helium electron in the Field Ionization scenario

There are more accurate ways to model this correction [34] but they involve extensive numerical calculations that are very difficult to simplify. They might however turn out to be important for future work because the current correction reduces calculated probabilities by as much as an order of magnitude.

The total energy of the electron depends on the position of the gas molecule relative to the metal tip. The closer the molecule gets to the surface, the lower the total energy of electrons bound to the molecule. Hence, there is a critical distance where the energy of the electron equals the Fermi level for electrons in the bulk of the metal. If the molecule gets any closer, the electron would be tunneling from a total energy less than $-\phi$ into electron states that are completely filled. Recall that all electron states below the Fermi level are completely filled in a metal. Therefore, assuming a constant field value F close to the surface, critical distance of approach $x_c \cong \frac{I-\phi}{F}$. The total electron energy at x_c is therefore $W(x_c) = -I$.

Calculations of potential fields and tunneling probabilities at distances x further away from the tip surface than x_c are done as follows:

1. Shift the unperturbed potential well by $(x - x_c)$ to the right

2. Set

$$\begin{aligned} W(x) &= \text{total electron energy at position } x \\ &= W(x_c) + \Delta \text{ (potential from applied and image potentials)} \\ &= W(x_c) + P_w(x) - P_w(x_c) \end{aligned}$$

OR equivalently,

$$W(x) = P_w(x) - I$$

since the electron still requires that amount of energy to escape into vacuum

Note that $P_w(x)$ = sum of applied and image potentials at location x

3. Perform computations of tunneling probability using WKB expression for D

Example plots of the results can be found in Figure 3-14, where molecular specifications for the Helium atom were used. The plots show that the field ionization tunneling probability

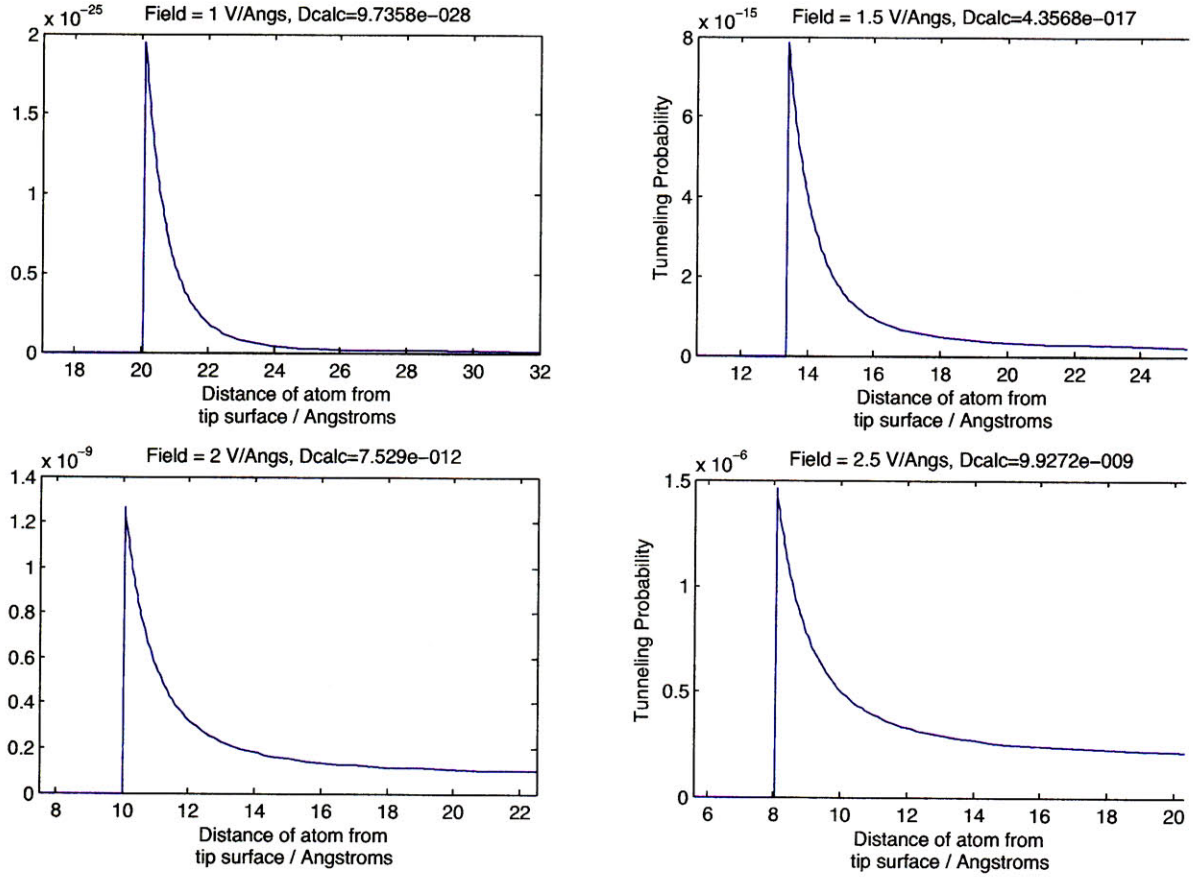

Fig. 3-14: One-dimensional WKB numerical solutions for the tunneling probability of He The sharp cut-off in each of the plots represents the critical distance x_c that was mentioned earlier. Electrons in molecules closer than x_c to the tip surface cannot tunnel out because there are no states for them to occupy on the other side of the potential barrier

of the tunneling electron depends strongly on the molecules distance from the field-generating tip close to the tip surface. Far from the surface, the tunneling probability is not strongly position-dependent. In the simulations, the electric field around the tip was assumed to vary linearly when a constant voltage is applied to the tip. While this approximation is inaccurate for any tip with any kind of curvature, it is acceptable for the small distances

under consideration (measured in angstroms). The size of an atom is measured in angstroms; one would not expect the electric field within an atom to vary much, especially at the high voltages being applied.

3.4.2 Extending to Include Electrostatic Simulation Results

A key assumption in the calculations in section 3.4.1 was that the electric field was constant in the region for which the calculations were performed. Here we note a method of removing that simplification and extending those calculations to 2D or 3D non-uniform fields.

The extension is relatively simple once the 1D calculations in section 3.4.1 are correctly done. Given the electrostatic simulations, it is a straightforward matter to calculate the electric field at every location in the solution space. Then, the 1D calculation routines can be applied to compute the tunneling probabilities at every location! Figure 3-15 attempts to illustrate this calculation for all points in an imaginary vertical cylinder of height $100nm$ and radius $100nm$ positioned so that the tip is at the center of the bottom disk of the cylinder. The plot assumes independent cylindrical co-ordinates: r = radial distance from tip in nm and h = the vertical distance from the tip also in nm. This means that the tip is at the location $(0, 0)$. As the figure shows, the tunneling probability is greatest very near to the tip. It is easy to see that the tunneling probability contours represent spherical contours in real space once we realize that the distance between two points in 3-dimensional space is exactly $\sqrt{r^2 + h^2}$. Figure 3-15 also shows the corresponding electric field solution in the same domain; the solutions are of the standard device dimensions we defined for our simulations in section 3.3.3.1.

We define the probability that a single incoming molecule get ionized as the maximum tunneling probability along its path in the solution space. This relation is not perfectly accurate because polarization forces will affect the path of any incoming particles and these forces in turn depend on the local electric fields. Therefore, the accurate solution would define an initial position and velocity for the particle and compute both its trajectory and

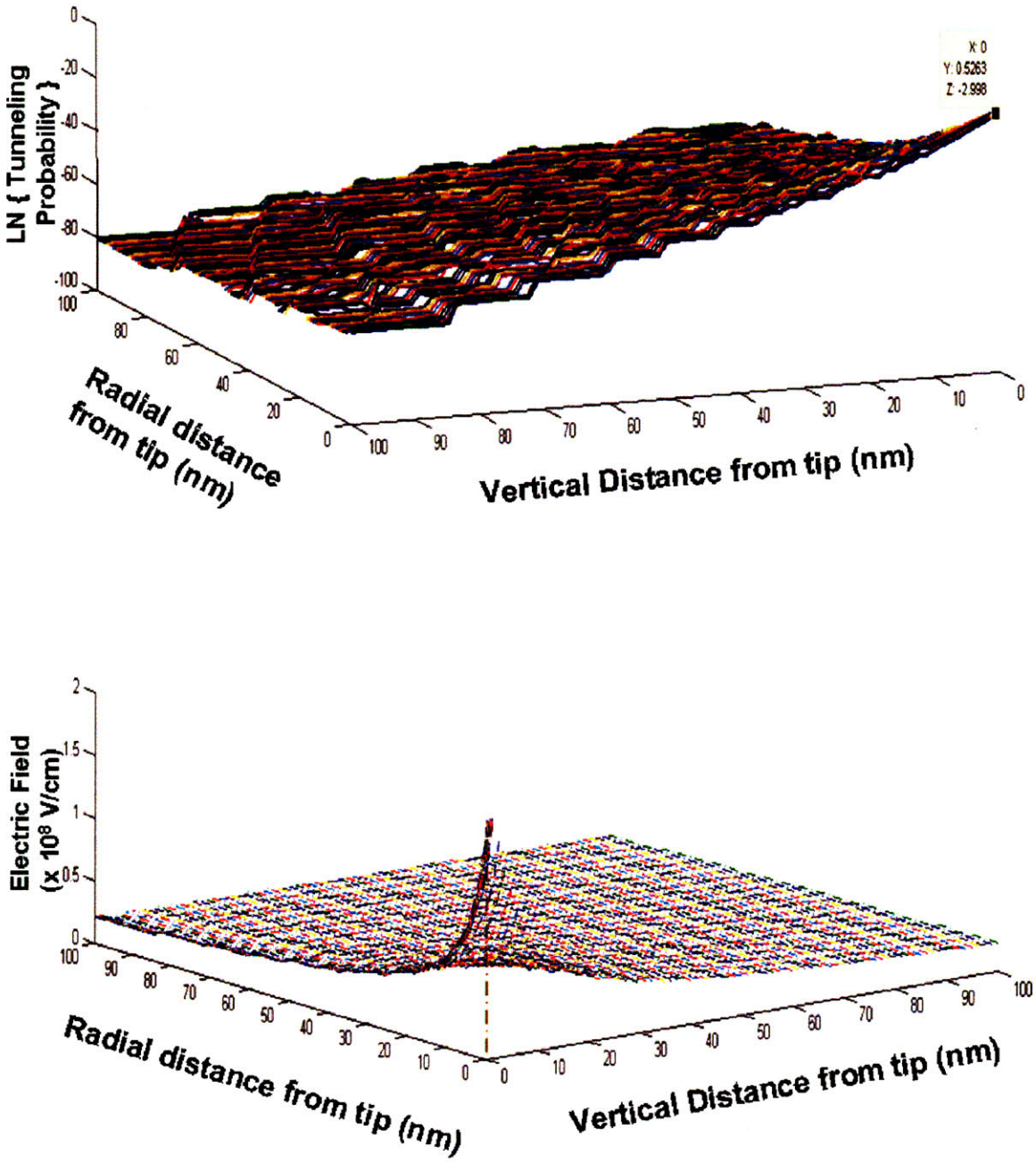

Fig. 3-15: Typical Tunneling Probability Solution in 3-Dimensions

tunneling probabilities along that trajectory using the electric field solution. In this work, we simply the problem by ignoring the effect of these trajectory corrections.

3.5 Summary

All the analytical models examined and our numerical simulations point to a strong dependence of the field amplification factor on the tip radius. This will inform our decision in chapter 5 to grow our device CNTs with the goal of minimizing the tip radius. The results of the numerical simulations suggest that the Bowling Pin Model [26] is the most accurate of the analytical models examined.

We used numerical simulation to predict the performance of our devices. The simulation results also helped us to design a target geometry for the fabrication stage of this work. The results suggest that a CNT and gate height of between 6 and 8 μm is optimal, with as small a tip radius as is possible. We will not attempt to optimize the gate thickness or CNT base angles since the simulation plots for varying these parameters indicate that such effort would not be effective. The results also suggest that we should make the aperture width as small as possible.

In addition, we estimated the tunneling probabilities of molecules close to the tip surface. Our results indicate that we should expect much of the soft ionization to take place in a narrow ($\frac{1}{2}nm$) shell around the CN tip.

4 CNF Growth

4.1 Introduction to Carbon Nanotubes

Since their discovery in 1991 [36], carbon nanotubes have attracted considerable attention because of their fascinating structure and properties. Broadly classed either as single-walled nanotubes (SWNT) or multi-walled nanotubes (MWNT), the latter consisting of nested shells of the former, many methods have been developed for their synthesis and manufacture, either as free-standing material or grown off a substrate. A SWNT consists essentially of a graphene sheet rolled into a cylinder, any particular nanotube being defined by its diameter and chirality with respect to the graphene sheet. A SWNT can have a diameter as small as $0.4nm$, containing only about 10 atoms around the circumference, with a thickness of only 1 atom [37]. One of the most striking characteristics of nanotubes is that their electrical properties depend very sensitively on structure; a nanotube can either be metallic or semiconducting [38]. These structural, electrical *and* mechanical properties of nanotubes have inspired considerable interest in their application in a myriad of nanoelectronic devices [39], scanning probes [40], field-emission sources [41], and super-capacitors [42].

Typically, experimental techniques for the production of carbon nanotubes result in a mixture with differing diameters and chirality. The nanotube material produced by the presently available synthesis methods, including laser vaporization, carbon arc discharge, vapor phase deposition, and solar energy synthesis, appears in a scanning electron microscopy (SEM) image as a mat of carbon nanotubes bundles $10-20nm$ in diameter and up to $100mm$ or more in length and containing between 30-500 SWNTs [43]. Consequently, considerable

effort has been expended on techniques for functionalizing, dispersing and cutting them. Nevertheless, separation and precise placement of CNTs remains quite difficult [44].

A lot of research has also gone into perfecting procedures by which high yield, uniform, and preferential growth of perfectly aligned nanotubes can be achieved. One such process is plasma-enhanced chemical-vapor deposition (PECVD) [45]. By using a regulated mixture of acetylene and ammonia, it is possible to grow uniform arrays of vertically aligned nanotubes at precise locations on silicon substrates via lithographic patterning [45] (see Figure 4-1). This is the method we have been working with.

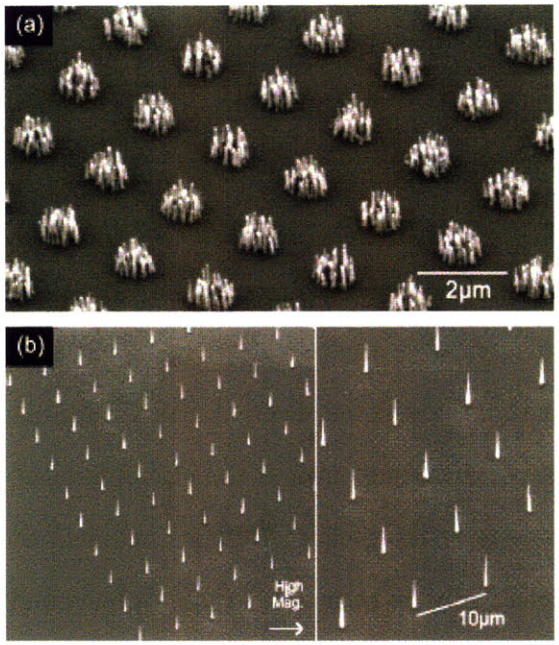

Fig. 4-1: (a) Bunches of nanotubes ($100nm$ in diameter) are deposited on 1 micron nickel dots because the nickel catalyst film breaks up into multiple nanoparticles. (b) Single nanotubes are deposited when the nickel dot size is reduced to $100nm$ as only a single nickel nanoparticle is formed from the dot (Image taken from [45])

4.2 Growth Process

To grow our CNTs, we deposit a thin film of Nickel (Ni) on a silicon substrate wafer. Sandwiched between the Ni and the Si is a $50nm$ film of titanium nitride TiN that serves

as a diffusion barrier. The diffusion barrier is necessary because Ni diffuses into Si to form $NiSi_x$ at temperatures above 450C [46]. Typically, between $5nm$ and $12nm$ of Ni catalyst is deposited. The wafer is then subjected to low pressure annealing at a temperature of 675C for 5 minutes. Annealing takes place in an ammonia (NH_3) gas environment. Its purpose is to break up the Ni film into nanoclusters, from which the CNTs grow. Actual growth is done by passing a mixture of NH_3 and acetylene under plasma at $3.5mbar$[47]. The voltage drop in the plasma sheath generates an electric field perpendicular to the surface, and this helps to vertically align the growing tubes [33]. However, for a dense forest of CNTs as can be expected using an unpatterned Ni film, the plasma is not really needed for alignment. This has been verified by experiment. Since the tubes on an unpatterned Ni surface grow in very close quarters, each growing tube is aligned by its closest neighbors.

The ratio of NH_3 to C_2H_2 used for the growth is very important. When more than 30% C_2H_2 is passed, too much amorphous carbon(a-C) is deposited on the surface along with nanotubes. *The condensation of a-C occurs only in the presence of plasma* [45]. A possible explanation goes as follows. Ion species in the system enter the plasma sheath and are accelerated toward the surface by the high electric fields within the sheaths. Not all the ions participate in the CNT growth mechanism since the *growth occurs only where there is an unsaturated nickel or carbon nanoparticle.* This means that some carbon will aggregate on the surface as (a-C), forming a conductive layer that is undesirable for microelectronic applications. NH_3 serves to counteract the formation of this so-called a-C layer by etching carbon. Unfortunately, the desirable carbon in the nanotubes does not escape this reducing treatment. Hence, there exists a lower limit for CNT deposition when too much NH_3 is passed into the system. Anisotropic etching of the Si substrate has been observed when the C_2H_2 concentration is 15% or lower [45], indicating that the etching from NH_3 is greater than the deposition of a-C.

Why use plasma at all if it causes so much trouble? First of all, the tubes in our target array must be spaced at least twice their height to avoid electric field screening. This

means the Ni has to be patterned for an actual field emission device. Also, to achieve good structural uniformity (similar diameters and heights), it is necessary to pattern the Ni catalyst into nano-sized dots [47]. When unpatterned, the catalyst film coalesces into nanoclusters of different sizes, leading to uneven CNTs of different diameters. Since carbon supply is approximately the same for each growing tube, variations in diameter lead to inverse variations in height. This is the same as saying that different-sized nanoclusters will lead to CNTs of different heights. Logically, this also implies, and is implied by, the fact that thicker catalyst films will lead to taller CNTs as has been observed by Ren et al [35].

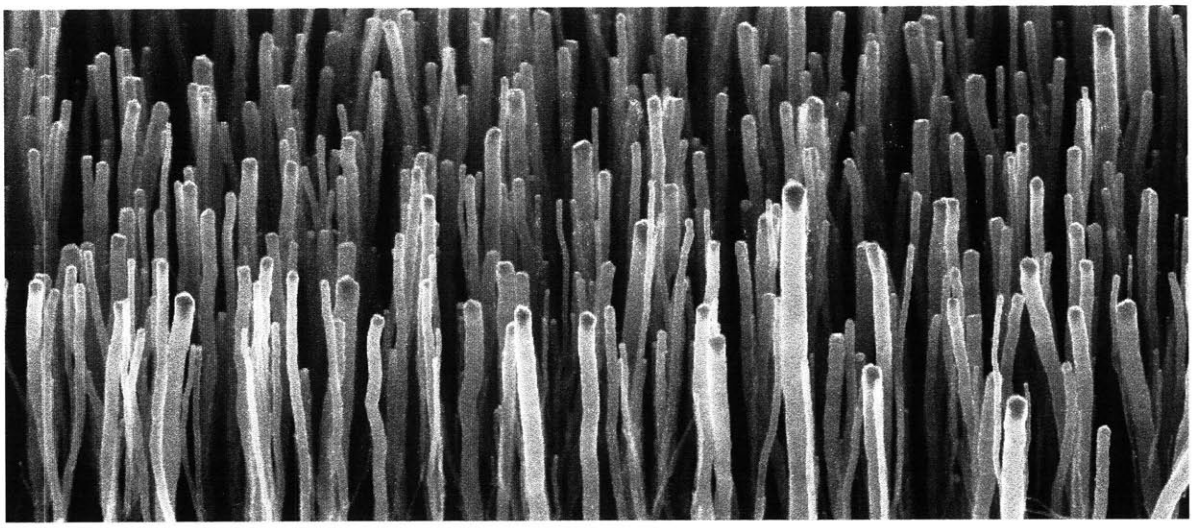

Fig. 4-2: SEM image showing the Ni nanoparticles on the tip at the end of the growth process. The mechanism by which this happens is called tip-growth

Growth Mechanism The most reasonable explanation for the observation that smaller catalyst particles grow smaller nanotubes is the **tip-growth** mechanism whereby the Ni nanoparticles are found on top of the nanotubes (Figure 4-2). It is generally accepted that the first step of the CNT CVD growth process is the decomposition of hydrocarbon molecules on the surfaces of the catalyst particles, followed by carbon diffusion through the catalyst particles and then precipitation at the annular sections of the catalyst surface. In the tip-growth process, the catalyst particles do not adhere firmly to the substrate and can be moved by the growing nanotube [22]. According to one version of this mechanism [21], the

growth process eventually terminates because the catalyst particle gradually becomes covered by amorphous carbon as the growth progresses. As the amorphous carbon encapsulation increases, the effective area of condensation reduces gradually, creating the taper that results in conical carbon nanofiber structures. Growth then stops when the catalyst particle is completely covered by amorphous carbon and carbon can no longer precipitate to form the structured CNTs. Hence, the greater the initial volume and surface area of the nucleated catalyst particle, the longer the actual growth window and the taller the resulting carbon nanofiber! As evidence of their version of the tip-growth mechanism, the authors [21] showed that they were able to grow longer nanotubes by a process of intermittent annealing which presumably de-saturated the catalyst.

4.3 CCNT Characterization

Prior to any device fabrication, we characterized the Plasma-Enhanced Chemical Vapor Deposition (PECVD) tool, referred to as CCNT. Since Ni nanodots are hard to see on a TiN barrier, we chose to use a 50nm SiO_2 film as diffusion barrier. We ran the CCNT several times, varying the growth times and growth temperatures to benchmark growth characteristics.

Scanning electron microscopy (SEM) was used to investigate the effect of various growth conditions on the morphology of carbon nanotubes grown. Figure 4-3 shows the data recorded for forest growths. As shown, the CNTs grow taller at higher temperatures. The growth height is very nearly linear within the range of growth times we used.

Figure 4-4 shows some of the the data recorded for forest growths. Not much consistent data was collected for the growth of isolated CNTs because we were varying the diameters of the Ni nanoparticles in an attempt to determine an appropriate size. Most of the samples plotted in figure 4-4 are of growths processed at 825^oC. The nanoparticles for these growths were of average diameter $200nm$.

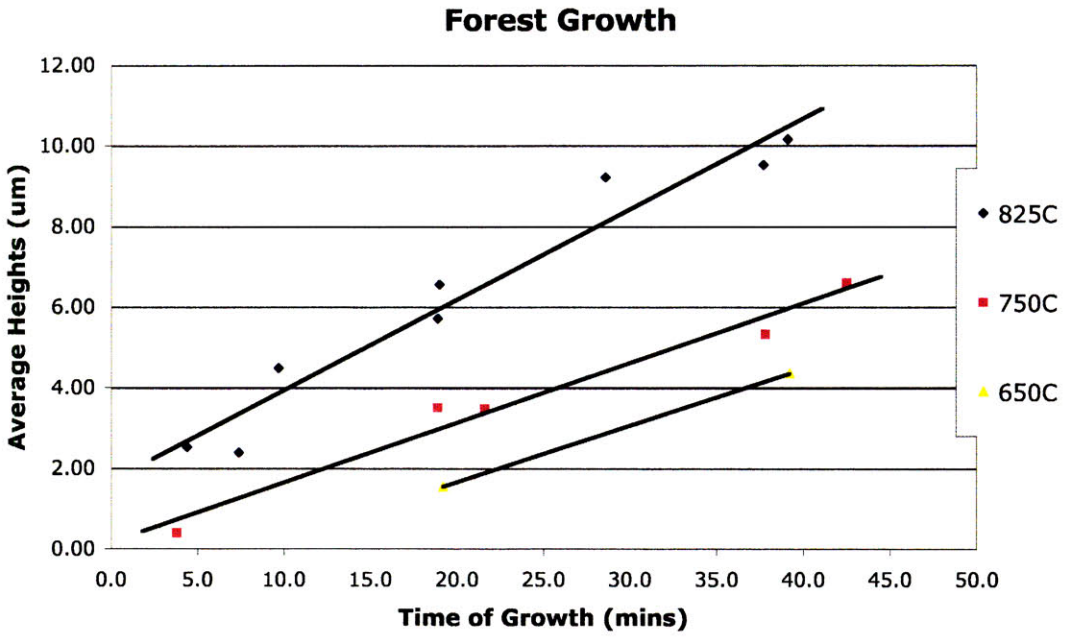

Fig. 4-3: CCNT characterization plot of Average Height vs Growth Time for Forest Growths

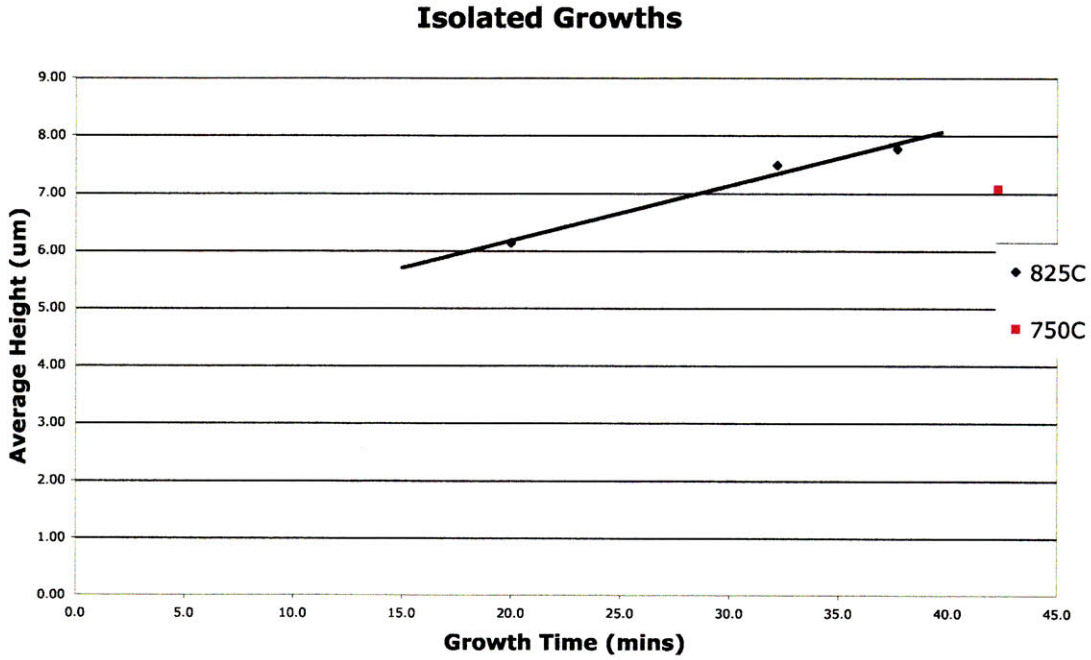

Fig. 4-4: CCNT characterization plot of Average Height vs Growth Time for Isolated Growths

We also ran an experiment in which we grew CNTs on Ni nanodots of different sizes. The results are shown in figure 4-5. These results show that isolated CNTs grow taller when the lithographic dot size are larger and serve as further confirmation of the **tip-growth** mechanism.

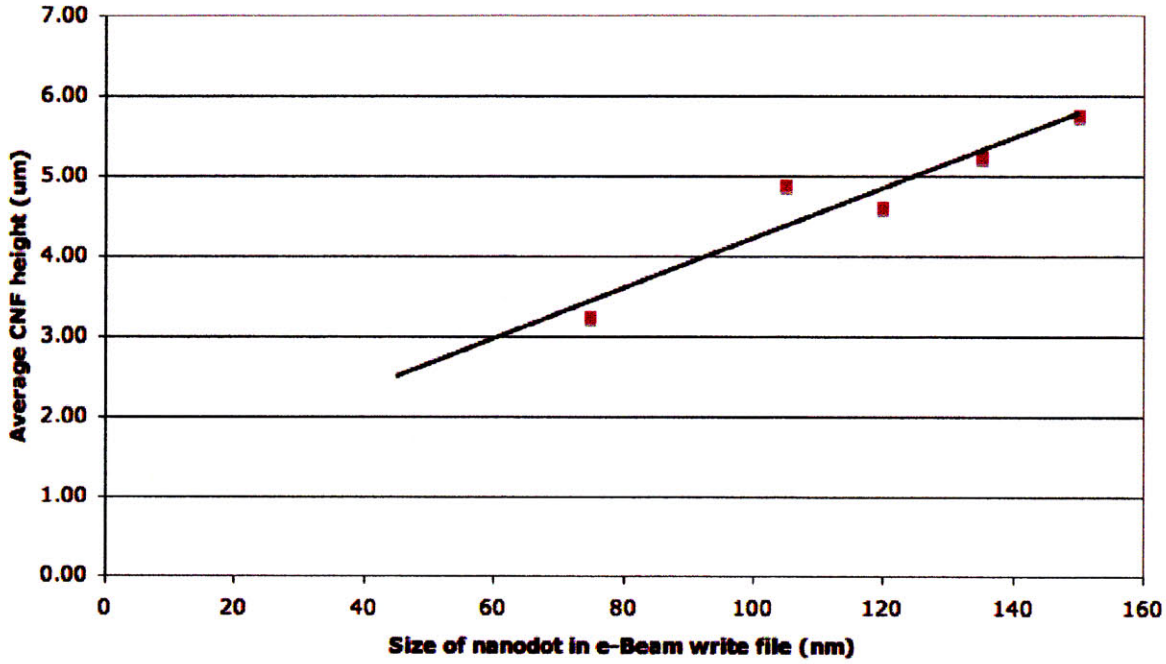

Fig. 4-5: Isolated CNT height as a function of nanodot size

A fuller characterization of the CCNT for isolate growth was further impeded by the difficulty of growing isolated CNTs at lower temperatures. Figure 4-4 shows data for growths at 825^oC only. None of 650^oC and only one of the 750^oC isolate growths yielded any structures recognizable as CNTs under the SEM. It may be that a non-zero anneal time is needed for these lower temperature growths because CNT growth of isolated nanotubes at 700^oC has been previously reported [45].

4.3.1 Height Distribution

The fiber heights for any particular growth, forest or isolated, were found to be uniform within 20% of the mean heights. This was quite a surprise since we expected patterning

to lead to better uniformity. However, we cannot control the effectiveness of the diffusion barrier across the growth area, which might also be related to the temperature differentials in the growth wafers. Figure 4-6 shows a sample growth of isolated nanotubes. Clearly, the uniformity is lacking.

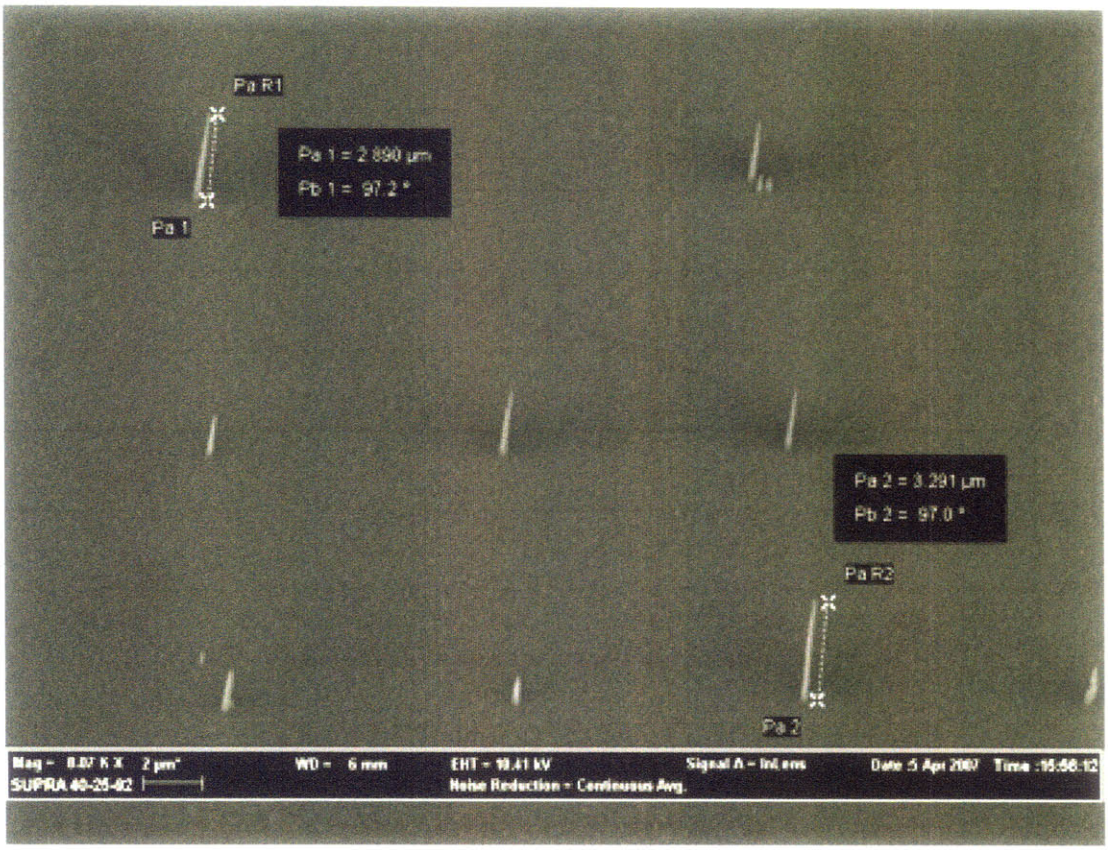

Fig. 4-6: Sample Growth Distribution

4.3.2 Distribution of Tip Radii

Several patterned arrays containing nanodots of differing sizes $(60 - 150nm)$ were fabricated on the same wafer. The wafer was then put through the standard growth process for 25 minutes at 825^oC. There was little observable variation in the tip radii. Figure 4-7 shows two fibers grown from nanodots of different sizes which came out with rather similar radii. The likely problem with this characterization is that the Ni nanoparticles in both growths

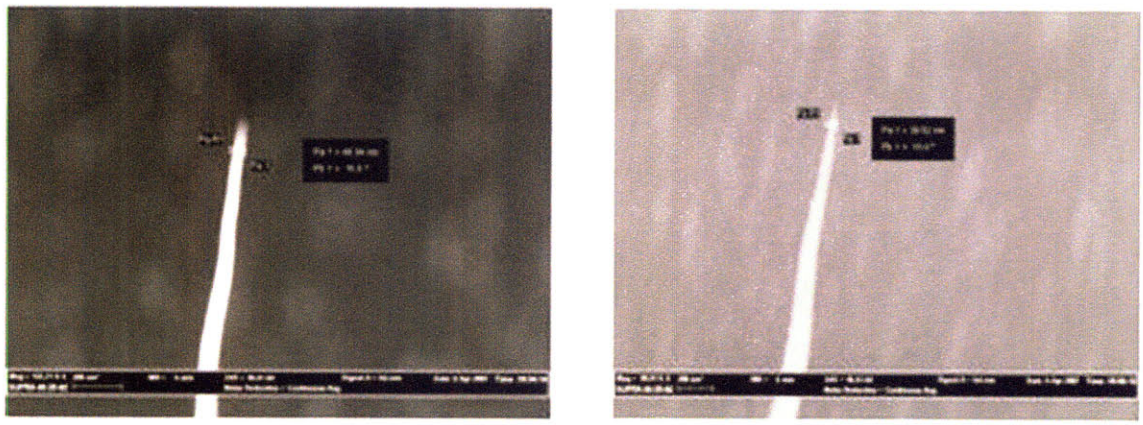

Fig. 4-7: Sample Tip Distribution

were already saturated at the end of the growth, which *is* desirable for our devices since it means we get the smallest possible tip radii. However, this also means that there will not be much difference between the tip radii. To properly characterize the differences in the patterned nanodot sizes, one would have to make sure that the growth does not reach saturation for any of the nanodots. Such effects have been observed with unsaturated forest growths.

Problems with the CCNT The CCNT's plasma generator has not proven to be a good match for the isolated CNT growth process. Forest growths are almost always successful if the plasma ignites at all. However, successful isolated growths have been increasingly hard to come by. Many experiments had to be abandoned because the plasma was faulty.

5 Device Fabrication

5.1 Target Device Structure

As we concluded in chapter 3, we aim to grow CNTs with heights between 6 and 8 μm and as small a radius as is possible. The CNT growth characterization in chapter 4 shows that we can grow isolated nanotubes of the specified range by growing for at least 30 minutes at $825^{o}C$. Our simulations also suggested that we should aim for the smallest gate aperture sizes possible. However, we chose to aim for $1.6\mu m$ in order to provide enough gap between the CNT and the gate and forestall any chances of the tip leaning to touch the gate, hence shorting the device. Since there will be many such elements and it takes only one emitter touching its aperture to short the entire device, this compromise is rather important. However, this also means that the devices we make in section 5.4.1 could potentially have at least $2\times$ larger field factors, as the simulation result in figure 3-8 suggests.

5.2 Before CN Growth

The process starts with the deposition of a $50nm$ TiN layer on top of the unprocessed Si wafer. As mentioned in the previous chapter, TiN serves as a diffusion barrier for the catalyst. A $0.25um$ layer of 950 PMMA is deposited on top of the TiN. Patterning nano dots in the PMMA was done using e-Beam lithography. $8nm$ of Ni catalyst were deposited on the developed PMMA before lift-off.

On e-beam Lithography All e-beam lithography was done at MIT's Scanning Electron-Beam-Lithography facility using either the VS 26 or the Raith 150 tool for direct write e-beam. The Raith is a commercial tool based on a Leo SEM column. It has an acceleration voltage variable from 1-30kV and an approximate beam diameter (for low currents) of 3 nm. The pattern generator can deflect the beam at effective speeds of about 1 MHz and can write field sizes between 50 and 300 microns. The step size on this tool is fixed at 2nm. This tool can write isolated lines as fine as $17nm$ and gratings with a pitch of $70nm$ (i.e. 35 nm lines and 35 nm spaces).

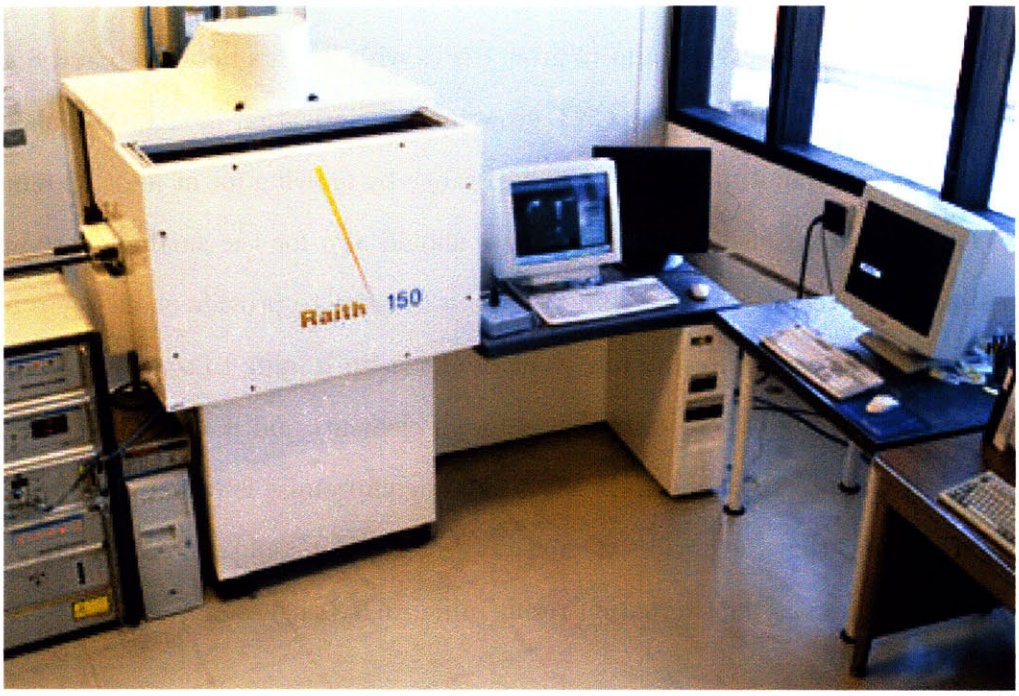

Fig. 5-1: MIT SEBL's Raith tool

PMMA positive resists are based on special grades of polymethyl methacrylate designed to provide high contrast, high resolution for e-beam, deep UV and X-ray lithographic processes. Because of the lithographic resolution supported by both PMMA and the Raith, it is possible to obtain a wide range of dot sizes. However, because nanocluster formation during the growth process is affected by the volumes of the catalyst dots and not merely their areas, the target diameter for the dots was chosen to be $150nm$. K. Teo has shown that

Ni dots of size $300nm \times 300nm \times 7nm$ and below, single carbon nanofibers were produced per dot [47]. Given this and the fact that the maximum over-exposure attempted in our writes on the Raith results in no more than $3\times$ the intended area, refining the lithography to produce sub-100nm dots did nothing to affect the isolated character of the growth. The volume of catalyst does affect the CN height as Figure 5-2 shows. To calibrate the Raith

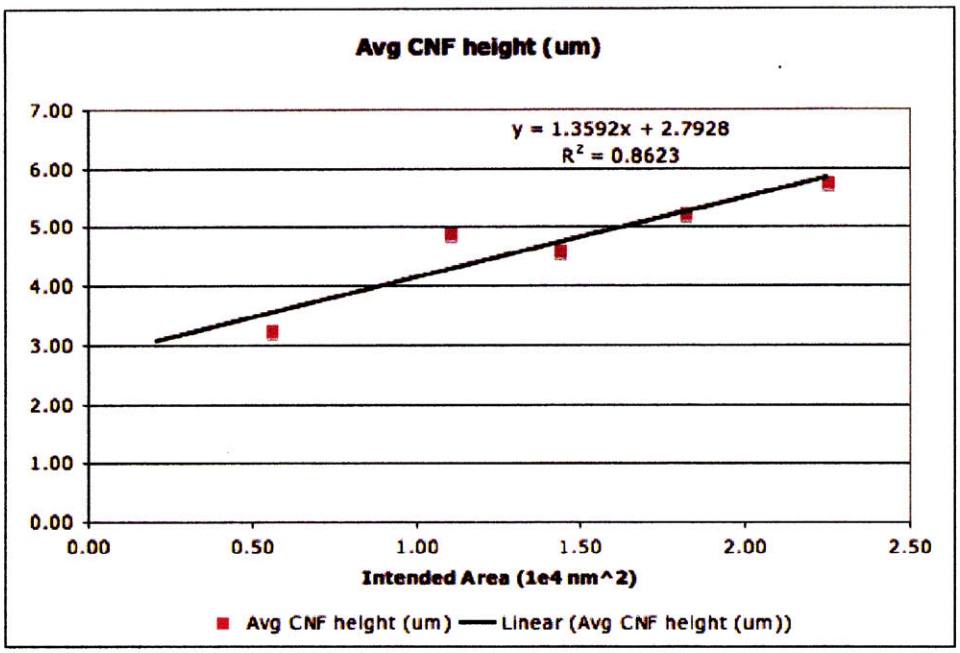

Fig. 5-2: Effect of Nanodot size on CN Height. Dots ranging from $75nm$ to $150nm$ were processed in the CCNT together

for writing 150nm dots, we ran some matrix exposures, varying the dose levels with the same-sized dots. Figure 5-3 shows an SEM of a $200nm \times 150nm$ dot. This dot was the result of a $120nm \times 120nm$ area write. Figure 5-4 shows an example of the calibration process for dot size $200nm$. Figure 5-5 gives an illustration of the write file used.

The actual device array is shown in Figure 5-6. This formation is particularly convenient because it can be used in either of the gating methods described in Section 5.4. The device array contains 36 square sub-arrays, 20 or which are 5×5 grids of nanodots, 12 are 25×25 grids and 4 are 50×50. We aimed for a dot size of $150nm$, that is, in the write file shown, the dots are square areas of size $150nm \times 150nm$. The pitch, that is the nearest-neighbor

Fig. 5-3: SEM image of a $200nm \times 150nm$ dot

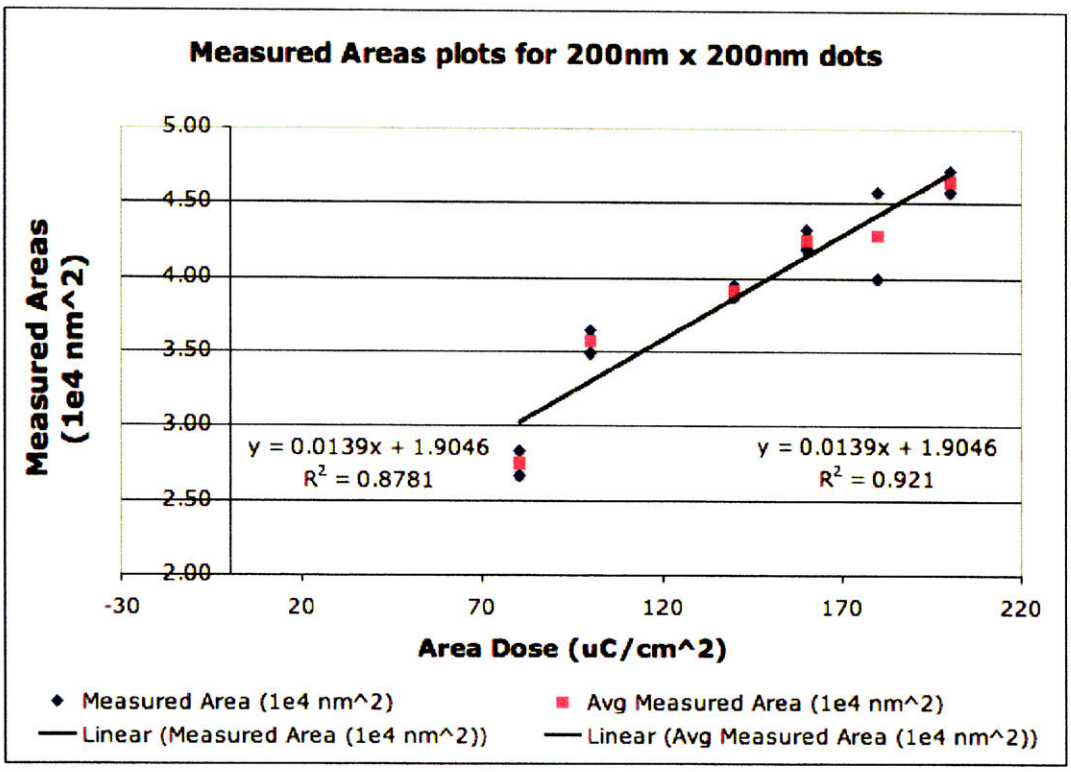

Fig. 5-4: Homing in on appropriate e-beam dose level for $200nm$ dots

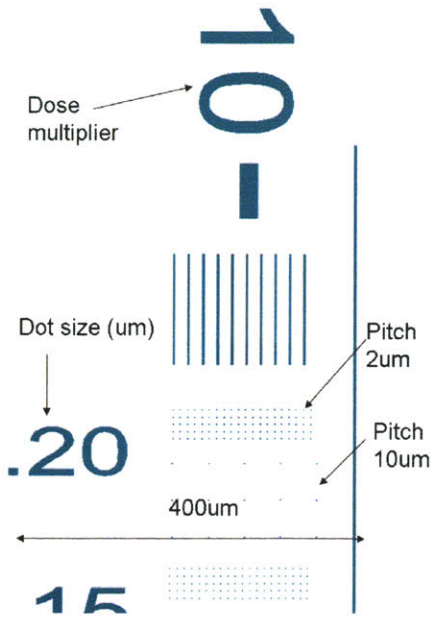

Fig. 5-5: Sample calibration lithography write array

distance in all of the 36 grids was a conservative $30\mu m$. It was almost impossible to take SEM images of more than one grown nanofiber at a time because the pitch was too large. $20\mu m$ would have sufficed.

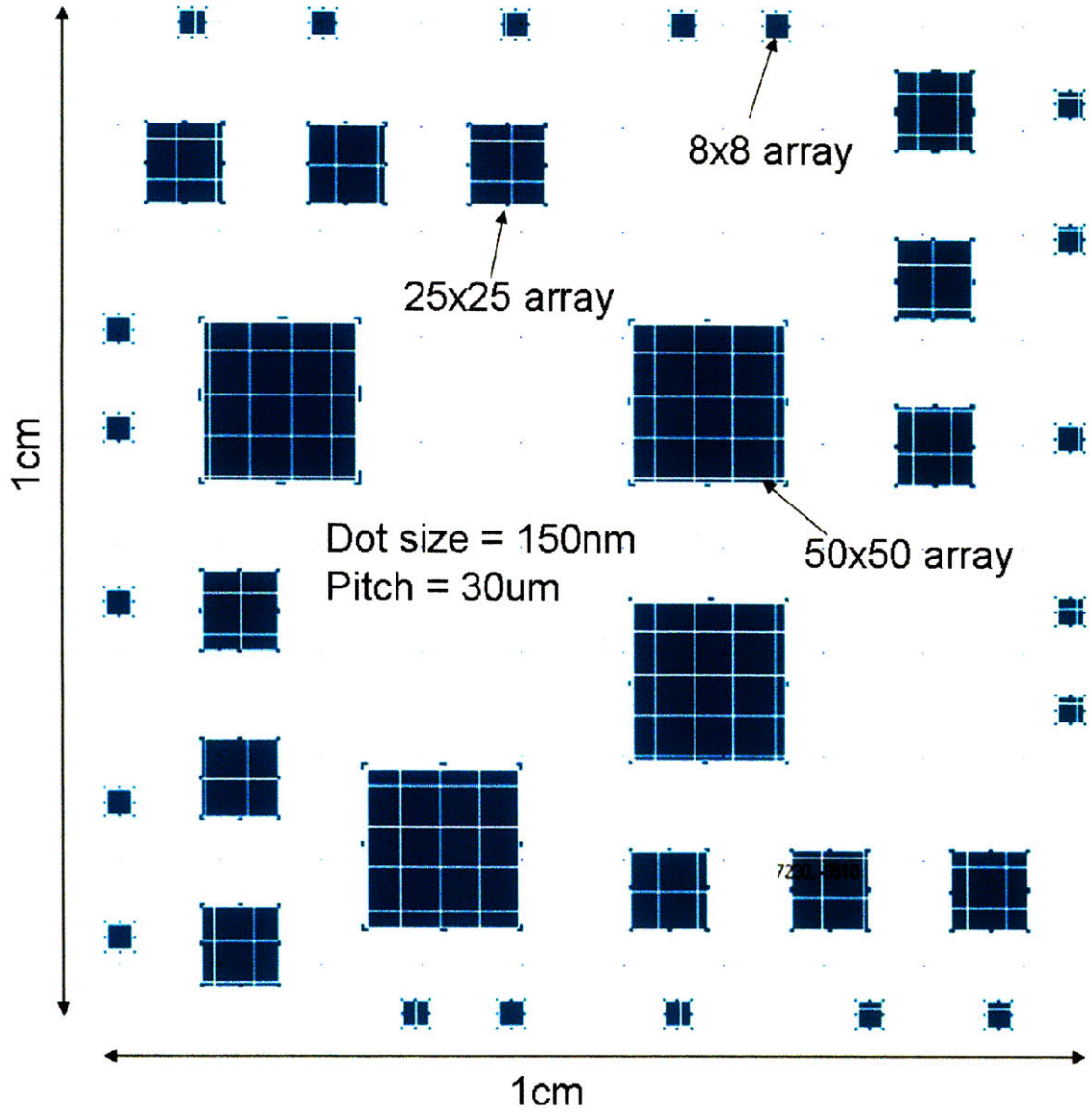

Fig. 5-6: Device nanodot write file

5.3 CN Growth

(see Chapter 4 for a description of the characterization of the CN growth process)
All CNs grown were grown at 825^oC for 40 minutes. The standard growth pressure was 3.5 mTorr but, in practice, the pressure varied between 3.5 mTorr and 6.5 mTorr. Plasma was power-controlled. The voltage was manually held at $580V$, which translated to plasma power levels between 90W and 150W. Sample SEM images are shown in figure 5-7. These images show single CNs because it is rather difficult to image an array of pitch $30\mu m$ on a TiN diffusion barrier. These CNs demonstrate an average tip diameter of $58nm$. The average height is $6.2\mu m$.

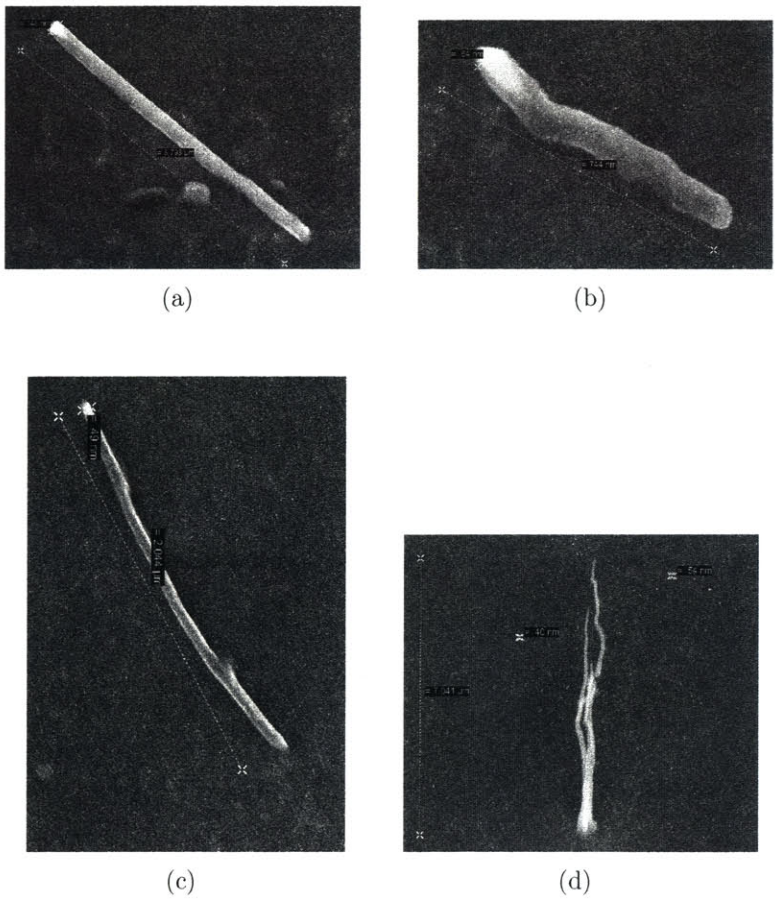

(a) (b)

(c) (d)

Fig. 5-7: Images of Individual Carbon Nanotubes in Test Wafer

5.4 Extraction Gates

To make the complete electrical device, it is necessary to construct a conductive gate in close proximity to the emitting carbon nanofibers. Two methods of fabricating the gate were explored: (1) Self-Aligned Gates and (2) MEMS Suspended Gates.

5.4.1 Self-Aligned Gates

The self-alignment method was developed in conjunction with Drs. Luis Velasquez-Garcia and Liang Yu-Chen. It starts with the deposition of a thin layer of oxide to insulate the CN tip from the gate material. The thickness of the deposited oxide was chosen to be in a range that minimizes the operating voltage of the device (higher field amplification with smaller separation) and also prevents breakdown of the insulating oxide. Thin silicon oxide is known to permit electrical discharges when $0.7 - 1kV/\mu m$ is applied.

Doped amorphous silicon was deposited as gate material over the oxide. Amor-Si is conductive and simulation predicted that the field amplification at the tip is not very sensitive to the thickness of the gate. Therefore, we did not try to grow very thick amor-Si in order to maximize the field amplification. The danger with growing thick amor-Si is that thick amor-Si would be more likely to fall under its own weight. On the other hand, it is also stiffer and less likely to break on external impact. Typical thickness obtained in fabrication ranged between $0.2\mu m$ and $0.4\mu m$. These values refer to the width of the amor-Si sheath surrounding the CNF (see Figure 5-8).

The steps used to open up the gate aperture are listed below:

1. Enough positive photoresist is spun so as to almost cover the tips of the vertical amor-Si-coated structures.

2. A short dry-etch process (with oxygen plasma) is applied to make sure that the amor-Si at the tips is exposed and not covered by the PR

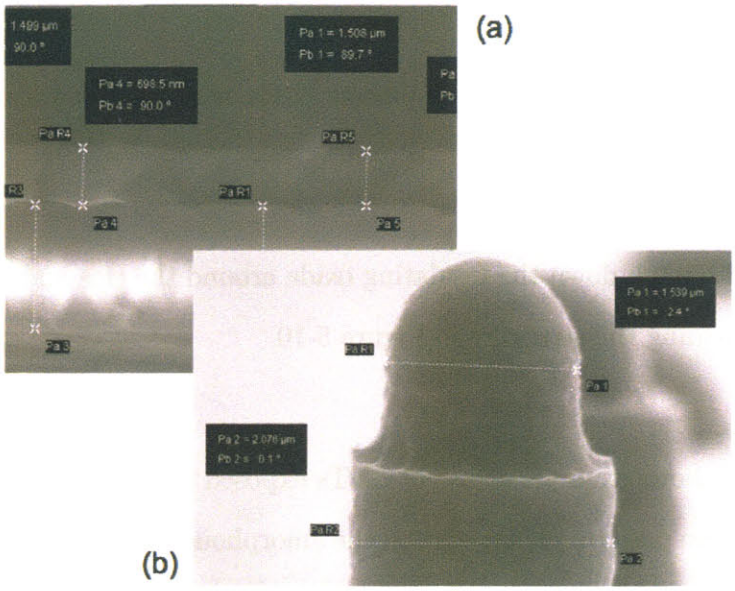

Fig. 5-8: Typical image of the gate mid development process

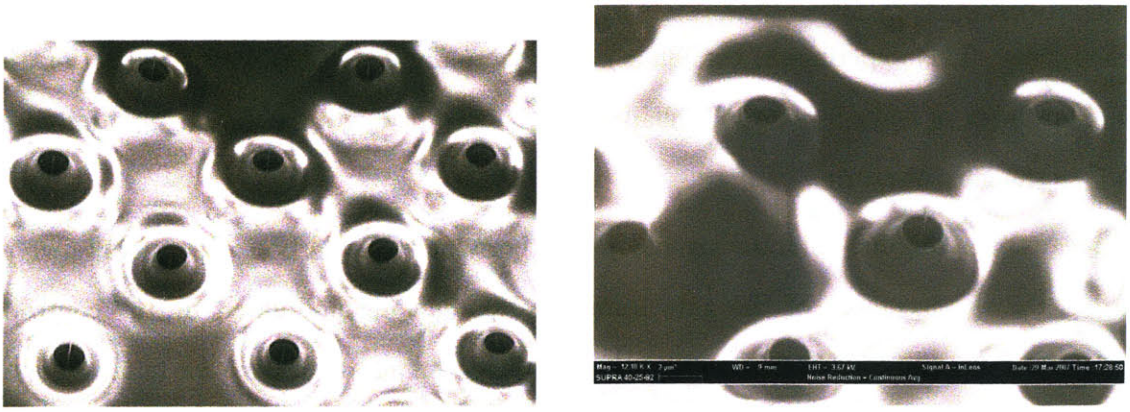

(a) (b)

Fig. 5-9: Array of CNTs after BOE

3. Another short dry-etch (with Sulfur Hexafluoride plasma) exposes the oxide at the tips (Figure 5-8(b))

4. A low pressure, low power oxygen plasma clean removes the resist while the oxide remains

5. BOE is used to etch down the insulating oxide around the tips and expose the carbon nanofiber, yielding the structure in Figure 5-10

Also, figure 5-9 shows example arrays of CNTs exposed after the BOE oxide etch. These latter arrays still have positive photoresist on the amorphous silicon, that is, we skipped step (4) above for these samples.

Timing is of utmost importance in many of the steps required in the self-alignment process. Figure 5-11 shows a failed process run. The last step, step (5) in which we etch back the insulating oxide with BOE, was prolonged. The result was that much of the oxide was etched away, leaving only the carbon nanotubes and the hanging amorphous Si gate material as shown in Figure 5-11. The gate is left hanging because not all the oxide was etched away. This experiment, though a failure, actually gives us a strong indication that a $0.25\mu m$ layer of amor-Si will not collapse under its own weight when hanging around the CNT as the gate aperture.

Because the original columns are not perfectly cylindrical (carbon nanofibers taper upwards), the displacement of the gate from the tips can be modulated by the controlled etching of the amor-Si. The same technique is however more effective for controlling the relative heights of the tip and gate. Tip-gate distances are better controlled by the thickness of the deposited oxide.

Interestingly enough, this self-alignment can also be applied to forests of CNTs as indicated by the half-complete self-aligned gate structures of figure 5-12.

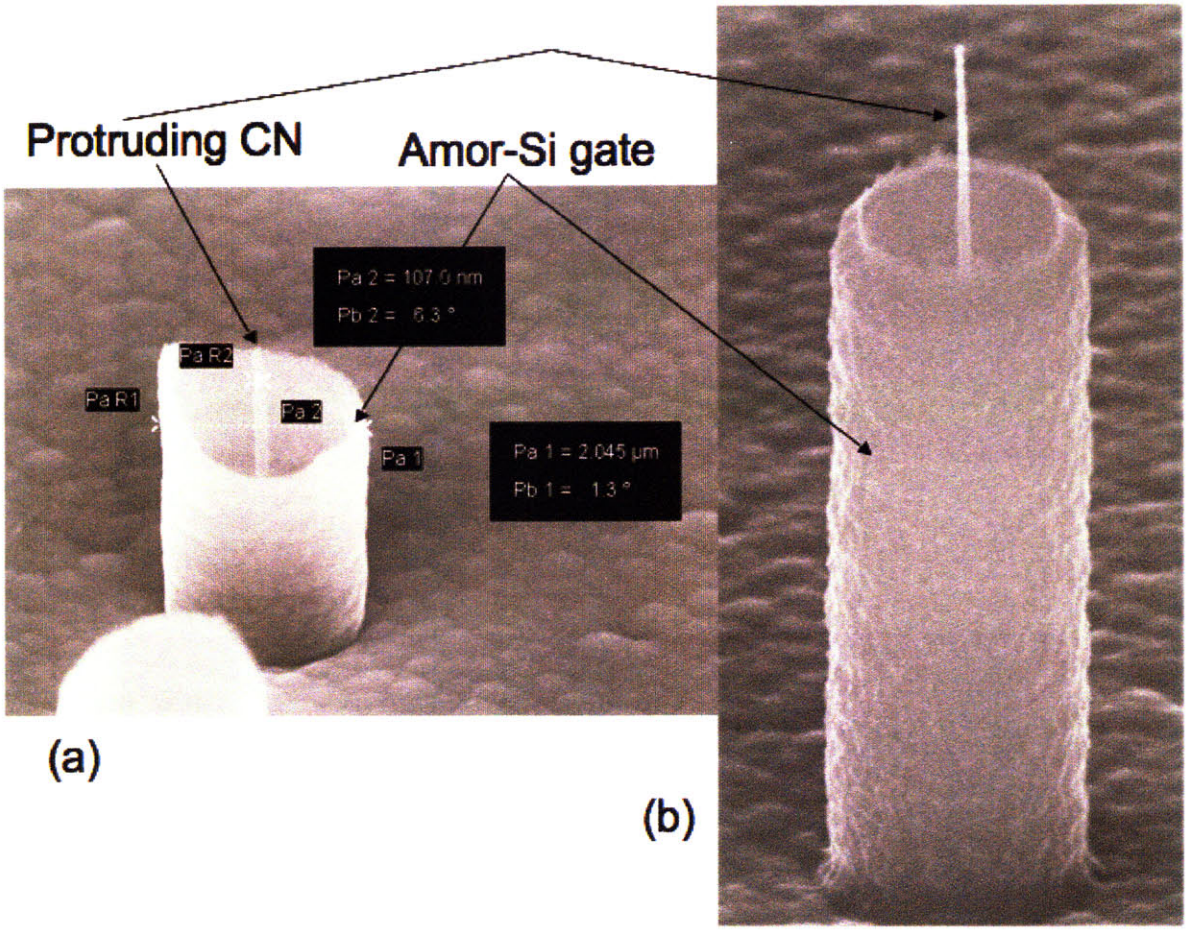

Fig. 5-10: Two examples of the complete device. Notice that the CNs protrude significantly above the top of the self-aligned gate. Ideally, we want the tip to be very slightly above the gate as varying the gate height during simulations showed us (Figure 3-9)

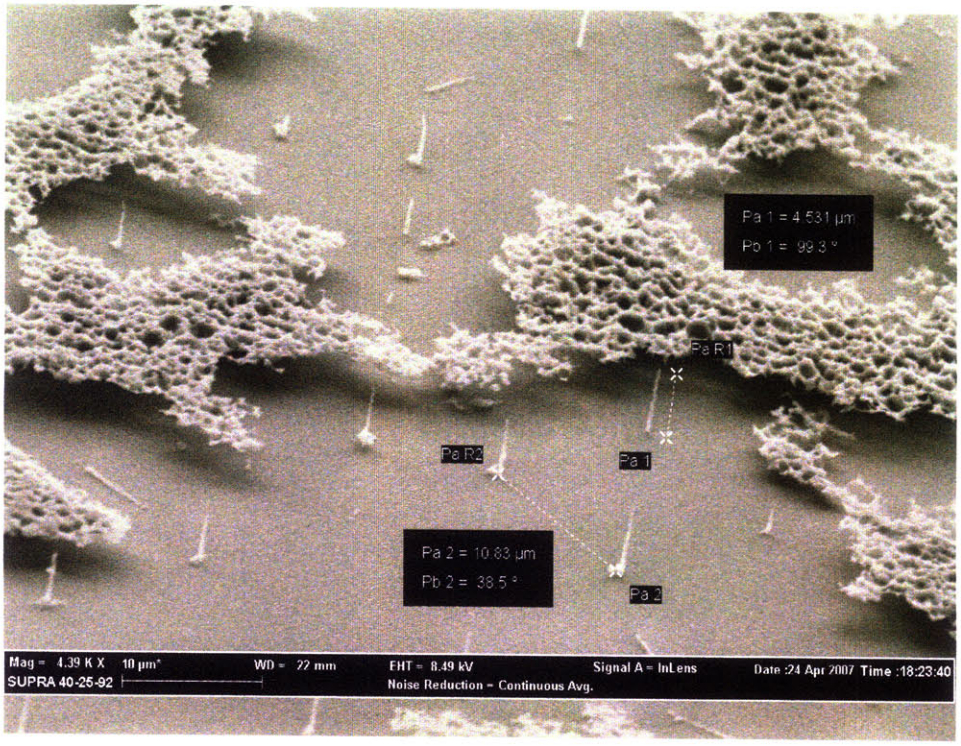

Fig. 5-11: SEM image of a failed process run

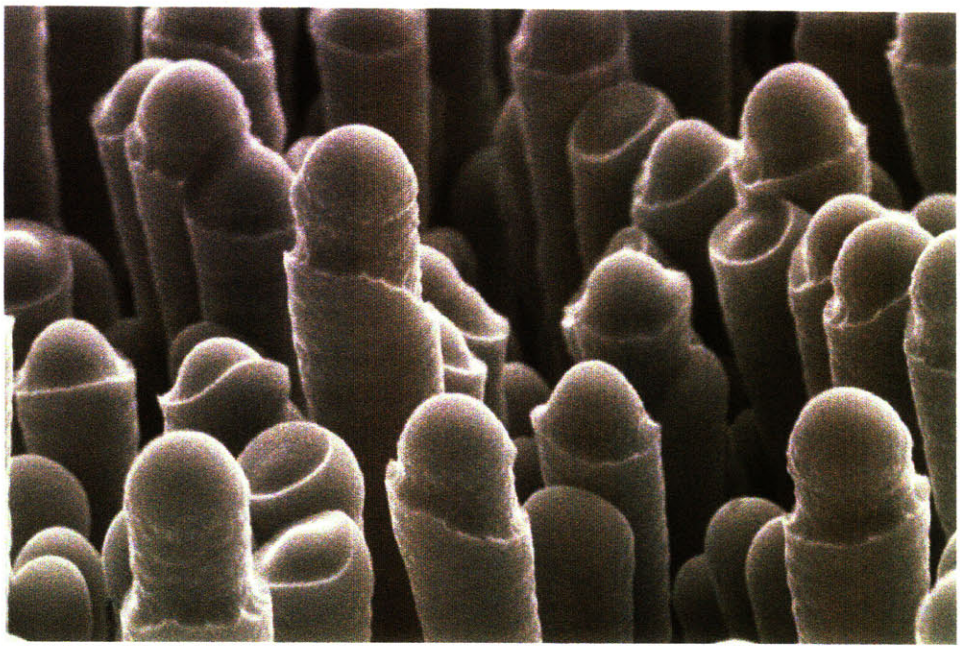

Fig. 5-12: Half-Complete Self-Aligned Forest

5.4.2 MEMS Suspended Gates

The original idea for the mechanical suspension rig came from Luis Velasquez-Garcia.

A $2cm$ x $2cm$ Si wafer was etched through at several locations, forming a screen of holes. It was then coated with metal on both sides. This served as the gate; it has $< 20\%$ transparency. The piece is placed over fully grown CNs, suspended by a plastic arbor shim that serves as an insulating barrier. Much of this process requires careful assembly. It is very easy to use a shim that is too thin, leading the device to short. Figure 5-13 shows an aerial view of an assembled MEMS suspended gate. The Si substrate on which the CNs were grown is under the gate as labeled. There are also 2 spring-loaded rods which help to keep the device stable while it is being loaded into the probe station as described in chapter 6.

The advantage of this approach to gating is that it is very simple and requires comparatively little time to complete. However, we would expect a device constructed this way to have a higher turn-on voltage than one constructed using the self-alignment micro-process (section 5.4.1).

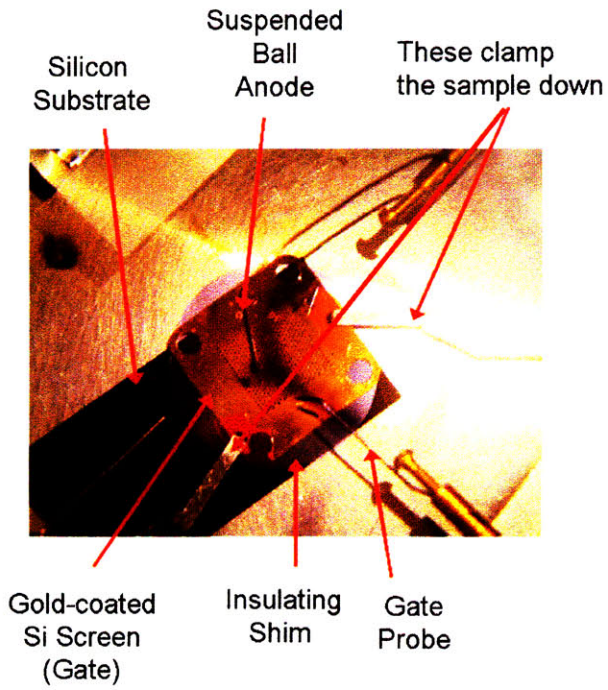

Fig. 5-13: MEMS Suspended Gate

6 Device Characterization

A device formed using the macromechanical suspension process above was tested. An insulating shim of dimension $0.004'' \times 0.625'' \times 1''$ was placed around the CN array and then overlaid with the perforated Gold-coated wafer. This meant that the device gate was at most $100\mu m (= 0.004'')$ from the base of the emitting CNTs, at which height there was practically no danger of the gate sagging and shorting the CNTs. The gate-CNT separation is *too* large (which is why the conformal microprocessing was tried first); we do not get the required currents from this device. In fact, in the absence of the CNTs and any other sources of field amplification, we can only obtain an inadequate field of $10^5 V/cm$ with 1000V across parallel conducting plates separated by $100\mu m$. The field amplification effect of the CNTs raises this field factor from $100cm^{-1}$ to greater than $10^5 cm^{-1}$, even at the non-proximal location of the gate.

6.1 Testing

Figure 6-1 shows the actual test station while Figure 6-2 shows a schematic of the testing setup. The gold-coated gate is probed using a very sharp tungsten probe. There is a microscope above the test chamber that helps in positioning the tungsten probe to just touch the gate. For field emission tests, the ball collector or anode was biased at a high voltage of $1100V$, the gate voltage was swept across increasing ranges and the wafer, whose backside is in contact with the metal sample holder, was held at ground. For field ionization tests, the anode was biased at a voltage between $-800V$ and $-1100V$, the gate was held at

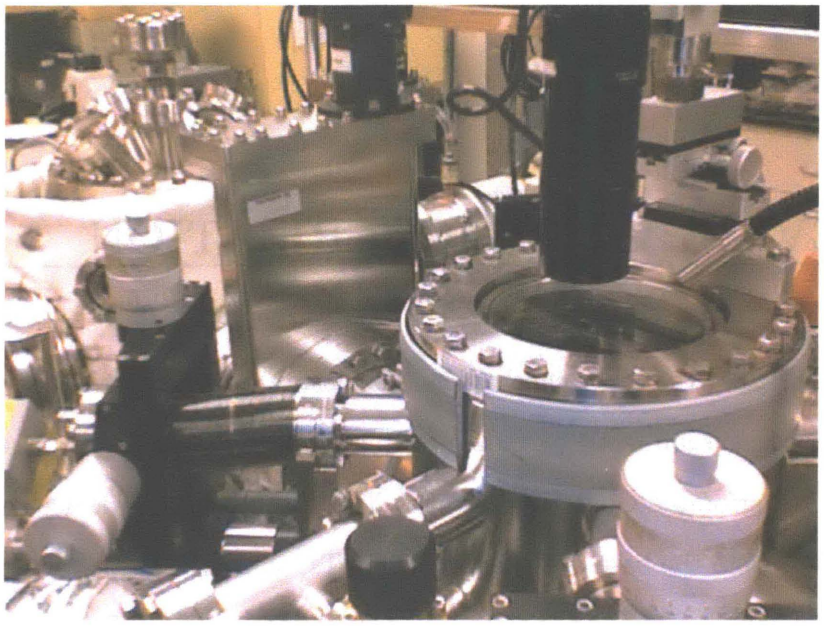

Fig. 6-1: The picture of the Ultra-high Vacuum Characterization Station shows the main test chamber on the right and the loadlock on the left. The station boasts a roughing pump, a turbo pump and a ion pump, which work together to achieve vacuum in excess of $10^{-8} mTorr$

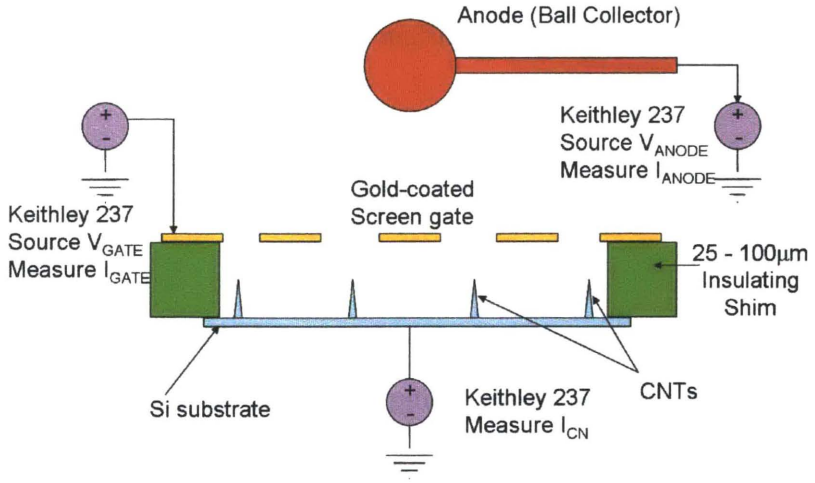

Fig. 6-2: This schematic of the testing set-up shows the ball which is platinum-coated and usually fixed at about $1cm$ above the substrate. Like the gate probe (also shown), the ball can be moved around in the three cardinal directions by manipulators located just outside the main testing chamber

ground and the wafer voltage was swept.

The testing procedure starts with a check for good electrical contact. We make sure that the gate probe is actually touching the probe and that the device is not shorted. Then we do an initial manual sweep of the gate voltage up to a voltage as would not threaten the probe station's compliance limits. Once we determined a safe ramp voltage, we acquire field emission data using Labview. This field emission data will allows us to determine the average field amplification factor of the emitting devices. This value will give us an idea whether or not field ionization is possible with the device. Recall that field ionization requires at least 1 order of magnitude more field than field emission to occur. Once we are ready to test for field ionization, we change the electrical configuration of the test to the field ionization configuration. We perform a baseline field ionization run without passing any gases to determine what currents (if any) are obtained in the absence of gases. Then we pass in Argon, taking care to set the pressure first. After the field ionization tests, we also run a final field emission test to see if the field amplification has increased or decreased. Usually, we would find that the field factors increase over the course of a test run.

All electrical measurements and sourcing was done with *Keithley 237* High Voltage Source Measurement Units. The data was acquired using the popular software *Labview*, a National Instruments product. *Labview* used a GPIB cable and card to communicate with the probe station.

6.2 Data analysis

6.2.1 Field Emission Characteristics

Figure 6-3 shows the typical I-V characteristics of a field emission test and Figures 6-4 and 6-5 show the Fowler-Nordheim plots for the field emission tests ran before and after the field ionization experiments. It is clear that the data agrees very well with the Fowler-Nordheim

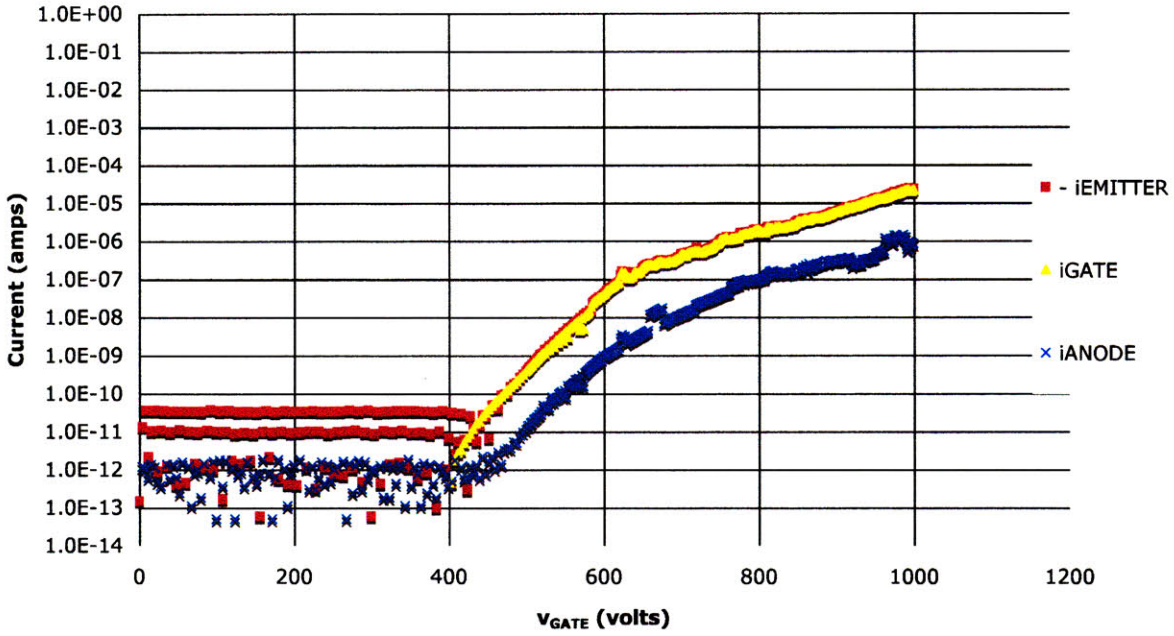

Fig. 6-3: Typical I-V curves of a Field Emitter Array. The anode current, emitter current and gate current are all plotted on a logarithmic scale with respect to the gate voltage. This device showed a turn-on voltage of about $500V$

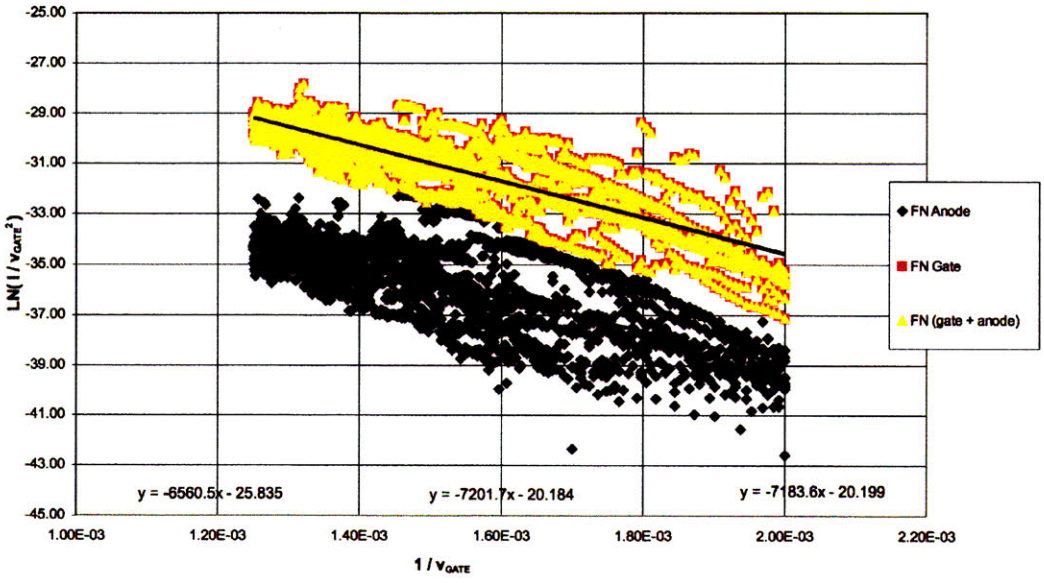

Fig. 6-4: Typical Fowler-Nordheim plot of "Before" Field Emission data showing fits of the Fowler-Nordheim equation to the anode and gate currents. It also shows a fit of the equation to the sum of anode and gate currents. These plots help to determine the field factors β relevant to the specific experiment. The near-equal slopes of the three fits increase our confidence in the measured β

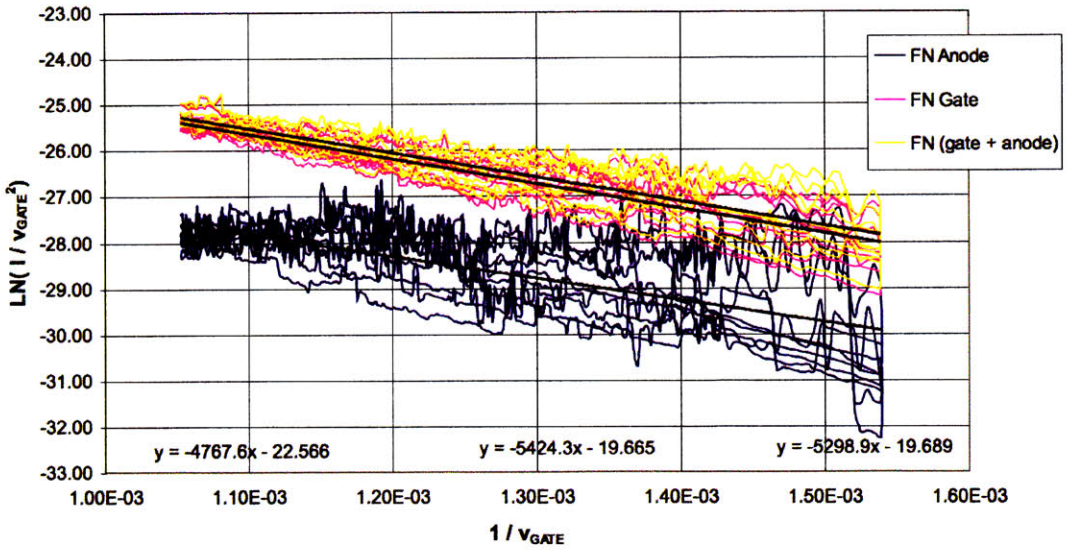

Fig. 6-5: Typical Fowler-Nordheim plot of "After" Field Emission data showing fits of the Fowler-Nordheim equation to the anode and gate currents. It also shows a fit of the equation to the sum of anode and gate currents. These plots help to determine the field factors β relevant to the specific experiment. The near-equal slopes of the three fits increase our confidence in the measured β

theory. Recall the Fowler-Nordheim equation 2.1:

$$I = a_{FN} V^2 e^{\frac{-b_{FN}}{V}} \tag{6.1}$$

where

$$\begin{aligned} a_{FN} &= \frac{\alpha A \beta^2}{1.1\varphi} e^{\frac{B(1.44\times10^{-7}}{\varphi^{0.5}}} \\ b_{FN} &= \frac{0.95 B \varphi^{3/2}}{\beta} \\ A &= 1.54 \times 10^{-6} \\ B &= 6.87 \times 10^{7} \end{aligned}$$

α is the effective emitter area, φ is the workfunction (assumed to be $4.8eV$ for graphite), and β is the field factor.

Transforming equation 6.1, we get $\ln(\frac{I}{V^2}) = \ln(a_{FN}) - \frac{b_{FN}}{V}$. Therefore, in Figures 6-4 and 6-5, we have plotted $\ln(\frac{I}{V^2})$ against $\frac{1}{V}$ in the voltage range from the turn-on ($500V$) to the terminal voltage ($800V$). Fowler-Nordheim predicts such a plot should have a good fit with a linear plot of slope $-b_{FN}$, from which we can deduce β. Using the formula for b_{FN} and the slopes from the Fowler-Nordheim plots, we were able to estimate that, for the device being analyzed:

Table 6.1: Field Factors Derived from "Before" Field Emission Data

Field Factor using:	b_N	β $[cm^{-1}]$	r $[nm]$
Anode Current	6560.5	$\mathbf{1.09 \times 10^5}$	91.7
Gate Current	7201.7	$\mathbf{9.93 \times 10^4}$	101
Gate + Anode Current	7183.6	$\mathbf{9.95 \times 10^4}$	100
(average)	6981.9	$\mathbf{1.02 \times 10^5}$	97.6

Table 6.2: Field Factors Derived from "After" Field Emission Data

Field Factor using:	b_N	β $[cm^{-1}]$	r $[nm]$
Anode Current	4767.6	$\mathbf{1.50 \times 10^5}$	66.7
Gate Current	5424.3	$\mathbf{1.32 \times 10^5}$	75.9
Gate + Anode Current	5298.9	$\mathbf{1.35 \times 10^5}$	74.1
(average)	5163.6	$\mathbf{1.38 \times 10^5}$	72.2

These field factors are an order of magnitude larger than the field factor of 10^4 $/cm$ obtained by Riley et al [20]. Riley et al used densely packed, multiwalled CNTs growing perpendicular to a stainless steel wire in their experiment. We get higher field amplification because the isolation of the CNTs in our experiment prevents field shielding [48, 23]. When the intertube distance is less than about twice the height of the CNTs, the induced charges at neighbouring tips can strongly repel each other, thus reducing the charge density at the tips and lowering the local electric field strength.

The field factors recorded in tables 6.1 and 6.2 give us the following bound for the

operating β:

$$\mathbf{1.02 \times 10^5} < \beta < \mathbf{1.38 \times 10^5} \ /cm$$

These tables also show estimates of the tip radii using the conservative "ball in a sphere" model: $\beta = \frac{1}{r}$. The calculated radii do *not* show excellent correlation with the SEM sampling we took. In that sampling, the CNs had an average *diameter* of $58nm$ (see section 5.3), whereas the "ball in a sphere" model predicts that the *radii* were of the order of $100nm$. We also note that the field factors increased after the field ionization experiments. This might be due to changing work functions as the CNs are conditioned by the applied positive voltages.

6.2.2 Field Ionization Characteristics

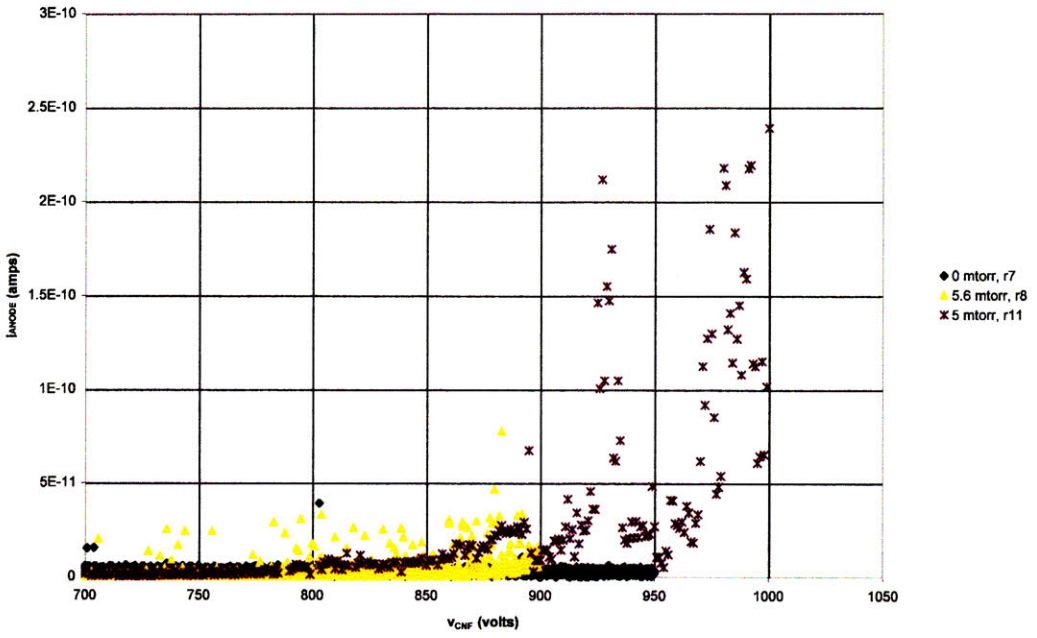

Fig. 6-6: Each sweep was run at a different pressure. The "0" $mTorr$ run is really the base pressure during the runs, which was about 1×10^{-7} $mTorr$. Since the anode currents recorded at base pressure were much smaller compared to the currents recorded at higher pressures, we conclude that our field ionization data is not just background noise

Figure 6-6 shows the anode currents recorded at base pressure and at two other pressures. The voltage sweeps at base pressure were used to measure the background noise. As the

figure shows, we have significantly higher currents at pressures higher than the base pressure, especially at 5 $mTorr$. Therefore, we can conclude that we are actually recording ion currents at the higher pressures. The correlation between the anode and gate currents is an indication that some fractions of the currents being recorded were being generated by the same process, likely field emission. This implies that we may have had some Electron Impact Ionization due to field emission from the gate (which was at the lowest potential). However, the R^2 values associated with the linear fits on the Anode vs Gate Current plot (Figure 6-7) suggest that the correlation between the anode current and gate current is not very strong. This is a good indication that there was some field ionization too. Since we cannot definitively differentiate the two processes, we will take the conservative stance and conclude that both processes contributed to the anode currents in some undefinable ratio.

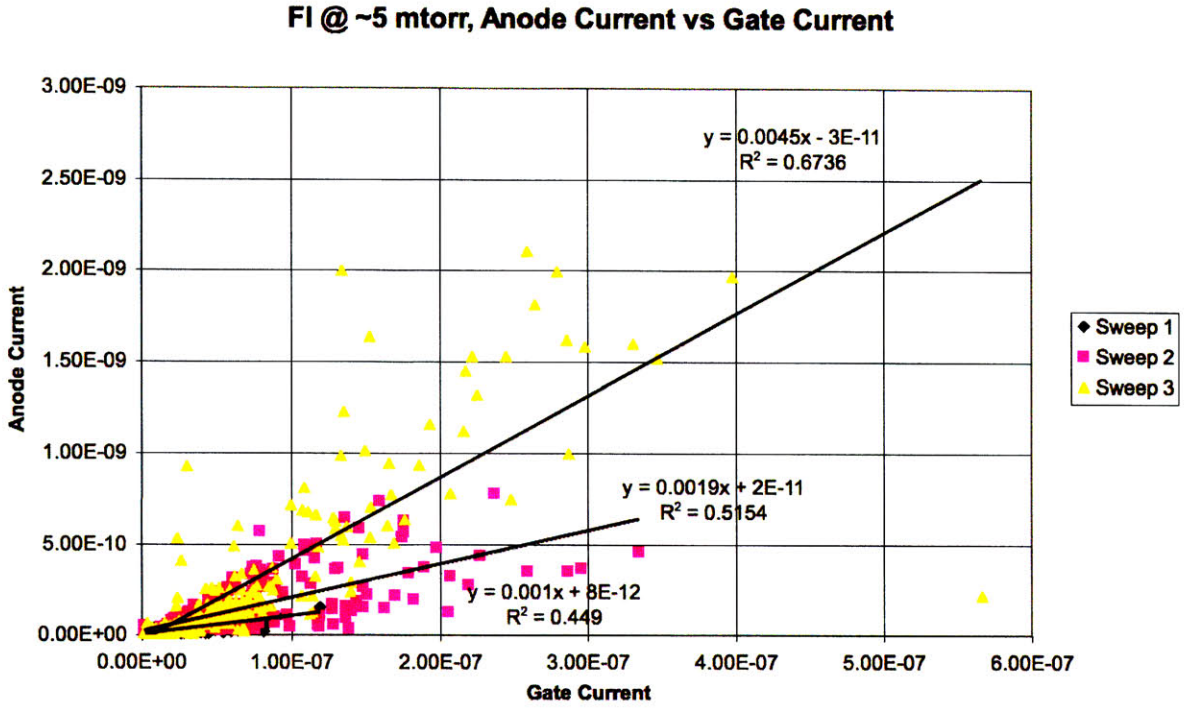

Fig. 6-7: Anode vs. Gate Currents for Consecutive Voltage Sweeps: possible indication of rising local pressures

The field ionization data showed significantly more noise than the field emission data. Figure 6-7 shows the ratio of anode current and the gate current for 3 consecutive voltage

sweeps at a pressure of 5 $mTorr$. As the figure suggests, the field ionization characteristics seemed to change as time progressed. Normally, one would expect the currents to increase as the suspension shim flattens out from sustained heating at the extremes of the voltage sweeps. However, the currents we got were not high so there should not have been any heating issue. Moreover, the anode current increased significantly more than the gate current. Interestingly enough, this effect might be simply explained by the (slowly) rising pressure in the probe station. However, as we do not have reliable measurements of the local pressures, it is difficult to suggest / investigate a more rigorous explanation for the pressure rise. We also observed that the pressure rise was more significant towards the high extreme of the voltage sweep, which effect might be explained by out-gassing from the shim.

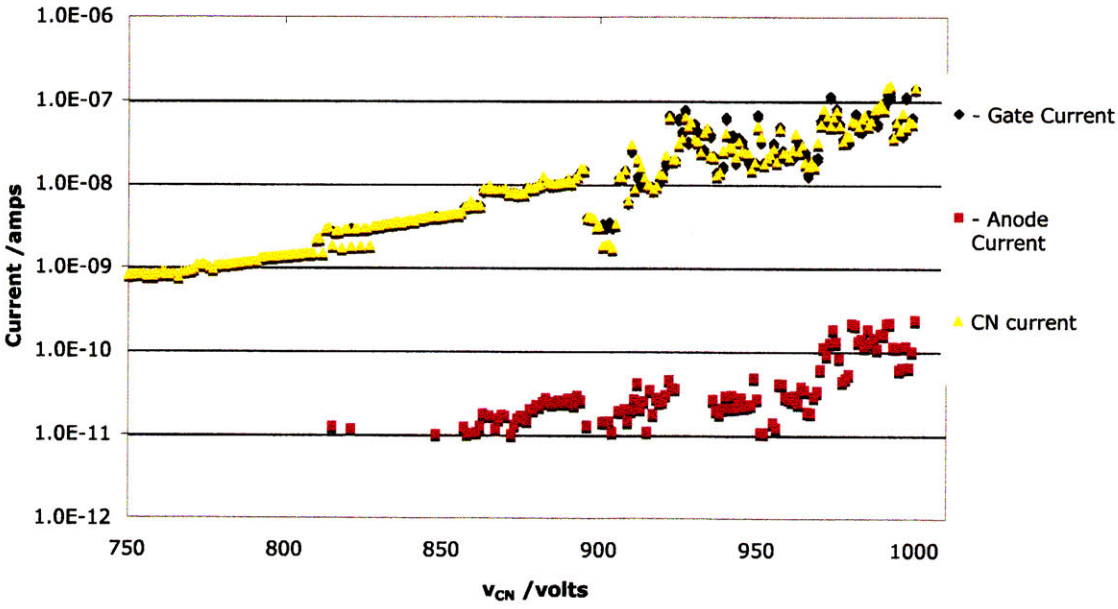

Fig. 6-8: Typical I-V curves of a Field Ionization Array showing a turn-on voltage of about 900 V. The anode current, emitter (CN) current and gate current are all plotted on a logarithmic scale with respect to the emitter voltage

To prevent significant pollution of the data, we analyzed the sweeps separately. Figure 6-8 shows the I-V characteristics of our final sweep at 5 $mTorr$ (there was too much noise in

the other sweeps). The striking detail in this plot is the exponential nature of the currents. We note that this should remind us of the field ionization equations we derived for the low-field scenario in chapter 2. The apex of the voltage sweep here is $1000V$. Considering the bound for β that we deduced in section 6.2.1, $1000V$ amounts to a field half as great as the $2 \times 10^8 V/cm$ that Gomer suggests is the typical field required for field ionization [6]. This suggests that we should analyze the field ionization data in the low field regime as we did in section 2.3.

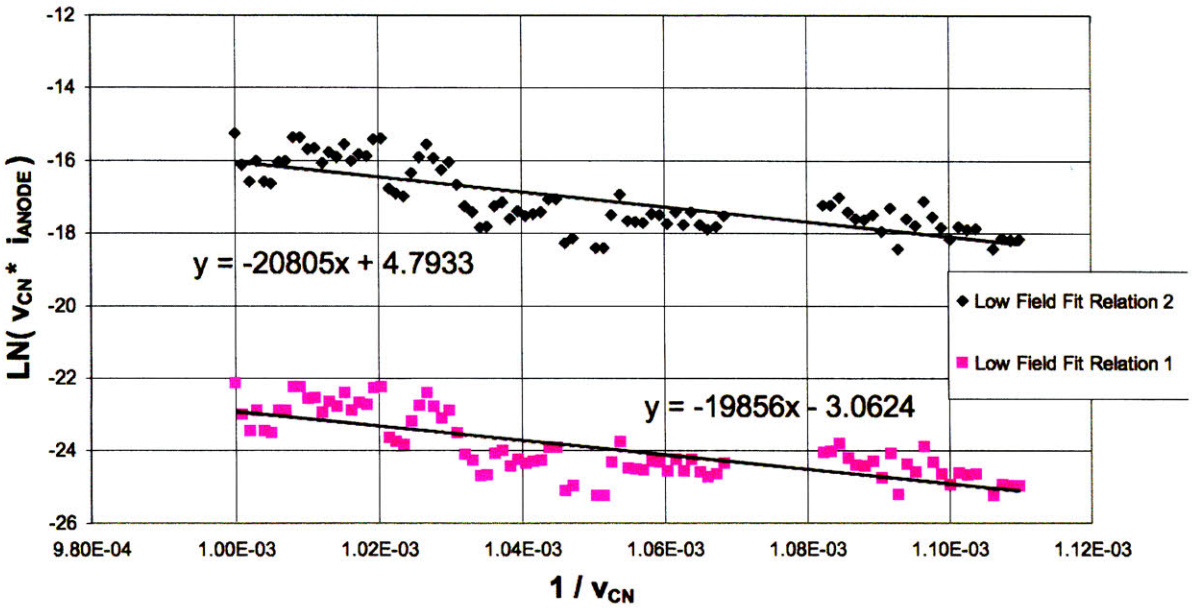

Fig. 6-9: Low Field Fit to Collected Data
"Low Field Fit Relation 1" is the fit to $i \propto exp\left(-\frac{1}{F_0}\right)$ while "Low Field Fit Relation 2" is the fit to $i \propto \frac{1}{F_0} exp\left(-\frac{1}{F_0}\right)$

Data Fit We obtained excellent fits with the Low Field Equation 2.11 using only the exponential and critical distance terms. That is, we fitted the data to the relations

$$i \propto \frac{1}{F_0} exp\left(-\frac{1}{F_0}\right)$$

and

$$i \propto exp\left(-\frac{1}{F_0}\right)$$

Figure 6-9 shows both fits. The first fit, "Low Field Fit Relation 1," is a linear fit to the plot of $\ln(i_{ANODE})$ against $\frac{1}{v_{CN}}$. v_{CN} is the voltage applied to the emitter or carbon nanotube. The second fit, "Low Field Fit Relation 2," is a linear fit to the plot of $\ln(v_{CN} * i_{ANODE})$ against $\frac{1}{v_{CN}}$.

As in section 2.3, both of these fits demonstrate very similar slopes (one is -20805, the other is -19856). Recall from section 2.3 that the proportionality constant for both fits is

$$\frac{C_3}{\beta}$$

where $C_3 = 6.8 \times 10^7 I^{\frac{3}{2}}$ and we ignore the multiplicative factor $\varepsilon(F_0)$ which is practically 1 in the range $(9.09 \times 10^7 < F_0 < 1.39 \times 10^8\ V/cm)$ of the fields generated in our experiment.

As an accuracy check, we deduce

$$9.81 < I_{\text{Argon}} < 12.61$$

from the equation for C_3, our deduced range for β (section 6.2.1) and the slopes of the fits. This value is quite accurate ($I_{Argon} = 15.7596$).

6.3 Conclusion

We managed to demonstrate field ionization from an array of carbon nanotubes. The field amplification factors of our CNTs yield fields of $10^8\ V/cm$ at $1000V$, which field is in the low range for field ionization. Therefore, the field ionization currents generated are not very high ($1nA$). They are probably even lower because we could not eliminate Electron Impact Ionization. It is quite likely that the currents recorded were generated from both electron impact ionization and field ionization. Nevertheless, the data agreed very well with the Low

Field equations and we were able to deduce the ionization potential of Argon to within 20%.

7 Thesis Summary and Suggestions for Future Work

7.1 Thesis Summary

We used a single-gated field ionization array (FIA) made up of vertical, isolated multi-walled carbon nanofibers to ionize Argon and demonstrated that the ionization was, at least partly, due to a field ionization process. First, we developed mathematical models and corresponding equations for analyzing field ionization data in the low field regime; these equations for the low field regime were tested on two different sets of data.

A characterization of our Plasma-Enhanced Chemical Vapor Deposition (PECVD) tool for growing vertically aligned carbon nanofibers was reported. This characterization was taken using multiple growths and varying growth parameters like the growth time and the growth temperature.

We presented MATLAB simulations which results helped in designing our device. The simulations predicted near-optimal field amplification of our ionization elements at heights between $6 - 8\mu m$. The simulations also confirmed the expected results that optimally amplifying elements would have the smallest possible tip radii and aperture diameters.

Two complete methodologies for fabricating the single-gated FIA were described. The first process is self-aligned, involving the deposition, patterning and etchback of oxide and doped amorphous silicon layers. The second process involved a MEMS assembly of the gate above the ionization elements.

For the FIA, we measured currents of about $1nA$ at the anode with a device fabricated by the MEMS assembly process described. After extracting the Fowler-Nordheim coefficients from data obtained when we used the array as a field emission array (FEA), we deduced that the associated β was in the range $1.02 \times 10^5 < \beta < 1.38 \times 10^5$ $/cm$. Since the voltage sweeps during Field Ionization testing peaked at $1000V$, we estimate that the surface electric fields were about $10^8 V/cm$

The tested device does not meet the requirements of the miniaturized mass spectrometer in the MGA program. The anode ion currents of order $1nA$ fall short of the $10\mu A$ required at the ionizer output. Even if we assume an anode extraction efficiency of about 5% that has been repeatedly demonstrated in field emission experiments using the same probe station, the device is still at least 2 orders of magnitude insufficient.

7.2 Suggestions for Future Work

To improve the output currents of the FIA, it would be necessary to:

1. Shorten the gate-tip distance by using the self-aligned gate in an actual device
2. Investigate reducing the radius of the grown CNTs by reducing the volume of catalyst nanodots

Also, a fuller characterization of the CCNT needs to be done with a full functional plasma generator and patterned samples with TiN diffusion barrier.

A Self-Aligned Gate Fabrication Process Flow

Table A.1: Complete Process Flow of the Fabrication of the Self-Aligned Gates

Step #	Lab	Machine	Recipe	Description
1	ICL	RCA	Standard RCA	
2	ICL	Endura	500A TiN	Deposit diffusion barrier
3	TRL	eBeamFP	50nm Ti	Deposit Ti crosshair layer
4	TRL	eBeamFP	250nm Au	Deposit Au crosshair layer
5	TRL	HMDS	OCG primer	Resist vapor primer
6	TRL	Coater	30 secs, 3 KHz, OCG	Spin resist for photolithography
7	TRL	Pre-bake	30 mins, 90^oC bake	
8	TRL	EV1	1.8 secs, crosshairs mask	Define non-crosshair areas in resist
9	TRL	photo-wet-1	90 secs OCG 934 soak; DI rinse	Develop exposed crosshairs
10	TRL	Spin-dry Au		
11	TRL	Post-bake	30 mins, 120^oC bake	
12	TRL	Acid-hood	1 - 2 mins Gold-etchant soak	Remove Au in non-crosshair areas
13	TRL	Acid-hood	10 secs BOE soak	Remove Ti in non-crosshair areas
14	TRL	Spin-dry Au		
15	TRL	Asher	1 hour oxygen plasma clean	Remove OCG resist, crosshairs complete

Continued on Next Page...

Table A.1 – Continued

Step #	Lab	Machine	Recipe	Description
16	TRL	PMMASpinner	5 secs at 500 rpm; 70 secs at 3 krpm; 90 secs hot plate bake at 180^oC	Spin 0.25um PMMA; 950 PMMA A4 used
17	SEBL	Raith	Direct write	Define (200nm x 200nm) nanodot locations
18	TRL	photo-wet-Au	90 secs 2:1 IPA:MIBK soak at 21 ± 0.5^oC; 1 min IPA spray; Nitrogen gun blow dry	Develop PMMA
19	TRL	eBeamFP	7 - 9 nm Ni	Deposit growth catalyst
20	TRL	photo-wet-Au	NMP soak at $60 - 80^oC$, vibrate face-down wafer slowly; Acetone rinse; IPA rinse; DI rinse	Lift-off PMMA
21	ICL	semZeiss		Image nano dots
22	TRL	CCNT	40 mins, 825^oC, 600V, 90W	Grow CNTs
23	ICL	semZeiss		Image CNTs
25	TRL	STS-CVD	15.5 mins lfsio	Deposit Insulating oxide
26	ICL	semZeiss		Image oxide coat, 1.8um sidewall diameter
28	TRL	STS-CVD	80+ mins jendope 20W	Deposit doped amorphous Si for gate material
29	ICL	semZeiss		Image amor-Si coat, 2.3um sidewall diameter
30	TRL	HMDS	OCG primer	Resist vapor primer
31	TRL	Coater	2.5 KHz OCG	Spin enough resist to almost cover the tips, might need multiple spins
32	TRL	Pre-bake	30 mins, 90^oC bake	
33	ICL	semZeiss		Check resist level

Continued on Next Page...

Table A.1 – Continued

Step #	Lab	Machine	Recipe	Description
34	TRL	STS1	60s Oxygen plasma clean	Expose amor-Si-coated tips
35	ICL	semZeiss		Check that amor-Si-coated tips are exposed
36	TRL	STS1	15s SF6-14 plasma etch	Etch exposed amor-Si until underlying oxide is exposed
37	ICL	semZeiss		Check that oxide is exposed
38	TRL	Asher	1 hour oxygen plasma clean	Remove OCG resist
39	ICL	semZeiss		Check that resist is completely removed
40	TRL	Acid-hood	7 mins BOE soak	Etch back oxide
41	TRL	Spin-dry Au		
42	ICL	semZeiss		Check that CNTs are exposed

B CCNT Characterization Data

Growth Stage				Plasma		Growth Height (μm)	
Temperature (C)	*Time (min)*	Ammonia (sccm)	Acetylene (sccm)	Voltage (V)	*Power (W)*	*Average*	Standard deviation
656	***19.2***	400	100	624	***143.1***	***1.54***	0.28
656	***39.2***	400	100	665	***142.0***	***4.34***	0.56
750	***3.8***	400	100	665.7	***107.6***	***0.40***	0.06
750	***18.9***	400	100	677.7	***110.5***	***3.50***	0.56
750	***37.8***	400	100	678.9	***108.9***	***5.32***	0.28
750	***21.6***	300	75	676.3	***76.2***	***3.46***	0.13
750	***42.5***	300	75	678.6	***68.1***	***6.59***	0.32
825	***4.4***	400	100	665.6	***138.9***	***2.52***	0.28
825	***7.4***	400	100	606.1	***113.3***	***2.38***	0.52
825	***9.7***	400	100	673.8	***118.8***	***4.48***	0.40
825	***18.9***	400	100	675.4	***104.3***	***5.70***	0.22
825	***19.0***	400	100	672	***124.4***	***6.55***	0.51
825	***28.6***	400	100	677.5	***96.5***	***9.20***	0.36
825	***37.7***	400	100	677.7	***82.3***	***9.51***	0.78
825	***39.1***	400	100	643.2	***72.1***	***10.14***	0.88

Forest Growth Characterization Data
All forest growths required a 5-minute Ammonia anneal at 650°C before growth

C MATLAB CODE

Listing C.1: CNT Tip Geometry

```
function [x,y] = cnt(r,h,t,s, sc)
global brad
% r = tip radius of curvature
% h = height of CNT
% t = base angle of upper CNT
% 2s + 1 = # points on tip half
% distances given in m
if (nargin < 1)
    r=5e-9; h=4e-6; t=70; s=50;
    figure(88),clf, set(gcf, 'DefaultLineLineWidth', 2), hold on
end
if (nargin < 5)
    sc = s; % # pts to use for side curve
end

tr = t * pi/180; % t in radians
x = zeros(s+sc, 1);                    y = x;
x(1)=0;                                y(1)=h;

nextInd = 2;
% curved tip
for i = 1:s
    ang=tr*i/s;
    x(nextInd) = r * sin(ang);  %going down, s pts on right side of apex
    y(nextInd) = r * cos(ang) + (h-r);
    nextInd = nextInd + 1;
end %% end curved tip

ht = h + r/cos(tr)-r; % total height if cone was a perfect triangle
dbrad = ht/tan(tr); % base radius if extends down w/ base angle
xint = brad; % limiting radius
yint = ht - xint*tan(tr); %height at limiting radius

indStartSC = nextInd;
% % side curve
r2 = brad;
tt = t; %asin((h-r)/r2)*180/pi;
ttt = (89.5 - t)*pi/180;
yStep = y(nextInd - 1) / (sc);
yStepTot = sc*yStep;
```

```
rr = 2;
yStepStart = yStepTot * 6 /(sc*(sc+1)*(2*sc+1));
for k = 1:sc
    tang = tan(tr + k*ttt/sc);
    yst = (yStepStart * k^2);
    x(nextInd) = x(nextInd - 1) + yst/ tang;
    y(nextInd) = y(nextInd - 1) - yst;
    nextInd = nextInd + 1;
end

if (sc > 0)
    %% scale side curve so that last pt is brad in width
    x(indStartSC:(nextInd-1))
    = x(indStartSC:(nextInd-1)) * (brad) / x(nextInd-1);
    %% shift side curve so that first pt falls neatly under tip curve
    x(indStartSC:(nextInd-1))=  x(indStartSC:(nextInd-1))
          + ((ht - y(indStartSC))/tan(tr) - x(indStartSC));
    % smoothening
    for gh=1:1
        x(indStartSC:(nextInd-1)) =
        filter(ones(1,2)/2,1,x(indStartSC:(nextInd-1)));
        y(indStartSC:(nextInd-1)) =
        filter(ones(1,2)/2,1,y(indStartSC:(nextInd-1)));
    end
    % remove first pt(s) on sc to provide some smoothness
    pts2rem = [indStartSC:indStartSC];
    x(pts2rem) = [];  y(pts2rem) = [];
    nextInd = nextInd - length(pts2rem);

    ragn = find(x>(brad-eps));
    x(ragn)=[];      y(ragn)=[];      nextInd=nextInd-length(ragn);
end

% base pts
x(nextInd) = brad;  y(nextInd) = 0;      nextInd = nextInd + 1;
x(nextInd) = 0;     y(nextInd) = 0;

if (nargin < 1)
    xx=[flipud(-x);x];yy=[flipud(y);y];%% plot whole
    %xx = x; yy=y; %% plot half
    subplot(2,2,[1,3]),patch(xx,yy,'y'); axis equal;

    subplot(2,2,2),stem(diff(xx)), subplot(2,2,4), stem(diff(yy))
    subplot(2,2,[1,3]),patch(xx,yy,'y');
    axis([1e-7*6*[-1 1] (- 80e-9) (h+20e-9)]); axis equal;

    subplot(2,2,[2,4]),patch(xx,yy,'y');
    axis([1e-9*5*[-1 1] (h - 50e-9) (h+20e-9)]); axis equal;

end
return
```

Listing C.2: Gate Geometry

```
function [x1,y1] = gate(aperture,height,thickness,xmax)

%       There will be 30 segments along the bullnose
        s = 30;

x = zeros(s+2, 1);
y = x;

halfapr = aperture/2;
halft = thickness/2;

x(1)=xmax;                  y(1)= height;

%       Points along the bullnose
for i = 0:s
        x(i+2) = halfapr+halft-(halft*sin(pi*i/s));
        y(i+2) = height+halft-(halft*cos(pi*i/s));
end

lastind = length(x)+1;
x(lastind)= xmax;
y(lastind)= height + thickness;

x1=x; y1=y;

%x2=-x; y2=y;

return;
```

Listing C.3: Device Model file for PDE Solver

```
function [p,e,t,u,c,pde_fig] = cntmodel(gateVoltage, anodeVoltage,
                                        cntVoltage, useAdaptive)

global roc hei thi apr the tiphei brad sss numRefine
global xmax ymax useRandthe useGate p_TRISIZE p_HGRAD p_REFINEMETHOD

if useRandthe
    rand('state',sum(100*clock));
    therover = [83:.2:88];
    the = therover(fix(rand * length(therover))+1);
end

% define structures
% adjust length of roc segments
ssss = sss;
if (roc < 5e-9), ssss = round(sss*roc/5e-9);, end
[xc,yc] = cntcat(roc, tiphei, the, ssss);
[xg,yg] = gate(apr, hei, thi, xmax);
% figure(71)
% plot(xc,yc, 'r', 'linewidth', 2), hold on, plot(xg, yg)
% hold off

pdeinit;
pde_fig=gcf; pde_fig=findobj(allchild(0),'flat','Tag','PDETool');
ax=gca; ax=findobj(allchild(pde_fig),'flat','Tag','PDEAxes');
set(pde_fig,'CurrentAxes',ax)
pdetool('appl_cb',5);
set(ax,'DataAspectRatio',[1 3 1]);
set(ax,'PlotBoxAspectRatio',[xmax ymax 1]);
%set(ax,'AspectRatio',[1.5 1]);
set(ax,'XLim',[0 xmax]);
set(ax,'YLim',[0 ymax]);
set(ax,'XLimMode','auto');
set(ax,'YLimMode','auto');
set(ax,'XTickMode','auto');
set(ax,'YTickMode','auto');
set(ax,'xcolor',[1 1 1]);
set(ax,'ycolor',[1 1 1]);

pdepoly(xc', yc', 'cnt');
pderect([0 xmax 0 ymax], 'R1');

if ~logical(useGate)
    %disp('will not use Gate')
    set(findobj(get(pde_fig, 'Children'),'Tag','PDEEval'),'String','R1-cnt');
else
    %disp('using Gate')
    pdepoly(xg', yg', 'gateR');
    set(findobj(get(pde_fig, 'Children'),'Tag','PDEEval'),...
        'String','R1-(cnt+gateR)');
end
disp(['Geometry drawn ... set boundaries?'])
pause;
```

```
% Boundary conditions:
pdetool('changemode',0)
gVstr = num2str(gateVoltage);
cVstr = num2str(cntVoltage);
aVstr = num2str(anodeVoltage);

% # edges on cnt
cntedgeCount = length(xc)-2;
gatedgeCount = length(xg)-1;
pdesetbd(1:cntedgeCount, 'dir',1,'1',cVstr);
%pdesetbd(1:cntedgeCount, 'neu',1,'0','0');

if ~logical(useGate)
    % top horiz boundary = ANODE
    pdesetbd(cntedgeCount+2, 'dir',1,'1',aVstr);

    % bottom horiz boundary, set to same voltage as CNT
    pdesetbd(cntedgeCount+3, 'dir',1,'1',cVstr);

    % vertical boundaries set as neuman
    pdesetbd(cntedgeCount + ([1 4]), 'neu',1,'0','0');
else
    % gate
    pdesetbd(cntedgeCount + (1:gatedgeCount), 'dir',1,'1',gVstr);

    % top horiz boundary = ANODE
    pdesetbd(cntedgeCount+gatedgeCount+1, 'dir',1,'1',aVstr);

    % bottom horiz boundary, set to same voltage as CNT
    pdesetbd(cntedgeCount+gatedgeCount+2, 'dir',1,'1',cVstr);

    % vertical boundaries set as neuman
    pdesetbd(cntedgeCount+gatedgeCount + (3:5), 'neu',1,'0','0');
end

disp(['Boundaries set ... generate mesh?'])
pause;

% Mesh generation:
setappdata(pde_fig,'trisize', p_TRISIZE);
setappdata(pde_fig,'Hgrad', p_HGRAD);
if p_REFINEMETHOD == 1, setappdata(pde_fig,'refinemethod','regular');
else, setappdata(pde_fig,'refinemethod','longest');, end
disp(['Initializing mesh ... tic']),   tic
pdetool('initmesh')

disp(['Refining mesh ... '])
for r=1:numRefine
    disp(['Refine explicit iteration # ' num2str(r)
        '       + 1 Explicit Jiggling ... '])
    pdetool('refine'),  pdetool('jiggle')
end,        toc
disp(['Mesh generated ... Solve PDE?'])
pause;
```

```
% PDE coefficients:
pdeseteq(1,'1.0','0.0','0','1.0','0:10','0.0','0.0','[0 100]')
setappdata(pde_fig,'currparam',['1.0';'0  '])

% Solve parameters:
if exist('useAdaptive') & (useAdaptive == 1 | useAdaptive == '1')
    useAdaptive = '1';, else useAdaptive = '0';, end
setappdata(pde_fig,'solveparam',...
    str2mat(useAdaptive,'963456','10','pdeadworst','0.5','longest','0',...
    '1e-5','','fixed','inf'))

% Plotflags and user data strings:
setappdata(pde_fig,'plotflags',[1 1 1 1 1 1 1 1 0 0 0 1 1 1 0 1 0 1]);
setappdata(pde_fig,'colstring','');
setappdata(pde_fig,'arrowstring','');
setappdata(pde_fig,'deformstring','');
setappdata(pde_fig,'heightstring','');

tic
pdetool('solve'); toc
[p,e,t,u,c] = getpetuc;

end
```

Listing C.4: Extracts Potential and Field Values at input coordinates

```
function [V, Fx, Fy] = interp_vf(p,t,u,curr_x, curr_y)
%% extracts potential and field values at provided co-ordinates
%% curr_x, curr_y should be in scaled units corresponding to point matrix p
%disp(['interp_vf ... Got curr_x= ' num2str(curr_x) ' curr_y= ' num2str(curr_y)])
inc = 1e-11;
Vgrid = tri2grid(p, t, u, curr_x-1e-10:inc:curr_x+1e-10, ...
    curr_y-1e-10:inc:curr_y+1e-10); % potential around current pt
[Egridx, Egridy] = gradient(Vgrid, inc); % Ex,Ey
Fx = -Egridx(11,11); Fy = -Egridy(11,11);
V = Vgrid(11,11);
end
```

Listing C.5: Returns field solutions along given coordinates

```
function  [rr, Egrid] = plotFieldonPath(p,t,u,rz)

% extrapolate u data to a grid containing as many of the xx,yy elements as
% is legal for the given solution space
rzsize_x = size(rz, 2);
if (rzsize_x ~= 2), rz = rz';, end % make rz ?x2

% first find correction for y_pts using tip location
tip_z = min(p(2,find(p(1,:)==0)));
[V_tip, Fr_tip, Fz_tip] = interp_vf(p,t,u, 0, tip_z);
% pause on, pause, pause off
Egridr = []; Egridz = [];

for ij = 1:size(rz,1)
    curr_r = rz(ij,1); curr_z = rz(ij,2)+tip_z;
    [V,Fx,Fy]=interp_vf(p,t,u, curr_r, curr_z);
    Egridr = [Egridr; Fx]; Egridz = [Egridz; Fy];
end

Egrid = sqrt(Egridr.^2 + Egridz.^2);

% locations where Egrid is nan, and Egridr is not
Ernan=isnan(Egrid) & ~isnan(Egridr);
Eznan=isnan(Egrid) & ~isnan(Egridz);
Egrid(Ernan) = Egridr(Ernan);
Egrid(Eznan) = Egridz(Eznan);

rr = sqrt(rz(:,1).^2 + rz(:,2).^2);

%[rr Egridr Egridz Egrid];

X = rr; Y = Egrid;
figure(56)
subplot(2,1,1)
plot(X, Y)
p=polyfit(log(X), log(Y), 1);
subplot(2,1,2)
loglog(X, Y, '+', X, exp(polyval(p, log(X))), '-r'), grid on
title(char(['fitted to \beta = ' num2str(exp(p(2))/Fz_tip)
    ' * F_tip * r^{' num2str(p(1)) '}']));
```

Listing C.6: Code for 1D Tunneling Probability Calculations

```
% tunneling probability computations
%fignum = 1;

%plot(x, Vapp(x)+Vim(x))

f = 2; % in V/Angstrom
Zeff = 2;   % Zeff is the atomic number
q = 1.602e-19; % electronic charge
% Pm = atom Potential, r as measured from centre of atom
Pm = @(r) - Zeff * 14.394 ./ abs(r);
Vapp = @(x) f*x;   % applied potential
Vim = @(x) -(3.6)./x;

% integration arrays
% distance coordinates for sampling
delta = 1e-4; % in Angstroms
I = 24.587; % ionization potential of He
ro = 0.31; % atomic radius of He
phi = 4.5; % work functino of tip material
xc = (I - phi)/ f ;% point of critical approach
X = [0.2:delta:9.4];  % in Angstroms
Ec = - phi; % Ec @ critical approach is (- work function)

%% Creating figure & axes
%fignum = 1;
fig = figure(fignum); fignum = fignum + 1;
set(fig, 'Name', 'Potential Plots, Critical Approach');
annotation3 = annotation(fig,'textbox','Position',[0.4176 0.9371 0.2274 0.04643],...
    'String',{'Calculations done for He atom'},'FitHeightToText','on');

% % HARD-CODED NUMERICAL INTEGRATION
%%%%%%%%%%%%%%%%%%%%%%%%%%%%%%%%%%%%%%%%%%[0.2912 0.3147],[0.6957 0.7943]
YY = @(x) Vapp(x) + Pm(xc - x) + Vim(x);
Yvals = YY(X) - Ec;
a1 = subplot(2,2,1); t='Potential Barrier';
fhhh=@(a1, t) title(t) & xlabel('Distance / Angstroms');
set(a1,'YLim', [-30 10]);
plot(X, Yvals + Ec, '--', 'displayname', t), fhhh(a1, t);
set(a1,'YLim', [-30 10])
annotation1 = annotation(fig,'line',[0.1314 0.4659],[0.7986 0.7986]);
annotation2 = annotation(fig,'textarrow', [0.2912 0.3147],[0.6957 0.7943],...
    'String', {'Ec = Electron Energy @ critical approach'});
a1 = subplot(2,2,2); t='Potential Barrier - Ec';
plot(X, Yvals, 'displayname', t), fhhh(a1, t);set(a1,'YLim', [-30 10])
% plot(X, Ec, '.-', 'displayname', 'electron')

Yvals(Yvals < 0) = 0;
a1 = subplot(2,2,3); t='with negative values zeroed off';
plot(X, Yvals, '-r', 'displayname', t), fhhh(a1, t); set(a1,'YLim', [-30 10])
Yvals = sqrt(Yvals);
a1 = subplot(2,2,4); t='Sq Root of Energy Interval';
plot(X, Yvals, 'g', 'linewidth',2, 'displayname',t ), fhhh(a1, t);
set(a1,'YLim', [-30 10])
```

```
area = 0.5 * delta * (2 * sum(Yvals) - Yvals(1) - Yvals(length(Yvals)));

me = 9.11e-31; % in kg
hbar = 1.055e-34/1.602e-19; % in eV-s
D = exp(-2* sqrt( 2*me/hbar^2 ) * area)

% % BUILT-IN NUMERICAL INTEGRATION
%%%%%%%%%%%%%%%%%%%%%%%%%%%%%%%%%%%%%%%%%%%%%%

area = quad(@(x) non0IffPositDiff(YY, Ec, x), 0.2, xc) ;
D = exp(-2* sqrt( 2*me/hbar^2 ) * area)
hold off
```

Bibliography

[1] Riehl et al. "Electrostatic Charge and Field Sensors based on Micromechanical Resonators." *Journal of Micromechanical Systems.* 2003.

[2] Akbar Montaser. *Inductively Coupled Plasma Mass Spectrometry.* Wiley-VCH. 1998.

[3] Y. Yin, J. Messier and J. A. Hopwood. "Miniaturization of Inductively Coupled Plasma Sources." *IEEE Transactions on Plasma Science.* **27**, 5, 1516, 1999.

[4] M. Barber, R. S. Bordoli, G. J. Elliot, R. D. Sedgwick, and A. N. Tyler. *Anal. Chem.* **54**, 645A, 1982.

[5] Prokai, L. *Field Desorption Mass Spectrometry.* Marcel Dekker, New York, 1990.

[6] Gomer, Robert. *Field Emission and Field Ionization.* Springer, 1993.

[7] Fenn, J. B., Mann, M., Meng, C. K., Wong, S. F., Whitehouse, C. M. "Electrospray Ionization-Principles and Practice." *Mass Spectrometry Reviews.* **9**, 1, 37-70, 1990.

[8] Brink, G. O. *Rev. Sci. Instrum.* **37**, 857-60, 1966.

[9] Bickes, R. W. and Bernstein R. B. *Rev. Sci. Instrum.* **41**, 759-68, 1970.

[10] Parks, E. K., Young, C. E. and Wexler S. *Rev. Sci. Instrum.* **42**, 1404-7, 1971.

[11] T. D. Mark and G. H. Dunn. *Electron Impact Ionization.* Springer, 1985.

[12] C. A. Spindt "Micro-fabricated field-emission and field-ionization sources." *Surface Science.* **266**, 145-154, 1992.

[13] S. Dushman, "Electron emission from metals as a function of temperature." *Phys. Rev.* **21**, 623, 1923.

[14] E M Oks. "Physics and technique of plasma electron sources." *Plasma Sources Sci. Technol.* **1**, 249-255, 1992.

[15] C. A. Spindt, C. E. Holland, A. Rosengreen, and Ivor Brodie. "Field-Emitter-Array Development for Microwave Microelectronics." *IEDM.* **16**, 1995.

[16] R. H. Good & E. W. Muller. "Field Emission." *Handbook of Physics.* **21**, 176, 1956.

[17] R. H. Fowler and L. W. Nordheim. "Electron Emission in Intense Electric Fields." *Proc. R. Soc. London.* **119**, 173, 1928.

[18] J. H. Gross. *Mass Spectrometry: A textbook.* Springer-Verlag, Berlin, Germany, 2004.

[19] E. de Hoffmann and V. Stroobant. *Mass Spectrometry: Principles and Applications.* John Wiley & Sons, West Sussex, England, 2002.

[20] D. Riley, K. B. K. Teo et al. "Helium Detection via Field Ionization from Carbon Nanotubes." *Nano Letters.* **3.10**, 1455-1458, 2003.

[21] Kuei-Yi Lee, S. Honda, M. Katayama, T. Miyake, K. Himuro, K. Oura, J. Lee, H. Mori and T. Hirao. "Vertically aligned growth of carbon nanotubes with long length and high density." *Journal of Vacuum Science & Technology B: Microelectronics and Nanometer Structures.* **23**, 4, 14501453, July 2005.

[22] Zhong Lin Wang, Yi Liu and Ze Zhang. *Handbook of Nanophase and Nanostructured Materials.* Springer, 2003.

[23] M. Wang, Z. H. Li, X. F. Shang, X. Q. Wang and Y.B. Xu. "Field-enhancement factor for carbon nanotube array." *Journal of Applied Physics.* **98**, 014315, 2005.

[24] Y. Saito and S. Uemura. "Field emission from carbon nanotubes and its application to electron sources." *Carbon.* **38**, 169-182, 2000.

[25] J. D. Jackson. *Introduction to Finite and Boundary Element Methods for Engineers.* 2nd edition. New York: John Wiley & Sons, Inc., 1975.

[26] L. Dvorson, M. Ding & A. I. Akinwande. "Analytical Electrostatic Model of Silicon Conical Field Emitters-Part I." *IEEE Transactions on Electron Devices.* **48**, 134, Jan. 2001

[27] David G. Pflug. "Low Voltage Field Emitter Arrays through Aperture Scaling." PhD Thesis. Massachusetts Institute of Technology, September 2000.

[28] Beer G. and Watson JO. *Introduction to Finite and Boundary Element Methods for Engineers.* New York: John Wiley & Sons, Inc., 1992.

[29] Yang, YJ. "Numerical Analysis and Design Strategy for Field Emission Devices." PhD Thesis. Massachusetts Institute of Technology, August 1998.

[30] C. A. Spindt, C. E. Holland, A. Rosengreen, and Ivor Brodie. "Field Emitter Arrays for Vacuum Microelectronics." *IEEE Transactions on Electron Devices.* **38**, 10, 2355-2363, 1991.

[31] C. E. Hunt, Johann T. Trujillo, and W. J. Orvis. "Structure and Characteristics of Silicon Field-Emission Microelectronic Devices." *IEEE Transactions on Electron Devices.* **38**, 10, 2309-2313, 1991.

[32] Dorota Temple. "Recent Progress in Field Emitter Array Development for High Performance Applications." *Materials Science and Engineering.* **R24**, 185-239, 1999.

[33] V. I. Merkulov, A. V. Melechko, M. A. Guillorn, D. H. Lowndes, & M. L. Simpson, *Applied Physics Letters.* **79**, 2970 (2001); L. R. Baylor, V. I. Merculov, E. D. Ellis, M. A. Guillorn, D. H. Lowndes, A. V. Melechko, M. L. Simpson, and J. H. Whealton, *J. Appl. Phys.* **91**, 4602 (2002).

[34] J. Appelbaum, D. Hamann. "Variational Calculation of the Image Potential near a Metal surface." *Physical Review B.* **VI.4**, 1122, 1972.

[35] Z. F. Ren, Z. P. Huang, J. W. Xu, J. H. Wang, P. Bush, M. P. Siegal, and P. N. Provencio. "Synthesis of Large Arrays of Well-Aligned Carbon Nanotubes on Glass." *Science.* **282**, 5391, 1998.

[36] Iijima, S. "Helical microtubules of graphitic carbon." *Nature.* **354**, 56, 1991.

[37] Dresselhaus, M. S. Dresselhaus, G. and Jorio, A. "Unusual properties and structures of carbon nanotubes." *Annual Reviews of Materials Research.* **34**, 247-278, 2004.

[38] Saito, R. Dresselhaus, G. & Dresselhaus, M. S. *Physical Properties of Carbon Nanotubes* London: Imperial College Press, 1998.

[39] R. Martel, T. Schmidt, H. R. Shea, T. Hertel. and Ph. Avouris. "Single- and multi-wa carbon nanotube field-effect transistors." *Applied Physics Letters.* **73**, 17, 2447, 1998.

[40] H. Dai, N. Franklin & J. Han. *Applied Physics Letters.* **73**, 1508, 1998.

[41] W. A. de Heer, A. Chatelaine & D. Ugarte. *Science.* **270**, 1179, 1995.

[42] E. Frackowiak, K. Metenier, V. Bertagna & F. Beguin. *Applied Physics Letters.* **77**, 2421, 2000.

[43] Dresselhaus, M. S. & Eklund, P. C. "Phonons in Carbon Nanotubes." *Advances in Physics.* **49.6**, 705-814, 2000.

[44] Wang, S. et al. "Peptides with selective affinity for carbon nanotubes." *Nature.* **833**, 196, 2003.

[45] K. Teo et al. "Uniform patterned growth of carbon nanotubes without surface carbon." *Applied Physics Letters.* **79**, 10, 2001.

[46] K. Teo, C. Singh, M. Chhowalla, W. Milne. "Catalytic Synthesis of Carbon Nanotubes and Nanofibers." *Encyclopedia of Nanoscience and Nanotechnology.* **X**, 1, 2003.

[47] K. Teo et al. "Plasma enhanced chemical vapour deposition carbon nanotubes/-nanofibers how uniform do they grow?." *Institute of Physics Publishing - Nanotechnology.* **14**, 204-211, 2003.

[48] L. Nilsson, O. Groening, C. Emmenegger, O. Kuettel, E. Schaller, L. Schlapbach, H. Kind, J. M. Bonard, and K. Kern. *Appl. Phys. Lett.* **76**, 2071, 2000.